Discovery and analysis of afterglows from poorly localized GRBs with the Gravitational-wave Optical Transient Observer (GOTO) All-sky Survey

Amit Kumar \$\bigcap\$, \$\frac{1,2*}{2}\$ B. P. Gompertz \$\bigcap\$, \$\frac{3}{4}\$ B. Schneider \$\bigcap\$, \$\frac{5}{5}\$ S. Belkin \$\bigcap\$, \$\hat{6}\$ M. E. Wortley \$\bigcap\$, \$\frac{3}{4}\$ A. Saccardi \$\bigcap\$, 7 D. O'Neill \$\bigcap\$, \$\frac{3}{4}\$ K. Ackley \$\bigcap\$, 2 B. Rayson \$\bigcap\$, 8 A. de Ugarte Postigo \$\bigcap\$, 5 A. Gulati \$\bigcap\$, \$\frac{9}{2}\$, \$\line{10}\$, \$\line{10}\$ D. Steeghs \$\bigcap\$, 2 D. B. Malesani \$\bigcap\$, \$\frac{12}{12}\$, 13,14 J. R. Maund \$\bigcap\$, 1 M. J. Dyer \$\bigcap\$, \$\frac{15}{15}\$, 16 S. Giarratana \$\bigcap\$, 7 M. Serino, \$\frac{18}{5}\$ Y. Julakanti \$\bigcap\$, 8 B. Kumar \$\bigcap\$, 920 D. Xu \$\bigcap\$, 21 R. A. J. Eyles-Ferris \$\bigcap\$, 8 Z.-P. Zhu \$\bigcap\$, 21 B. Warwick \$\bigcap\$, 2 Y.-D. Hu \$\bigcap\$, 22 I. Allen, 3 G. Ramsay \$\bigcap\$, 23 R. L. C. Starling \$\bigcap\$, 8 J. Lyman \$\bigcap\$, 2 K. Ulaczyk, 2 B. Godson \$\bigcap\$, 2 D. K. Galloway \$\bigcap\$, 6.24 V. S. Dhillon \$\bigcap\$, 15,25 P. O'Brien \$\bigcap\$, 8 K. Noysena \$\bigcap\$, 26 R. Kotak, 27 R. P. Breton \$\bigcap\$, 28 L. K. Nuttall \$\bigcap\$, 29 D. Pollacco, 2 J. Casares \$\bigcap\$, 25,30 T. L. Killestein, 2 M. R. Kennedy \$\bigcap\$, 31 N. Habeeb \$\bigcap\$, 8 S. Moran \$\bigcap\$, 8 K. Wiersema \$\bigcap\$, 32 I. Worssam \$\bigcap\$, 34 D. L. Coppejans \$\bigcap\$, 2 C. A. Phillips \$\bigcap\$, 2 A. Martin-Carrillo \$\bigcap\$, 33 N. S. Pankov \$\bigcap\$, 34,35 J. F. Agüí Fernández \$\bigcap\$, 36 M. A. Aloy \$\bigcap\$, 37,38 J. An \$\bigcap\$, 21 G. E. Anderson \$\bigcap\$, 39,9 A. Bochenek \$\bigcap\$, 40 A. J. Castro-Tirado \$\bigcap\$, 41,42 X. Chen \$\bigcap\$, 19,20 L. Cotter \$\bigcap\$, 33 R. Deptate \$\bigcap\$, 44 V. D'Elia \$\bigcap\$, 45 Y. Fang \$\bigcap\$, 19,20 S. Y. Fu \$\bigcap\$, 45 J. P. U. Fynbo \$\bigcap\$, 12,13 D. H. Hartmann \$\bigcap\$, 47 L. B. He, 21 L. Izzo \$\bigcap\$, 48,13 S. Q. Jiang \$\bigcap\$, 17 Y. Kawakubo \$\bigcap\$, 18 E. V. Klunko, 49 A. J. Levan \$\bigcap\$, 14,2 X.-W. Liu \$\bigcap\$, 19,20 X. Liu \$\bigcap\$, 21 G. Lombardi \$\bigcap\$, 50,25 E. Maiorano \$\bigcap\$, 51 J. T. Palmerio \$\bigcap\$, 52 D. A. Perley \$\bigcap\$, 4

Affiliations are listed at the end of the paper

Accepted 2025 September 26. in original form 2025 September 11

ABSTRACT

Gamma-ray bursts (GRBs), particularly those detected by wide-field instruments such as the Fermi/GBM, pose challenges for optical follow-up because of their large initial localization regions, leaving many GRBs without identified afterglows. The Gravitational-wave Optical Transient Observer (GOTO), with its wide field of view, dual-site coverage, and robotic rapid-response capability, bridges this gap by rapidly identifying and localizing afterglows from alerts issued by space-based facilities including Fermi, SVOM, Swift, and the EP, providing early optical positions for coordinated multiwavelength follow-up. In this paper, we present optical afterglow localization and multiband follow-up of five Fermi/GBM (240619A, 240910A, 240916A, 241002B, and 241228B) and two MAXI/GSC (240122A and 240225B) triggered long GRBs discovered by GOTO in 2024. Spectroscopy for six GRBs (no spectroscopy for GRB 241002B) with VLT/X-shooter and GTC/OSIRIS yields precise redshifts spanning $z \approx 0.40-3.16$ and absorption-line diagnostics of hosts and intervening systems. Radio detections for four events (240122A, 240619A, 240910A, and 240916A) confirm the presence of long-lived synchrotron emission. Prompt-emission analysis with Fermi and MAXI data reveals a spectrally hard population, with two bursts lying $> 3\sigma$ above the Amati relation. Although their optical afterglows resemble those of typical long GRBs, the prompt spectra are consistently harder than the long-GRB average. Broad-band afterglow modelling of six GOTO-discovered GRBs yields jet half-opening angles of a few degrees and beaming-corrected kinetic energies $E_{\rm jet} \sim 10^{51}$ – 10^{52} erg, consistent with the canonical long-GRB population. These findings suggest that optical discovery of poorly localized GRBs is likely subject to observational biases favouring luminous events with high spectral peak energy (E_p) , while also providing insight into jet microphysics and central engine diversity.

Key words: techniques: photometric – techniques: spectroscopic – gamma-ray burst: individual: GRB 240122A, GRB 240225B, GRB 240619A, GRB 240910A, GRB 240916A, GRB 241002B, GRB 241228B – gamma-ray bursts.

^{*} E-mail: amit.kumar@rhul.ac.uk, amitkundu515@gmail.com

1 INTRODUCTION

The study of gamma-ray bursts (GRBs) has advanced significantly since their discovery in the 1960s (R. W. Klebesadel, I. B. Strong & R. A. Olson 1973; I. B. Strong, R. W. Klebesadel & R. A. Olson 1974), driven by a combination of dedicated space-based surveys and ground-based follow-up observations. From confirming their cosmological origins (Meegan et al. 1992; E. Costa et al. 1997; M. R. Metzger et al. 1997; J. van Paradijs et al. 1997) to uncovering possible progenitors for long and short GRBs (E. P. Mazets et al. 1981; C. Kouveliotou et al. 1993; S. E. Woosley & J. S. Bloom 2006; F.-W. Zhang et al. 2012; B. P. Abbott et al. 2017b), these highenergy events have now been recognized as among the most luminous explosive phenomena in the universe (P. Mészáros 2013; P. Kumar & B. Zhang 2015; A. Levan et al. 2016; LHAASO Collaboration 2023). Observations across the electromagnetic spectrum have not only enhanced our understanding of GRB mechanisms but also established their ability to probe the distant universe (F. Fiore 2001; N. R. Tanvir et al. 2009; P. Petitjean & S. D. Vergani 2011; A. Saccardi et al. 2023, 2025) and constrain cosmological parameters (L. Amati & M. Della Valle 2013; M. Demianski et al. 2017; O. Luongo & M. Muccino 2021; M. Moresco et al. 2022), marking them as invaluable tools in modern astrophysics.

A fundamental classification distinguishes GRBs into longduration $(T_{90}^{-1} \gtrsim 2 \text{ s})$ and short-duration $(T_{90} \lesssim 2 \text{ s})$ bursts (C. Kouveliotou et al. 1993). Long GRBs (LGRBs) are typically associated with the collapse of massive, rapidly rotating stars (S. E. Woosley 1993; W. Zhang, S. E. Woosley & A. Heger 2004; A. Maeder & G. Meynet 2012; B. Zhang 2019; M. Á. Aloy & M. Obergaulinger 2021; M. Obergaulinger & M. Á. Aloy 2022), occasionally accompanied by broad-lined Type Ic supernovae (T. J. Galama et al. 1998; S. E. Woosley & J. S. Bloom 2006; Z. Cano et al. 2017; A. Kumar et al. 2024a). In contrast, short GRBs (SGRBs) generally are thought to originate from compact binary mergers involving neutron stars and/or black holes (D. Eichler et al. 1989; R. Narayan, B. Paczynski & T. Piran 1992; M. Tanaka 2016), and are associated with kilonovae, a connection confirmed through GW170817/GRB 170817A/AT 2017gfo (B. P. Abbott et al. 2017a, b; A. Goldstein et al. 2017; E. Pian et al. 2017; E. Troja et al. 2017; S. Valenti et al. 2017; H. Wang et al. 2017; N. R. Tanvir et al. 2017), see also B. D. Metzger (2019). Although the longshort dichotomy holds in general, recent observations reveal notable exceptions, such as LGRBs 211211A and 230307A that exhibited signatures consistent with kilonova emission and compact object merger progenitors (J. C. Rastinejad et al. 2022; E. Troja et al. 2022; J. Yang et al. 2022; B. P. Gompertz et al. 2023a; C.-Y. Dai et al. 2024; A. J. Levan et al. 2024; H. Sun et al. 2025). Conversely, SGRB 200826A showed a possible association with a supernova, suggesting a massive star origin (T. Ahumada et al. 2021; B. B. Zhang et al. 2021; A. Rossi et al. 2022). These atypical cases challenge the traditional progenitor classification and motivate further systematic investigations into the diversity of GRB origins. However, in this work we adopt the conventional $T_{90} \lesssim 2 \,\mathrm{s}$ and $T_{90} \gtrsim 2 \,\mathrm{s}$ division as a working classification. While exceptions to this dichotomy are known (B. Zhang et al. 2009; O. Bromberg et al. 2013; S. Kulkarni & S. Desai 2017), the 2 s threshold remains the standard convention for comparability, and our sample lies comfortably above this boundary, where the risk of misclassification is lower.

The origin of GRBs and the understanding of the underlying physics can be probed using multiwavelength afterglow observations (see D. Miceli & L. Nava 2022). Synchrotron emission from relativistic jets that interact with the circumburst medium encodes information about the jet geometry, ambient density, and microphysical parameters (R. Sari, T. Piran & R. Narayan 1998; J. Granot & R. Sari 2002; A. Panaitescu & P. Kumar 2002), see also L.-L. Zhang et al. (2024). Afterglow light-curve features such as jet breaks, cooling breaks, and chromatic evolution offer insights into jet collimation and energy structure (J. E. Rhoads 1999; R. Sari & T. Piran 1999). Theoretical models provide further context: relativistic jet propagation in collapsars was first explored via simulations (M. A. Aloy et al. 2000), and more recent 3D magnetorotational corecollapse models further demonstrate jet collimation and dynamics in magnetized environments (M. Obergaulinger & M. Á. Aloy 2021). Complementary hydrodynamical studies examine jet-cocoon mixing and structured outflow morphologies (O. Gottlieb et al. 2020).

Early optical and multiwavelength follow-up has revealed a broad diversity in afterglow behaviours, including evidence for reverse shocks (B. Zhang & S. Kobayashi 2005; C. G. Mundell et al. 2007; P. Mimica, D. Giannios & M. A. Aloy 2009, 2010; T. Laskar et al. 2013; S.-X. Yi et al. 2020), energy injection episodes (G. Björnsson, E. H. Gudmundsson & G. Jóhannesson 2004: B. Zhang et al. 2006: T. Laskar et al. 2015), and structured jets (G. P. Lamb & S. Kobayashi 2017; P. Beniamini, J. Granot & R. Gill 2020; G. Oganesyan et al. 2020). Combined with X-ray and radio data, optical observations enable comprehensive modelling of afterglows, shedding light on the energetics and structure of GRB jets (R. Margutti et al. 2013). However, a persistent challenge in GRB afterglow detection and follow-up arises from the poor initial localization provided by widefield gamma-ray monitors such as Fermi Gamma-ray Burst Monitor (GBM; C. Meegan et al. 2009). With the highest GRB detection rate and strong sensitivity to prompt gamma-ray emission, Fermi/GBM enables detailed temporal and spectral studies (C. Meegan et al. 2009; A. von Kienlin et al. 2020), but typically provides localization uncertainties spanning several square degrees. In contrast, missions like Neil Gehrels Swift Observatory (Swift hereafter; N. Gehrels et al. 2004), Einstein Probe (*EP*; W. Yuan et al. 2015, 2022), and Spacebased multiband astronomical Variable Objects Monitor (SVOM; J. Wei et al. 2016) offer arcsecond- to arcminute-level localizations but detect comparatively fewer bursts. Recovering counterparts to these poorly localized GRBs provides a valuable opportunity to expand our understanding of GRB diversity and reduce selection biases. However, the large error regions often exceed the field of view (FoV) of conventional optical telescopes, complicating timely afterglow identification. Furthermore, the intrinsic faintness of some afterglows (E. Liang et al. 2007; H. Dereli et al. 2017) and circumburst extinction (S. Savaglio & S. M. Fall 2004; S. Schulze et al. 2011) can further hinder follow-up. Without alternative localization strategies, a significant fraction of GRBs, particularly those detected by Fermi/GBM, remain uncharacterized, limiting our ability to probe jet physics, energetics, and progenitor properties.

Wide-field optical instruments, such as the Gravitational-wave Optical Transient Observer (GOTO; M. J. Dyer et al. 2020; D. Steeghs et al. 2022), have emerged as powerful tools to address this gap. GOTO, comprising 32 robotic telescopes across two sites, Roque de los Muchachos Observatory (La Palma, Canary Islands)

 $^{^1}T_{90}$ marks the period during which the central 90 per cent of a GRB's total detected emission is observed, from 5 per cent to 95 per cent cumulative count levels.

²https://goto-observatory.org/

and Siding Spring Observatory (New South Wales, Australia), enables near-continuous coverage of both hemispheres (M. J. Dyer et al. 2024). Unlike traditional follow-up facilities, the GOTO instruments can 'tile' the large error regions of GBM-like triggers in near real-time, providing a complementary discovery channel to narrow-field missions and helping to overcome localization-driven selection effects. Its fast-response capabilities and wide FoV make it well-suited to bridging the gap between gamma-ray detection and multiwavelength characterization, particularly for poorly localized but scientifically valuable GRBs.

In this work, we present a systematic study of seven poorly localized LGRBs 240122A, 240225B, 240619A, 240910A, 240916A, 241002B, and 241228B, whose optical afterglows were discovered by GOTO in response to alerts from Fermi/GBM and the Monitor of All-sky X-ray Image (MAXI) Gas Slit Camera (GSC; M. Matsuoka et al. 2009; T. Mihara et al. 2011), with localization uncertainties ranging from a few arcminutes to several square degrees in radius. The structure of this paper is as follows. Section 2 provides an overview of GOTO, outlining its observational strategy and summarizing its past observation records. Section 3 introduces the sample and describes the discovery of their afterglows in terms of localization coverage and optical afterglow detections. Section 4 presents the multiwavelength (X-ray to radio) follow-up observations of the afterglows. Section 5 details the prompt gamma-ray analyses and properties of the GRBs in our sample, along with comparisons to other GRBs. Section 6 discusses the multiwavelength afterglow properties and compares them with literature data for other GRBs, including optical spectroscopic analyses of the afterglows and precise redshift estimates. Section 7 presents the afterglow modelling of six GRBs from our sample using afterglowpy and Bayesian inference with dynesty nested sampling. Finally, Section 8 summarizes our findings and presents the main conclusions of this study.

All magnitudes reported in this work are given in the AB photometric system. We define T_0 as the trigger time reported by the detecting satellite, which serves as the reference epoch for our temporal analysis. For GRBs 240122A and 240225B this corresponds to the MAXI/GSC trigger, while for the remaining five events it corresponds to the Fermi/GBM trigger.

2 GOTO AND ITS APPROACH TO GRB COUNTERPART SEARCHES

2.1 GOTO overview

The Gravitational-wave Optical Transient Observer (GOTO; M. J. Dyer et al. 2020; D. Steeghs et al. 2022; M. J. Dyer et al. 2024) is a global network of 32 robotic unit telescopes (UTs) distributed over two sites, with two domes at each site: the Roque de los Muchachos Observatory on La Palma, Canary Islands, and the Siding Spring Observatory in New South Wales, Australia (see Fig. 1). This configuration enables near-continuous monitoring of both the northern and southern skies.

Each site hosts two independent mounts, with the eight UTs on each mount aligned to form a tiled array with small overlaps, yielding a combined FoV of $\approx 44\,\mathrm{deg^2}$ per mount. With two mounts per site, this provides $\approx 88\,\mathrm{deg^2}$ of instantaneous coverage, and across both sites the network spans $\approx 176\,\mathrm{deg^2}$. This wide coverage makes GOTO particularly well-suited to search for optical counterparts of poorly localized transients such as gravitational-wave events (e.g. B. P. Gompertz et al. 2020), GRBs detected by facilities such as *Fermi*, *SVOM*, and *EP* (e.g. Y. L. Mong et al. 2021; S. Belkin et al. 2024), as well as other fast and exotic transients including rapidly





Figure 1. The full configuration of the GOTO telescope network in April 2023, comprising 32 robotic unit telescopes distributed across four domes, two domes at each of the two sites. Top: GOTO-N, located at the Observatorio del Roque de los Muchachos on La Palma, comprising GOTO-1 (left) and GOTO-2 (right). Bottom: GOTO-S, hosted at Siding Spring Observatory in Australia, consisting of GOTO-3 (left) and GOTO-4 (right). Figure credit: M. J. Dyer et al. 2024.

evolving supernovae and tidal disruption events. The telescopes are equipped with ON Semiconductor KAF-50100 CCDs, which provide broad sensitivity across the optical range, with the deployed Baader filters setting the effective bandpass. In survey mode, a wide L-band (400 – 700 nm) encompassing the Sloan gri filters is used, providing sensitivity to a wide range of transients and maximizing discovery potential.

In 'responsive' mode, the GOTO instruments autonomously observe large sky regions associated with poorly localized transient events, such as GW events, GRBs, and high-energy neutrino alerts, to search for their optical counterparts. The exposure time and cadence in this mode are adapted to the nature of the event and vary accordingly across different source types. This study focuses specifically on the discovery of optical afterglows from poorly localized GRBs using GOTO. The following section outlines the observational strategies employed by GOTO to identify and confirm these afterglows.

2.2 Follow-up strategies to discover GRBs' optical afterglows

In responsive mode, if triggered by a GRB alert, GOTO pauses its survey operations to target the localization region. Follow-up strategies are tailored based on the source of the trigger and the localization uncertainty, as described below and illustrated in the flowchart in Fig. 2.

2.2.1 Swift/BAT, SVOM/ECLAIRs, and EP triggers

Swift, SVOM/ECLAIRs, and EP GRB detections generally come with precise localization (arcsecs to arcmins), far smaller than a single GOTO tile, and which can be easily covered by other observatories

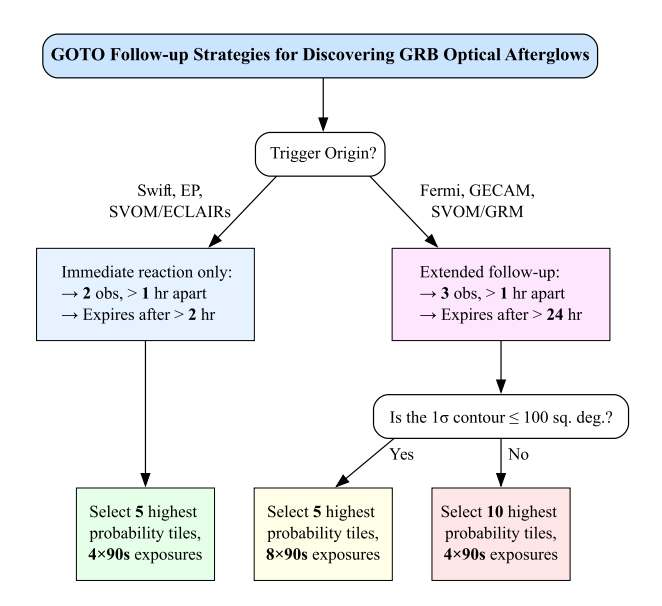


Figure 2. A summary of the GOTO GRB follow-up strategy.

with a lower FoV. Therefore, the primary reason for GOTO to follow up these events is to take advantage of its fast, robotic nature to get rapid coverage of the localization region immediately following the trigger, in order to capture any optical afterglow while it is still bright and young. For these triggers, up to five tiles on the GOTO survey grid are permitted to be selected; however, given the welllocalized nature of these sources, the search region is almost always within a single tile (more than one tile is allowed to be selected for rare cases where a source falls within the overlapping region on the edge of multiple tiles). Two observations are scheduled for each tile, spaced one hour apart, each using the standard set of 4 × 90 s exposures, which typically reaches a depth of \sim 19.8 AB mag in GOTO L-band. However, these targets are only valid in the GOTO scheduling queue for the first two hours after the trigger time. This ensures that rapid observations will be taken if any of the GOTO telescopes are available immediately after the trigger; however, after the two-hour window, GOTO's usefulness is lessened, and any observations are left to other observatories.

2.2.2 Fermi/GBM, SVOM/GRM, and GECAM triggers

Detections from Fermi/GBM, SVOM Gamma Ray burst Monitor (GRM; J. He et al. 2025) and Gravitational Wave Electromagnetic Counterpart All-sky Monitor (GECAM; Y. Chen et al. 2020) often have poorer localization areas (radial uncertainties of a few to tens of degrees), and therefore GOTO's wide FoV is well suited to locating any afterglow. As such, observations for these follow-up campaigns are valid for a 24-h period from the GRB trigger time, with three epochs scheduled spaced at least one hour apart, to ensure the best chance of discovering and observing the evolution of the optical afterglow during its peak brightness phase. As these localization regions can stretch to cover large areas of sky, a limit is imposed to target only the 10 highest tiles sorted by the contained localization probability. This limit was picked based on a recovery rate of 75.5 per cent when applied to 102 historical Fermi/GBM triggers with corresponding Swift/X-Ray Telescope (XRT; D. N. Burrows et al. 2005) detections. The selected tiles are then each scheduled for three observations using the standard 4×90 s exposure set. However, in 2024 an improved strategy was developed: for well-localized events – where the 1σ localization region covers less than $100~\rm deg^2$ – a more focused strategy was created which selects a maximum of five grid tiles for observations but with a double set of $8\times90~\rm s$ exposures, reaching a 5σ depth of $L\sim20.5$ mag. From simulating 50 000 artificial GRB afterglows of varied localization regions, the likelihood of detection was maintained when trading spatial coverage for increased depth and, in certain cases, can result in an approximate $10~\rm per$ cent increase in the afterglow detection chance. This new focused strategy, along with the $10~\rm tile$ limit for larger areas, was introduced in July 2024, prior to which all triggers selected only the five highest tiles for $4\times90~\rm s$ exposures. Of the five Fermi-triggered campaigns described in Section 3, only GRB 240619A used the old selection criteria, meaning it was limited to only five triggered pointings. However, all five events have localization regions of larger than $100~\rm deg^2$, so none would have used the deeper $8\times90~\rm s$ sets.

2.3 Identifying the GRB optical counterpart

For each GOTO observing sequence, whether taken in responsive or survey mode, images are processed in near real-time by the GOTO pipeline (Lyman et al., in preparation), which includes calibration, astrometric solution, and difference imaging against archival deep GOTO templates. Transient candidates are then ranked by a machine-learning classifier (T. L. Killestein et al. 2021), crossmatched to contextual catalogues (e.g. SDSS D. G. York et al. 2000; Pan-STARRS K. C. Chambers et al. 2016), and Solar System ephemerides, and subsequently passed through automated real/bogus and contextual filters.

The Burst Advocate (BA) monitors GRB alerts, confirms that GOTO follow-up has been executed, and initiates candidate vetting in the GOTO marshall. Promising sources are inspected by the working group, including checks against archival imaging and forced photometry, before being promoted for group review. A candidate is classified as the optical afterglow counterpart if it satisfies the following:

- (i) Spatial consistency: positionally coincident with the high-probability GRB localization region, with a point-like PSF and no association with known artefacts or moving objects (minor-planet checks performed). If present, the location relative to a plausible host galaxy is also considered.
- (ii) Temporal behaviour: evidence of fading between successive GOTO epochs, or a later non-detection deeper than the initial detection; where possible, the decline should be consistent with a power-law afterglow behaviour.
- (iii) Contextual screening: absence of a persistent source in archival templates; no counterpart in variable-star catalogues, and not coincident with a known AGN nucleus.
- (iv) Multiwavelength corroboration: spatial consistency with a *Swift*/XRT source strengthens the association, but is not required.

Candidates satisfying criteria (i)–(iii) are promoted to the transient stream and considered GRB afterglow counterparts, while those also fulfilling (iv) are prioritized for rapid spectroscopy and additional ToO follow-up. Confirmed counterparts are reported in General Coordinates Network (GCN³) Circulars and logged in the Transient Name Server (TNS⁴).

³https://gcn.nasa.gov/circulars

⁴https://www.wis-tns.org/

Table 1. Summary of the LGRBs analysed in this work. For each burst, we list the high-energy and optical afterglow discoverers, the time from the high-energy trigger to the optical discovery $(T - T_0)$, the GOTO internal afterglow name, J2000 coordinates, discovery L-band magnitude, Galactic extinction E(B - V), and spectroscopic redshift.

GRB	High-energy discoverer	Optical discoverer	Discovery $T - T_0 (h)^a$	GOTO internal name	RA (h:m:s)	Dec (°:':")	Discovery L-band mag	$\frac{E(B-V)^b}{(\text{mag})}$	Redshift ^c
240122A	MAXI/GSC	GOTO-S	0.73	GOTO24eu	06:12:12.91	-19:08:38.81	17.58 ± 0.04	0.0651	3.1634 ± 0.0003
240225B	MAXI/GSC	GOTO-N	1.50	GOTO24tz	08:33:26.67	+27:04:32.71	17.12 ± 0.04	0.0354	0.9462 ± 0.0002
240619A	Fermi/GBM	GOTO-S	4.69	GOTO24cvn	10:49:34.70	+17:16:58.07	17.17 ± 0.17	0.0253	0.3960 ± 0.0001
240910A	Fermi/GBM	GOTO-S	9.43	GOTO24fvl	01:36:23.45	-00:12:17.86	19.33 ± 0.13	0.0247	1.4605 ± 0.0007
240916A	Fermi/GBM	GOTO-S	7.73	GOTO24fzn	15:43:39.23	-07:45:53.21	17.80 ± 0.06	0.1359	2.6100 ± 0.0002
241002B	Fermi/GBM	GOTO-S	3.05	GOTO24gpc	21:53:16.56	-58:56:51.98	19.53 ± 0.09	0.0268	_
241228B	Fermi/GBM	GOTO-N	0.32	GOTO24jmz	08:31:05.46	+06:50:54.07	14.54 ± 0.01	0.0290	2.6745 ± 0.0004

Notes. ^aFor MAXI GRBs, T₀ denotes the MAXI/GSC trigger time; for Fermi GRBs, T₀ denotes the Fermi/GBM trigger time.

2.4 Observational performance and discovery statistics

The GOTO GRB follow-up programme has developed from its prototype stage to a fully operational dual-site facility (M. J. Dyer et al. 2024), delivering a series of notable discoveries. The prototype system (GOTO-4), comprising four UTs at the La Palma site, achieved first light in June 2017 and was officially inaugurated in July 2017, initiating routine operations (D. Steeghs et al. 2022). During this early phase, GOTO secured its first GRB optical afterglow detection with GRB 171205A, associated with SN 2017iuk (D. Steeghs et al. 2017; L. Izzo et al. 2019). In the initial 3 yr between June 2017 and June 2020, the GOTO-4 system responded to 77 Fermi/GBM and 29 Swift/BAT triggers (see Y. L. Mong et al. 2021; D. Steeghs et al. 2022), demonstrating the scientific potential of the facility even in its prototype configuration.

With full deployment at both sites, as of 2024 December 31 (with GRBs observed thereafter will be included in a future study), GOTO has conducted follow-up observations for over 257 Fermi, 43 Swift-, 28 EP-, and 7 GECAM-triggered events. No targeted observations were conducted for SVOM events during this period, as GOTO began following up SVOM triggers in 2025, coinciding with the scheduled start of SVOM's science operations in February 2025. On average, GOTO's first targeted observation latency was approximately 11.2 h, with response times ranging from 270 s to 69.77 h post-trigger. The average latency for the last observation in each follow-up series was 26.36 h, while the alert latency averaged 4.8 h, underscoring the challenges in achieving timely and efficient follow-ups.

The GOTO collaboration has reported nearly 80 GCN circulars to date based on GOTO observations, including the detection and upper-limit constraints of GRB afterglows. To date, nearly 28 successful detections have been reported, including GRB 230818A, detected 4.43 min after its trigger (B. P. Gompertz et al. 2023c). In addition, GOTO has provided numerous upper-limit constraints and contributed to serendipitous discoveries like orphan afterglow AT2023lcr (B. Gompertz et al. 2023b), with early-phase observations aiding in the refinement of transient properties (Martin-Carrillo et al., in preparation). GOTO's follow-up capabilities continue to evolve in response to operational experience and scientific objectives.

GRB 230911A was the first LGRB for which GOTO discovered an optical afterglow (S. Belkin et al. 2023); details are published in S. Belkin et al. (2024). After this first case, in 2024, GOTO discovered optical afterglows of 2 *MAXI*-triggered (GRB 240122A and GRB 240225B) serendipitously and 5 *Fermi*-triggered (GRBs 240619A, 240910A, 240916A, 241002B, and 241228B) LGRBs in responsive mode, which are studied in detail in this work.

The details of these 7 GRBs in our sample are discussed in the following section. In addition to these LGRBs, within 2024 itself, GOTO also identified the optical afterglow of the SGRB 241105A (Y. Julakanti et al. 2024b), which was localized by *Fermil*/GBM with an uncertainty of \sim 4 deg (Fermi GBM Team 2024e). GOTO rapidly responded to the trigger, tiling 277.9 deg² within the 90 per cent GBM localization region and covering \sim 84 per cent of the total probability within 1.6 h. The afterglow was discovered at $L \sim 17.2$ mag, later confirmed through multiwavelength follow-up and spectroscopy to lie at a redshift of z = 2.681 (L. Izzo et al. 2024). Although this event is not part of the core LGRB sample analysed here, it highlights GOTO's capabilities to detect optical afterglows from both long and short GRBs, even under challenging localization conditions. A detailed analysis of GRB 241105A is presented in a separate paper by Dimple et al. (2025).

3 THE GRB SAMPLE

Our sample comprises seven LGRBs whose optical afterglows were discovered by GOTO in 2024: two *MAXI*–triggered events (GRBs 240122A and 240225B) identified serendipitously, and five *Fermi*–triggered events (GRBs 240619A, 240910A, 240916A, 241002B, and 241228B) detected in responsive mode. This section begins by discussing the prompt high-energy triggers and observations of these seven GRBs. The basic properties of the GRBs in our sample are listed in Table 1. The detection circumstances provide essential context – in particular, the trigger times, localization accuracy, and alert distribution – that directly influenced GOTO's follow-up strategy, as discussed above in Section 2.2. The subsequent subsections describe the localization, follow-up coverage, and an observational summary of the seven LGRBs in our sample.

3.1 High-energy triggers

The GOTO follow-up campaigns for GRBs in our sample were initiated by triggers from the *MAXI/GSC* (M. Matsuoka et al. 2009; T. Mihara et al. 2011) and the *Fermi/GBM* (C. Meegan et al. 2009). We briefly summarize below the specific GRBs that prompted these observations. Fig. 3 shows the 90 per cent containment localization regions provided by the triggering satellites.

3.1.1 MAXI/GSC GRBs 240122A and 240225B

GRB 240122A was detected by the MAXI/GSC on 2024 January 22 at 10:28:03 UT in the 2-10 keV range (H. Negoro et al. 2024).

^bGalactic extinction values are estimated following recalibrated dust maps of E. F. Schlafly & D. P. Finkbeiner (2011).

^csee Section 6.3

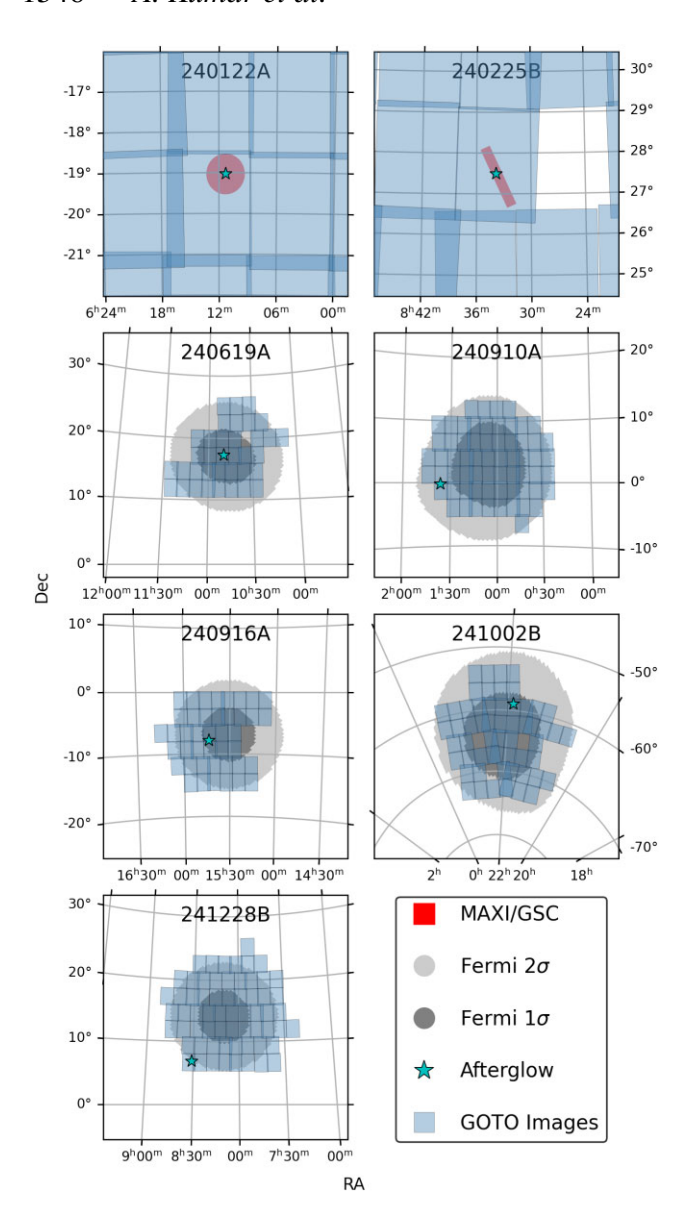


Figure 3. GOTO coverage of each of the GRBs in the sample. The first two plots denote the 90 per cent containment *MAXI/GSC* localizations (red) in a 3° \times 3° field. The localization areas are generated based on information from their discovery GCNs. The following five plots show *Fermi/GBM* localizations (grey) and the 1 and 2 σ contours from their respective HEALPIX skymaps in a 20° \times 20° field. In all plots, the 2D footprint of GOTO images taken in the first 10 h post-trigger that overlap the localizations are shown in light blue. The corresponding afterglow positions are marked with a cyan star.

The burst was localized to RA = $06^h11^m18^s$ and Dec = $-19^\circ01'51''$ (J2000), with an uncertainty of 30 arcmin. This event was detected solely by *MAXI/GSC*, with no additional high-energy instruments reporting a detection. Due to the large localization uncertainty, it was not followed up by narrow-field optical instruments but represented a good candidate for wide-field facilities such as GOTO.

MAXI/GSC triggered GRB 240225B on 2024 February 25 at 20:15:46 UT in the 4–10 keV range (M. Nakajima et al. 2024). The burst was localized to RA = $08^h33^m49^s$ and Dec = $+27^\circ29'13''$ (J2000), with a statistical 90 per cent confidence level elliptical error region, where the semimajor and semiminor axes have radii of 0.13° and 0.11°, respectively (see Fig. 3). The burst was also observed

by several other high-energy instruments, including *AstroSai*'s Cadmium Zinc Telluride Imager (CZTI) in the 20–200 keV band, and the CsI anticoincidence detectors in the 100–500 keV band (J. Joshi et al. 2024). Additional detections include *INTEGRAL* SPI–Anti-Coincidence Shield (SPI–ACS) in energies $\gtrsim\!80$ keV, the CALET Gamma-ray Burst Monitor (CGBM) in the 100–500 keV range and coverage up to 40–1000 keV (Y. Kawakubo et al. 2024), *Konus*-Wind up to $\sim\!3$ MeV (D. Frederiks et al. 2024), and the *Glowbug* gamma-ray telescope in the 10–10 000 keV range (C. C. Cheung et al. 2024).

3.1.2 Fermi/GBM GRBs 240619A, 240910A, 240916A, 241002B, and 241228B

GRB 240619A triggered the *Fermi/*GBM on 2024 June 19 at 03:43:31 UT in the 50–300 keV band (Fermi GBM Team 2024a; S. Dalessi, C. Meegan & Fermi Gamma-ray Burst Monitor Team 2024). The burst was localized to RA = $10^{\rm h}48^{\rm m}00^{\rm s}$ and Dec = $+17^{\circ}18'00''$ (J2000), with a statistical uncertainty of 1.6° , which is circularized 90 per cent containment radius $R_{\rm err,90}$ in degrees (see Fig. 3 and column two of Table 2). In addition to *Fermi/*GBM, the burst was also detected by the CALET CGBM in the 40–1000 keV band (S. Torii et al. 2024), *Konus*—Wind up to \sim 10 MeV (D. Svinkin et al. 2024), and the 1U-sized CubeSat *GRBAlpha* in the 70–890 keV band (M. Dafcikova et al. 2024a).

GRB 240910A triggered the *Fermi/*GBM on 2024 September 10 at 04:00:44 UT (Fermi GBM Team 2024b). The event was localized to RA = $01^h00^m00^s$ and Dec = $+04^\circ30'00''$ (J2000), with a statistical uncertainty of 4.5°. This burst was also picked up by the *SVOM/*GRM operating in the 15 keV–5 MeV range (SVOM/GRM Team 2024), as well as by the 1U CubeSat *GRBAlpha* (J. Ripa et al. 2024).

GRB 240916A, detected by the *Fermi/GBM* at 01:22:56 UT on 2024 September 16 (Fermi GBM Team 2024c; O. J. Roberts, C. Meegan & Fermi Gamma-ray Burst Monitor Team 2024a), was localized to RA = $15^{\rm h}32^{\rm m}00^{\rm s}$ and Dec = $-07^{\circ}05'00''$ (J2000) with a statistical uncertainty of 1.2°. Additional high-energy observations were made by the *INTEGRAL/SPI*–ACS (D. Pawar 2024) and by the 1U CubeSat *GRBAlpha* (M. Dafcikova et al. 2024b).

GRB 241002B triggered the *Fermi/GBM* at 06:14:18.76 UT on 2024 October 2 (Fermi GBM Team 2024d; O. J. Roberts et al. 2024b). The burst was localized to RA = $22^h15^m00^s$ and Dec = $-64^\circ17'00''$ (J2000), with a statistical uncertainty of 3.7°. It was also observed by the *Swift* Burst Alert Telescope–Gamma-ray Urgent Archiver for Novel Opportunities (*Swift/BAT*–GUANO; J. DeLaunay et al. 2024a).

GRB 241228B triggered the *Fermi*/GBM at 04:13:05.39 UT on 2024 December 28 (Fermi GBM Team 2024f; L. Scotton, C. Meegan & Fermi Gamma-ray Burst Monitor Team 2024). The burst was localized to RA = $08^{\rm h}08^{\rm m}00^{\rm s}$ and Dec = $+14^{\circ}00'00''$ (J2000), with a statistical uncertainty of 1.7° . It was also detected by the *Swift*/BAT–NITRATES system (J. DeLaunay et al. 2024b), with the position consistent with the GBM localization. In addition, the *Fermi* Large Area Telescope (LAT) observed high-energy emission (> 100 MeV) from this burst, including a 16 GeV photon detected 31 s after the trigger (N. Di Lalla et al. 2025).

These prompt high-energy detections by Fermi/GBM provided the initial localization constraints and trigger alerts that enabled rapid optical follow-up by GOTO. The diversity in localization uncertainties influenced the choice of tiling patterns and observing cadences. In the following section, we present the optical afterglow

Table 2. Summary of GOTO's coverage of the *Fermi/GBM* GRBs in our sample. For each event, we list the *Fermi/GBM*-reported 90 per cent localization uncertainty ($R_{\text{err.}90}$), number of images, sky coverage area, enclosed probability, and mean 5σ L-band limiting magnitude.

GRB	R _{err,90} (deg)	No. of images	Coverage (deg ²)	Prob. enclosed (per cent)	Mean 5σ depth (mag)
240619A	1.6	56	151.5	85.7	18.6
240910A	4.5	191	295.3	90.3	20.0
240916A	1.2	41	178.6	78.3	19.1
241002B	3.7	58	273.1	84.9	20.3
241228B	1.7	165	214.0	89.9	19.8

localizations and follow-up coverage, highlighting how the prompt trigger information shaped the subsequent GOTO observations.

3.2 Localization coverage and optical afterglow discoveries

Fig. 3 provides an overview of the sky localization and follow-up coverage for the GRBs analysed in this study (GRBs 240122A, 240225B, 240619A, 240910A, 240916A, 241002B, and 241228B), based on GOTO observations obtained within the first 24 h posttrigger. The dark and light grey contours represent the 1σ and 2σ localization regions extracted from the HEALPIX (K. M. Górski et al. 2005) probability skymaps. Light blue shading denotes the GOTO fields observed within 10 h of each burst, demonstrating the system's wide-area and rapid-response capabilities. Cyan stars mark the locations of confirmed optical afterglows, showing that GOTO's coverage either enclosed or closely bordered the true source positions in all cases. In addition, the finding charts highlighting the confirmed afterglows, derived from GOTO observations, are presented in panels (a)-(g) of Fig. 4. For context, each GOTO cutout is paired with a corresponding image from Legacy Survey (LS) DR10 covering the same ~ 6.3 arcmin $\times 6.3$ arcmin FoV; for GRB 240122A, a Pan-STARRS DR1 image is shown instead.

3.2.1 MAXI/GSC GRBs 240122A and 240225B: arcminute-scale localization

GOTO does not follow up MAXI triggers in responsive mode, as MAXI alerts are not distributed in a machine-readable format that can be ingested automatically by the sentinel. Instead, these fields are only covered serendipitously in survey mode. In Fig. 3, the top row shows the two events detected by MAXI/GSC, GRB 240122A, and GRB 240225B, each displayed within a $3^{\circ} \times 3^{\circ}$ FoV. The red shaded regions indicate the approximate localization areas from MAXI/GSC reports. For GRB 240122A, the afterglow is well centred within the localization and fully encompassed by the GOTO field. In contrast, for GRB 240225B, the GOTO tiling intersected the elongated error region, providing timely coverage that included the eventual afterglow position.

GRB 240122A: GOTO-S serendipitously observed the localization region of GRB 240122A during its routine all-sky survey on 2024 January 22, discovering the optical afterglow (GOTO24eu/AT2024apy) at J2000 coordinates $RA = 06^h 12^m 12^s.91$ and $Dec = -19^\circ 08'38''.81$. The afterglow was detected at 11:11:43 UT ($T_0+43.68$ min) with an $T_0+43.68$ min) with an $T_0+43.68$ min) with an $T_0+43.68$ min Fig. 3 (top-left), the GOTO FoV comfortably covers the compact $T_0+43.68$ min Pig. 3 (top-left), the GOTO FoV comfortably covers the compact $T_0+43.68$ min Pig. 3 (top-left), the GOTO FoV comfortably covers the compact $T_0+43.68$ min Pig. 3 (top-left), the GOTO FoV comfortably covers the compact $T_0+43.68$ min Pig. 3 (top-left), the GOTO FoV comfortably covers the compact $T_0+43.68$ min Pig. 3 (top-left), the GOTO FoV comfortably covers the compact $T_0+43.68$ min Pig. 3 (top-left), the GOTO FoV comfortably covers the compact $T_0+43.68$ min Pig. 3 (top-left), the GOTO FoV comfortably covers the compact $T_0+43.68$ min Pig. 3 (top-left), the GOTO FoV comfortably covers the compact $T_0+43.68$ min Pig. 3 (top-left), the GOTO FoV comfortably covers the compact $T_0+43.68$ min Pig. 3 (top-left), the GOTO FoV comfortably covers the compact $T_0+43.68$ min Pig. 3 (top-left), the GOTO FoV comfortably covers the compact $T_0+43.68$ min Pig. 3 (top-left), the GOTO FoV comfortably covers the compact $T_0+43.68$ min Pig. 3 (top-left), the GOTO FoV comfortably covers the compact $T_0+43.68$ min Pig. 3 (top-left), the GOTO FoV comfortably covers the compact $T_0+43.68$ min Pig. 3 (top-left), the GOTO FoV comfortably covers the compact $T_0+43.68$ min Pig. 3 (top-left), the GOTO FoV comfortably covers the compact $T_0+43.68$ min Pig. 3 (top-left), the GOTO FoV comfortably covers the compact $T_0+43.68$ min Pig. 3 (top-left), the GOTO FoV comfortably covers the compact $T_0+43.68$ min Pig. 3 (top-left), the GOTO FoV comfortably covers the compact $T_0+43.68$ min Pig. 3 (top-left), the GOTO FoV comfortably covers the compa

GRB 240225B: Similarly, GOTO-N serendipitously covered the field of GRB 240225B and discovered its optical afterglow (GOTO24tz/AT2024dgu) at J2000 coordinates RA = $08^{\rm h}33^{\rm m}26^{\rm s}$.67 and Dec = $+27^{\circ}04'32''$.71. The counterpart was first detected on 2024 February 25 at 21:45:51 UT ($T_0+1.50\,\rm h$) at $17.12\pm0.04\,\rm mag$ ($L-{\rm band}$) and was last detected the following night at 22:10:38 UT ($T_0+25.91\,\rm h$) at $19.69\pm0.18\,\rm mag$ (B. P. Gompertz et al. 2024a). As shown in Fig. 3 (top-right), the GOTO tiling intersected the elongated MAXI/GSC localization, with the afterglow located near the centre of the observed field.

3.2.2 Fermi/GBM GRBs 240619A, 240910A, 240916A, 241002B, and 241228B: degree-scale localization

Fermi/GBM triggers are distributed in real time via machine-readable GCN notices, which the GOTO sentinel ingests automatically. This enables fully responsive follow-up, with observations scheduled immediately after the alert is received. Follow-up observations are carried out as soon as observing conditions and visibility constraints permit. The five different panels in Fig. 3 correspond to events detected by Fermi/GBM GRBs 240619A, 240910A, 240916A, 241002B, and 241228B, each displayed over a wider $20^{\circ} \times 20^{\circ}$ field. A quantitative summary of GOTO follow-up coverage for the Fermi/GBM GRBs in our sample is provided in Table 2. For each event, we list the GBM localization uncertainty (expressed as the circularized 90 per cent containment radius in degrees), number of images obtained to cover the 90 per cent GBM localization region, the total sky area imaged, the fraction of localization probability enclosed within the observed fields, and the mean 5σ limiting magnitude. The two MAXI/GSC GRBs are not included here, as their compact localizations were fully covered serendipitously by single $\sim 9 \text{ deg}^2$ survey pointings.

GRB 240619A: GOTO-S initiated targeted follow-up observations of GRB 240619A on 2024 June 19 at 08:24:01 UT (T_0 +4.68 h), continuing until 21:48:35 UT ($T_0+18.08\,\mathrm{h}$). As illustrated in Fig. 3 (second row; left panel), the GOTO tiling successfully overlapped the 1σ and 2σ HEALPIX contours from the Fermi/GBM localization, with the afterglow position (blue star) falling within the observed fields obtained in the first 10 h. The afterglow (GOTO24cvn/AT2024lwv) was identified in these data at J2000 coordinates $RA = 10^{h}49^{m}34^{s}.70$ and $Dec = +17^{\circ}16'58''.07$, with detections by GOTO-S at 08:24:50 UT $(T_0+4.69 \text{ h})$ and by GOTO-N at 21:40:50 UT $(T_0+18.00 \text{ h})$, exhibiting L-band magnitudes of 17.17 \pm 0.17 and 18.38 \pm 0.09 mag, respectively (B. P. Gompertz et al. 2024b), details are tabulated in Table 1. Although the afterglow was first discovered by GOTO, the position was also serendipitously covered by the ATLAS all-sky survey (J. L. Tonry et al. 2018), which provides a forced photometric detection at an earlier epoch. The source is detected in the ATLAS forced photometry data with an o-band (560-820 nm) magnitude of 16.24 ± 0.01 at $T_0 + 2.53$ h and 18.72 ± 0.12 at $T_0 + 26.71$ h, retrieved

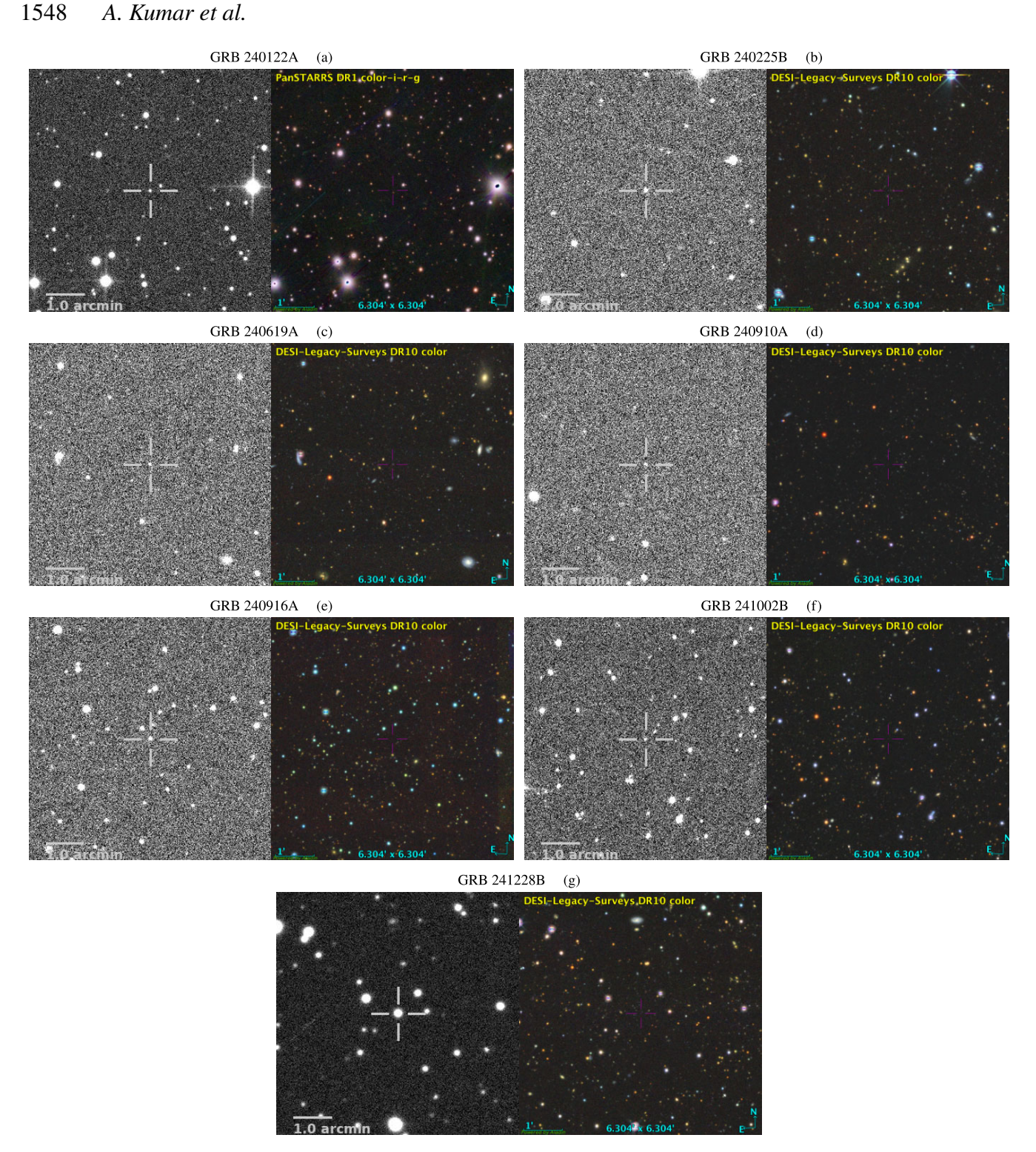


Figure 4. Finding charts of GRBs 240122A, 240225B, 240619A, 240910A, 240916A, 241002B, and 241228B in the GOTO L-band (400-700 nm) observed by GOTO. Each cutout is a 300 × 300 pixel region centred on the transient, corresponding to a FoV of ~6.3 arcmin ×6.3 arcmin at the GOTO pixel scale of 1.26 arcsec pix⁻¹. For comparison, survey images from the Legacy Survey DR10 are shown (except for GRB 240122A, where a Pan-STARRS DR1 image is used), matched to the same FoV. Details of each object are listed in Table 1.

from the ATLAS Forced Photometry Server (L. Shingles et al. 2021). While ATLAS did not identify the transient in real time, its archival data proved valuable in constraining the early-time brightness and confirming the fading behaviour consistent with an optical afterglow (B. P. Gompertz et al. 2024b).

GRB 240910A: GOTO-S began targeted follow-up observations of GRB 240910A on 2024 September 10 at 12:25:28 UT $(T_0+8.41 \text{ h})$, continuing through to 16:33:57 UT $(T_0+12.55 \text{ h})$. As shown in Fig. 3 (second row; right panel), the GOTO coverage successfully intersected the high-probability localization contours,

with the afterglow position clearly lying within the imaged area. The afterglow (GOTO24fvl/AT2024vfp) was discovered at J2000 coordinates RA = $01^{\rm h}36^{\rm m}23^{\rm s}.45$ and Dec = $-00^{\circ}12'17''.86$, with detections spanning from 13:26:31.776 UT ($T_0+9.43$ h) to 16:01:36 UT ($T_0+12.01$ h), yielding L-band magnitudes of 19.32 \pm 0.13 and 19.74 \pm 0.12 mag, respectively (Y. Julakanti et al. 2024a).

GRB 240916A: GOTO-S began targeted follow-up observations of GRB 240916A on 2024 September 16 at 09:06:47 UT ($T_0+7.73$ h), continuing until 09:23:05 UT ($T_0+8.00$ h). As seen in Fig. 3 (third row; left panel), the GOTO tiling intersected the high-probability regions of the localization, successfully encompassing the afterglow site. The afterglow (GOTO24fzn/AT2024vlp) was identified at J2000 coordinates RA = $15^{\rm h}43^{\rm m}39^{\rm s}.229$ and Dec = $-07^{\circ}45'53''.22$, with a detection at 09:06:47.81 UT ($T_0+7.73$ h) at an L-band magnitude of 17.80 \pm 0.05 mag (B. P. Gompertz et al. 2024c).

GRB 241002B: GOTO-S conducted targeted follow-up observations of GRB 241002B starting on 2024 October 2 at 09:17:03 UT ($T_0+3.05\,\text{h}$), concluding at 09:40:00 UT ($T_0+3.43\,\text{h}$). As shown in Fig. 3 (third row; right panel), the observed GOTO fields overlapped the high-probability regions of the *Fermi/GBM* localization, with the afterglow position included within the footprint. The afterglow (GOTO24gpc/AT2024xbg) was discovered at J2000 coordinates RA = $21^{\text{h}}53^{\text{m}}16^{\text{s}}.56$ and Dec = $-58^{\circ}56'51''.98$, with a detection at 09:17:20 UT ($T_0+3.05\,\text{h}$) at an L-b magnitude of $19.53\pm0.09\,\text{mag}$ (A. Kumar et al. 2024c).

GRB 241228B: GOTO-N initiated follow-up observations of GRB 241228B on 2024 December 28 at 04:26:19 UT $(T_0+0.22 \text{ h})$, continuing through to 23:24:22 UT $(T_0+19.19 \text{ h})$. As depicted in Fig. 3 (bottom-left panel), the GOTO tiling efficiently covered the high-probability localization region, including the afterglow position. The afterglow (GOTO24jmz/AT2024afgu) was identified by GOTO-N at J2000 coordinates $RA = 08^{h}31^{m}05^{s}.46$ and Dec = $+06^{\circ}50'54''.07$, with an initial detection at 04:32:24 UT ($T_0+0.32 \text{ h}$) at an L-band magnitude of 14.54 ± 0.01 mag. Multiple detections followed throughout the observing sequence, with the final GOTO-N detection recorded at 13:00:42 UT ($T_0+8.79\,\mathrm{h}$) at 19.70 \pm 0.10 mag (A. Kumar et al. 2024d). The afterglow candidate for GRB 241228B falls on the 94.5 per cent probability contour, formally outside the GBM 90 per cent localization region. While most GRB afterglows are found within the 90 per cent contour, a small fraction are expected to lie just beyond it, making GRB 241228B a noteworthy case.

4 AFTERGLOW FOLLOW-UP OBSERVATIONS

In addition to the discovery imaging provided by GOTO, we carried out a coordinated programme of multiwavelength follow-up to characterize the afterglows of our GRB sample. These observations span the X-ray, UV, optical, and radio regimes, enabling us to track the temporal evolution and spectral energy distributions of the counterparts. The combined data set allows us to constrain the physical properties of the bursts, verify their association with the optical transients identified by GOTO, and provide essential input for modelling their afterglow emission.

Figs 5(a)–(g) illustrates the timeline of the multiwavelength follow-up campaigns for all GRBs in the sample, marking the epochs at which each facility recorded its first observation relative to the trigger time. The various phases of the events are colour-coded as follows: X-ray afterglow (blue), UV/optical/NIR afterglow (green), radio afterglow (purple), and prompt emission (red) for completeness. This timeline highlights the wide temporal coverage and the rapid, coordinated response from both ground- and space-based observatories across the electromagnetic spectrum for the GRBs in our sample. More observation details are provided below.

A full log of photometric measurements, combining GCN Circular reports and data from this work, is presented in Tables A1 and A2, while Table 3 summarizes the spectroscopic campaigns.

4.1 X-ray

The XRT onboard *Swift* (D. N. Burrows et al. 2005) performed follow-up observations in response to our target-of-opportunity (ToO) requests, with exposures ranging from 1.3 to 3.6 ks depending on the GRB, and all data were collected in Photon Counting (PC) mode. X-ray data, including light curves, calibrated event files, and spectra, were retrieved from the public *Swift/XRT* GRB Catalogue hosted by the UK Swift Science Data Centre⁵ and processed using the standard XRT pipeline as described in P. A. Evans et al. (2007, 2009). All light curves and spectra were generated using the automated tools provided by the XRT team.

XRT detected X-ray afterglows for all seven events, with uncatalogued sources coincident with or close to the GOTO optical transient locations in each case. The corresponding 0.3–10 keV light curves (in counts $\rm s^{-1}$) for the seven GRBs 240122A, 240225B, 240619A, 240910A, 240916A, 241002B, and 241228B, together with comparison GRBs, and spectra (in counts $\rm s^{-1}\,keV^{-1}$) for our sample are discussed later in Section 6.1.

4.2 UV/Optical/NIR photometric observations

Follow-up afterglow observations in the UV/optical/NIR, including data from both the GCN Circulars and this work, are compiled in Table A1. The table provides details on the observing facilities, instruments used, measured magnitudes, and other relevant parameters. Fig. 6 shows the extinction-corrected UV/optical/NIR afterglow light curves and the wavelength coverage of all filters used (passbands in nm).

While GOTO primarily contributed discovery optical observations for the GRBs in our sample, its relatively small aperture and lack of multiple band observations limit its utility for extended follow-up. Details of the GOTO observations and initial detection magnitudes have been presented in Section 3.2. Therefore, GOTO observations are not included in this section. Instead, this section focuses on subsequent optical afterglow follow-up observations obtained with a range of facilities situated around the globe.

4.2.1 Swift/UVOT

In addition to XRT, *Swift* simultaneously observes with its UV-Optical Telescope (UVOT; P. W. A. Roming et al. 2005). We obtained the resulting data from the UK *Swift* Science Data Centre⁶ (UKSSDC) and used UVOTPRODUCT V2.9⁷ to measure the photometry of the afterglow. We used a 5 arcsec radius circular aperture centred at the positions noted in Section 3.2 and a detection threshold of 3σ . The measured magnitudes were converted from the UVOT photometric system to AB using the standard UVOT zeropoints (A. A. Breeveld et al. 2011). The afterglow was detected in at least one epoch for five of the seven sources in our sample. The exceptions are GRB 240122A, where the UVOT FoV did not cover the source position, and GRB 240225B, for which no UVOT

⁵https://www.swift.ac.uk/

⁶https://www.swift.ac.uk/index.php

⁷As part of HEASOFT V6.32 (Nasa High Energy Astrophysics Science Archive Research Center (Heasarc)Nasa High Energy Astrophysics Science Archive Research Center (Heasarc) 2014).

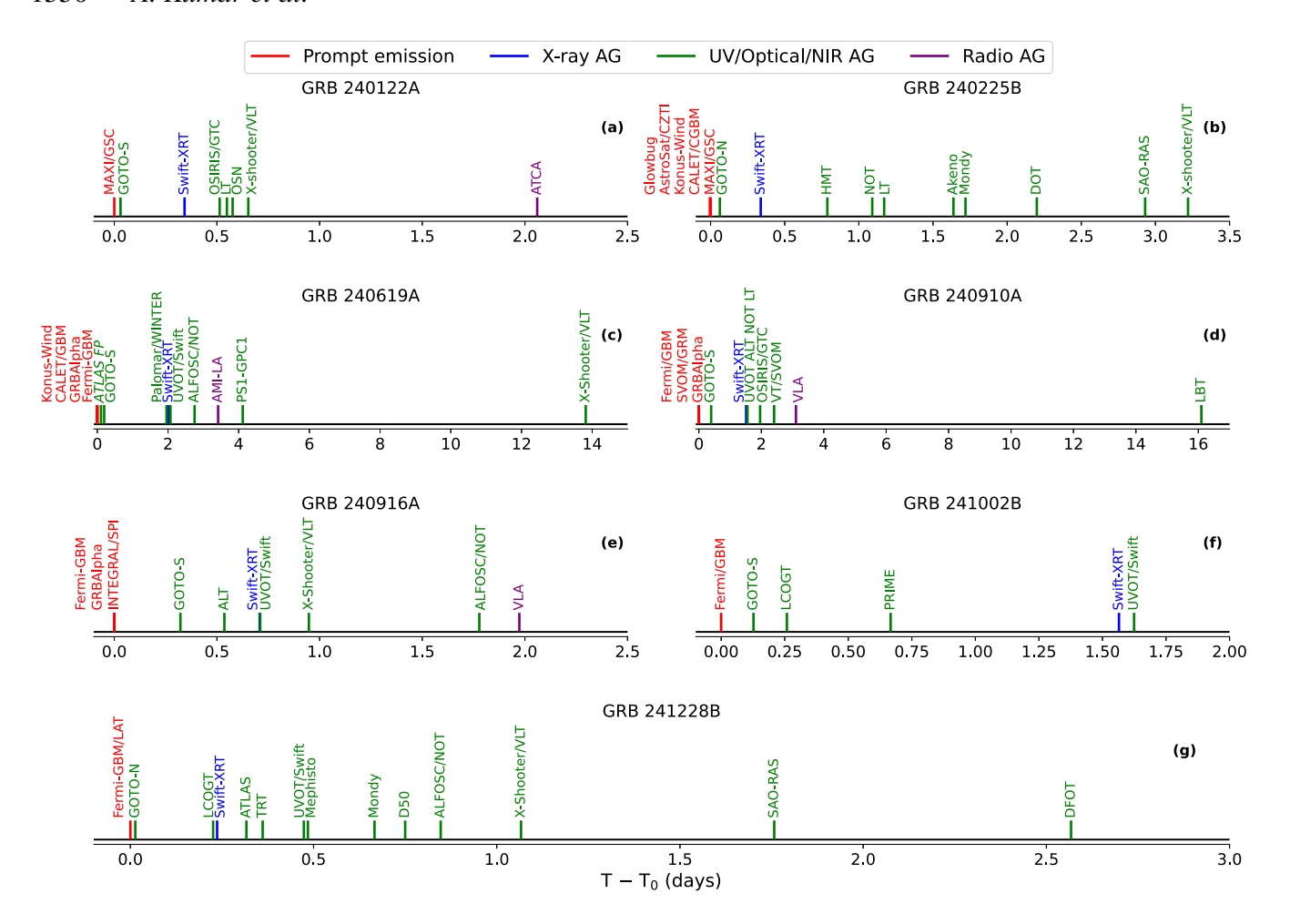


Figure 5. First detection times across various observatories for GRBs in our sample. Shown are prompt (red), X-ray afterglow (blue), UV/optical/NIR afterglow (green), and radio afterglow (purple) observations from both space- and ground-based facilities. In all cases, GOTO discovered the optical afterglow following the prompt emission. For GRB 240619A, although ATLAS has the earliest epoch, the afterglow was first discovered by GOTO, and the ATLAS data were serendipitously pre-covered and used in the GOTO discovery report (B. P. Gompertz et al. 2024b).

Table 3. Log of spectroscopic afterglow observations for the GRBs analysed in this work. Redshift values are included here for completeness; detailed measurement methods behind estimating these values are described in Section 6.3.

GRB	Date-Obs	T-T ₀ (h)	Telescope	Instrument	Exp. Time	Slit width (arcsec)	Airmass	Seeing (arcsec)	Redshift
240122A	2024-01-22 22:56:23 UT	12.47	GTC	OSIRIS	3 × 900 s	1.0	1.50	1.70	3.1634 ± 0.0003
240122A	2024-01-23 02:25:01 UT	15.95	VLT	X-shooter	$4 \times 1200 \text{ s}$	1.0^{a} – 0.9^{b}	1.00-1.01	0.45 - 0.49	3.1634 ± 0.0003
240225B	2024-02-29 01:45:36 UT	77.52	VLT	X-shooter	$4 \times 1200 \text{ s}$	1.0^{a} – 0.9^{b}	1.61 - 1.65	0.66 - 0.70	0.9462 ± 0.0002
240619A	2024-07-02 23:20:52 UT	331.68	VLT	X-shooter	$4 \times 600 \text{ s}$	1.0^{a} – 0.9^{b}	1.90-2.00	0.94-0.96	0.3960 ± 0.0001
240910A	2024-09-12 03:08:33 UT	47.13	GTC	OSIRIS	$3 \times 1200 \text{ s}$	1.0	1.14	0.80	1.4605 ± 0.0007
240916A	2024-09-17 00:08:31 UT	22.76	VLT	X-shooter	$4 \times 600 \text{ s}$	1.0^{a} – 0.9^{b}	1.74-1.99	1.07-1.09	2.6100 ± 0.0002
241228B	2024-12-29 06:00:45 UT	25.68	VLT	X-shooter	$4 \times 1200 \text{ s}$	$1.0^a - 0.9^b$	1.17-1.18	0.53-0.54	2.6745 ± 0.0004

Note. aUVB arm, bVIS and NIR arms.

data were obtained. The UVOT follow-up observations are listed in Table A1, and the corresponding light curves are presented in Fig. 6.

4.2.2 LT

The IO:O Imager at the robotic 2m Liverpool Telescope (LT; I. A. Steele et al. 2004) located at the international Observatorio del Roque de los Muchachos, La Palma, was triggered for follow-up

of GRBs 240122A, 240225B, and 240910A. For GRBs 240122A and 240910A, one epoch was obtained in each of riz bands. For GRB 240225B, one epoch is in griz, and three later epochs were secured in r—band. All LT data were pre-reduced for bias, dark, and flat-field corrections using the facility pipeline. The photometry was then extracted with the photometry-sans-frustration pipeline (psf; M. Nicholl et al. 2023), making use of its built-in template subtraction. The observations are summarized in Table A1, and the corresponding light curves are shown in Fig. 6.

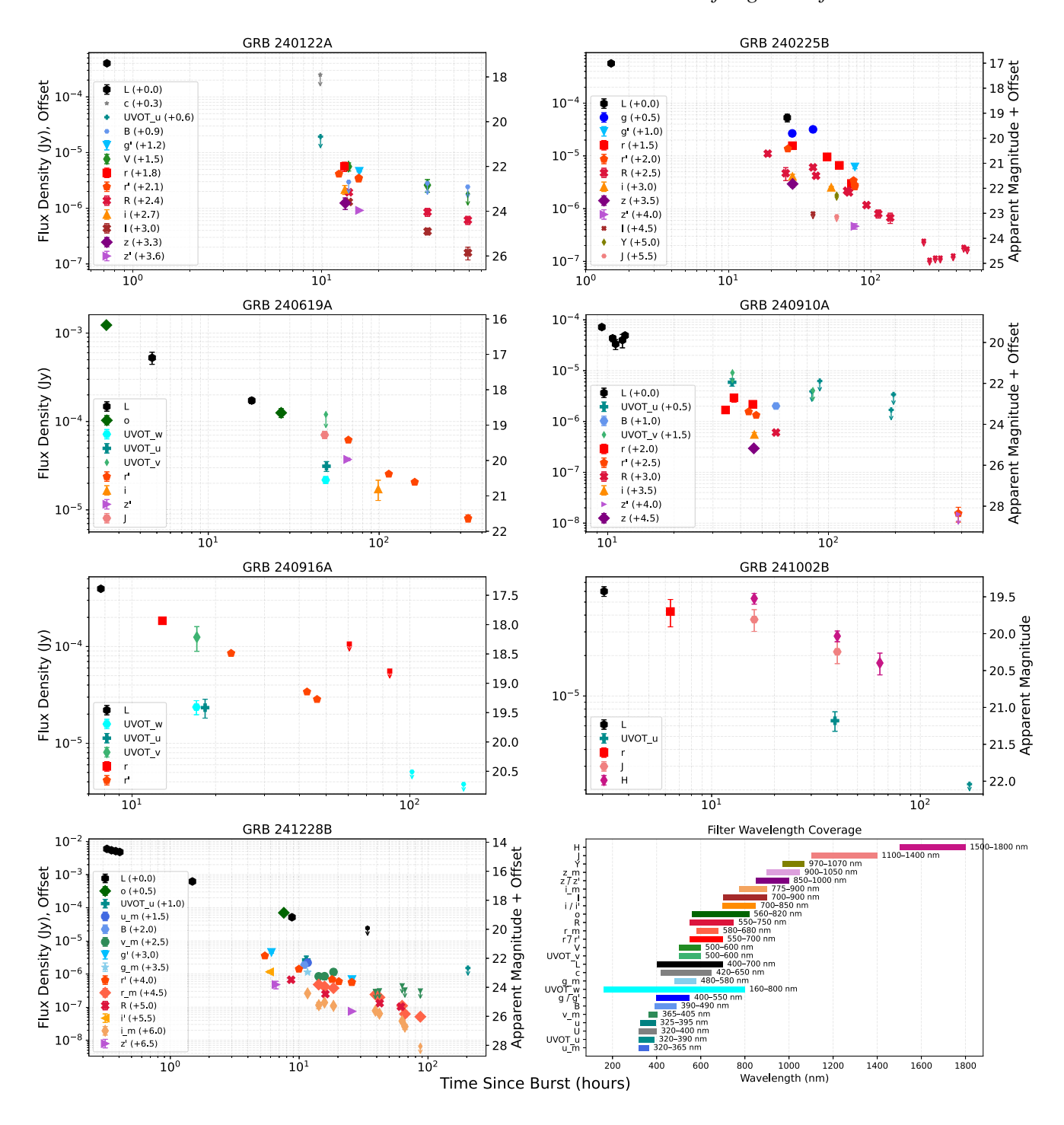


Figure 6. UV/optical/NIR afterglow photometry for GRBs 240122A, 240225B, 240619A, 240910A, 240916A, 241002B, and 241228B, combining our measurements with values compiled from GCN Circulars (see Table A1). Left ordinates show flux density (Jy) and right ordinates show AB magnitude; corrected for foreground extinction. Downward arrows indicate non-detections (3σ upper limits). To reduce crowding, per-band vertical magnitude offsets are applied as noted in each legend; an offset of Δm corresponds to a multiplicative factor of $10^{-0.4\Delta m}$ on the flux axis. Time is measured relative to the trigger ($T-T_0$): we adopt the MAXI T_0 for GRBs 240122A and 240225B and the Fermi T_0 for the remaining five bursts. The bottom-right panel summarizes the approximate passband coverage (nm) of all UV/optical/NIR filters used.

4.2.3 NOT

The Nordic Optical Telescope (NOT; A. A. Djupvik & J. Andersen 2010) is a 2.56 m telescope located at the Observatorio del Roque de los Muchachos in La Palma (Canary Islands, Spain). The NOT routinely performs ToO observations of GRB and FXT

afterglows. The NOT observed and detected the counterparts of GRBs 240225B, 240619A, 240910A, 240916A, and 241228B using the Alhambra Faint Object Spectrograph and Camera (ALFOSC) optical imager. The reduction of the NOT data follows standard procedures, including bias and flat-field correction. The photometric calibration was computed against the Pan-STARRS catalogue.

Details of these measurements are provided in Table A1, with their temporal evolution illustrated in Fig. 6.

4.2.4 VLT/X-shooter acquisition camera

The X-shooter spectrograph (J. Vernet et al. 2011) mounted on Unit Telescope 3 (Melipal) of the Very Large Telescope (VLT) at Cerro Paranal Observatory was triggered for follow-up of a subset of GRBs in our sample.

Prior to the spectroscopic observations (see Section 4.3.1), acquisition images were obtained with the acquisition and guiding (A&G) camera in the Sloan g', r', and z' bands, depending on the target. These images were used to verify the target acquisition and also provide valuable photometric information on the afterglow. The raw frames were reduced using a custom pipeline based on ccdproc (M. Craig et al. 2017), including bias subtraction and flat-field correction.

Astrometric calibration was applied using *Astrometry.net* (D. Lang et al. 2010), and the images were aligned and stacked where appropriate. Aperture photometry was performed using photutils (L. Bradley et al. 2024), and the zero-point was calibrated against Pan-STARRS DR2 field stars. A log of the observations is given in Table A1, and the resulting light curves are presented in Fig. 6.

4.2.5 BOOTES

The Burst Observer and Optical Transient Exploring System (BOOTES) 8 observed GRB 240122A using the 60 cm robotic telescope at the BOOTES-2/TELMA station in La Mayora, Málaga, Spain. Observations began on 2024 January 22 at 19:44:56 UT, approximately 9.3 h after the trigger. A series of 60 s exposures were obtained with a clear filter. The afterglow was faint and remained undetected in both individual frames and the stacked image. A 3σ upper limit was derived, as listed in Table A1.

4.2.6 OSN

The follow-up observations of GRB 240122A are also performed with the 1.5 m telescope at the Sierra Nevada Observatory (OSN, Granada, southern Spain), targeting the burst position starting on 2024 January 22 at 23:45:57 UT (13.3 h post-trigger). The afterglow was clearly detected during the first night, prompting continued monitoring over the following two nights (January 23 and 24). Observations across all three epochs were performed in the Johnson-Cousins B, V, R, and I bands, with exposure times of 90 s and 150 s. The afterglow remained clearly visible in the stacked images. Photometric measurements were obtained via aperture photometry using standard procedures in the IRAF software package (D. Tody 1986), following bias subtraction and flat-field correction. Magnitudes were calibrated against nearby reference stars in the field, listed in the SDSS catalogue, using the transformation equations from R. H. Lupton et al. (2005). 10 The resulting magnitudes are reported in Table A1, while Fig. 6 displays the corresponding light curves.

4.2.7 1.5 m AZT-33IK Mondy

The AZT-33IK 1.5-m telescope at the Sayan Solar Observatory (ISTP SB RAS), located near the village Mondy in Buryatia, was triggered

for the follow-up observations of GRB 240225B on 2024 February 27 at 13:01:23 UT. A series of 30 images with an individual exposure of 120 s was obtained using the Andor NEO CMOS photometer attached to the telescope. The observations were carried out using the Johnson R-filter. Aperture photometry of the stacked image from the entire series yielded a magnitude for the optical afterglow of $R=19.72\pm0.07$ (AB). We continued observations with AZT-33IK until the 2024 March 17 epoch.

We processed all our observations using the APEX pipelines (A. V. Devyatkin et al. 2010; V. Kouprianov 2012; N. Pankov et al. 2022). The process involved image calibration (dark frame subtraction, flat-fielding, cosmic-ray removal), image quality control, image stacking, and source extraction. The apex_forced_phot pipeline was utilized for the forced photometry of the GRB 240225B afterglow on difference images. Image subtraction with the method described in A. B. Tomaney & A. P. S. Crotts (1996), was performed by apex_subtract pipeline, using Pan-STARRS-DR1 survey images as a reference obtained from HIPS2FITS service (T. Boch et al. 2020). This step ensured that the underlying host galaxy, presented in the Legacy Survey DR9 with a magnitude of $r \sim 24.2$ and a photometric redshift of $z \sim 0.9$, did not affect the afterglow measurement.

We note an LS DR10 source at the coordinates RA = $08^{\rm h}33^{\rm m}26^{\rm s}.06$ and Dec = $+27^{\circ}04'32''.9$ (8 arcsec West of the afterglow position) with a magnitude of $r \sim 22.4$ that may affect the photometry in the images with poor seeing. The apparent magnitudes were initially calibrated against three nearby USNO-B1.0 stars (identifiers are 1171-0194062, 1171-0194079, and 1171-0194031) in the Vega system and then converted to the AB system using standard Vega-to-AB magnitude conversion. ¹² The complete record of these observations is compiled in Table A1, and their light curves are plotted in Fig. 6.

4.2.8 LBT

We obtained late-time r'z' imaging of GRB 240910A with the Large Binocular Cameras (LBCs; E. Giallongo et al. 2008) mounted on the Large Binocular Telescope (LBT) on Mt. Graham, Arizona, USA (Program ID: IT-2024B-023). LBC imaging data were reduced using the dedicated data reduction pipeline (A. Fontana et al. 2014). Aperture photometry was performed via IRAF tools and calibrated against SDSS field stars. Observation logs are reported in Table A1, with the associated light-curve behaviour shown in Fig. 6.

4.2.9 HMT

The Half-Meter Telescope (HMT) is a 50 cm wide-field telescope, located at Nanshan Station of Xinjiang Astronomical Observatory, Chinese Academy of Sciences. HMT conducted two observations during the night of 2024 February 26 (UT), 18.40 and 24.87 h since the GRB 240225B trigger, respectively. Based on the standard data processing of IRAF and aperture photometry, the measured brightness in *R*-band is listed in Table A1, and plotted in Fig. 6.

4.2.10 TRT

The Thai Robotic Telescope (TRT) is an automated telescope network comprising four 70 cm CDK700 Telescopes equipped with Andor CCD cameras, distributed in the United States (SRO),

⁸https://bootesnetwork.com/

⁹http://www.osn.iaa.es/

¹⁰ http://www.sdss.org/dr4/algorithms/sdssUBVRITransform.htm

¹¹ https://alasky.cds.unistra.fr/hips-image-services/hips2fits

¹²https://www.astronomy.ohio-state.edu/martini.10/usefuldata.html

Chile (CTO), Australia (SBO), and China (GAO). The telescope located at SBO started observations at 8.7 h after the GRB 241228B trigger and obtained $4 \times 300 \,\mathrm{s}$ frames in the R-band. The Johnson-Cousin filters were calibrated with the converted magnitude from the Sloan system.¹³ The aperture photometry is calibrated with the Pan-STARRS Data Release 2 (K. C. Chambers et al. 2016; H. Flewelling 2018) and listed in Table A1.

4.2.11 Altay

The Altay Telescopes are located at the Altay Observatory, Xinjiang, China, as part of the Altay Astronomical Time-domain Project (also known as JinShan Project). This project consists of four 50 cm telescopes with a FoV of $1.7^{\circ} \times 1.7^{\circ}$, which are named from 50A to 50B, two 100 cm telescopes with a FoV of $1.4^{\circ} \times 1.4^{\circ}$, which are named 100A and 100B, and one 100 cm telescope with a FoV of 14 arcmin \times 14 arcmin, which is named 100C. In the early commissioning stage of the project, we triggered the GRB 240910A and GRB 240916A with the 100 cm telescopes using the Sloan r-filter.

The obtained images were processed with the standard IRAF procedures, including bias and dark subtraction, flat correction, and image combination. After the astrometric calibration by *Astrometry.net* (D. Lang et al. 2010), the apparent photometric data were calibrated with the Pan-STARRS Data Release 2 (K. C. Chambers et al. 2016; H. Flewelling 2018). A comprehensive summary of the results is given in Table A1, and light curves are shown in Fig. 6.

4.2.12 1.6m Mephisto

The 1.6m Multi-channel Photometric Survey Telescope (Mephisto) is a wide-field multichannel telescope (X. Yuan et al. 2020). It is located at Lijiang Observatory of Yunnan Astronomical Observatories, Chinese Academy of Sciences, and is operated by the South-Western Institute for Astronomy Research, Yunnan University. Equipped with three-channel CCD cameras (blue uv, yellow gr, and red iz channels), Mephisto can perform simultaneous observations in ugi_m or vrz_m optical bands at a particular moment. The wavelength coverage of the u_m , v_m , g_m , r_m , i_m , and z_m filters is 320–365, 365–405, 480–580, 580–680, 775–900, and 900–1050 nm with central wavelengths at 345, 385, 529, 628, 835, and 944 nm, respectively (see e.g. Y.-P. Yang et al. 2024; Y. Cheng et al. 2025). Presently, the facility is in an advanced stage of commissioning.

Mephisto was triggered to observe GRB 241228B on 2024 December 28 (15:38:16) UT and continued until 2024 December 31. Multiple frames with an exposure time of 300 s were obtained at different epochs during the follow-up. The pre-processing of raw frames was performed using a specialized pipeline developed for the Mephisto observational data (Fang et al., in preparation). To obtain the instrumental magnitudes of the GRB, point spread function photometry was performed on the stacked images. The corrected Gaia XP low-resolution spectra (B. Huang et al. 2024) were utilized for the photometric calibration. Considering that the Mephisto bands are not fully covered by the corrected Gaia XP spectra (336- $1020 \,\mathrm{nm}$), it was extrapolated partially in the u and z Mephisto bands. Each band's synthetic magnitude in the AB system was calculated by convolving the spectra with the transmission efficiency. The median of the magnitude offset between the instrumental and synthetic magnitudes of the non-variable stars in the field was used to

finally calibrate the Mephisto photometric measurements (for details see X. Chen et al. 2024; X. Zou et al. 2025). The overall uncertainties in the photometric calibration were constrained to be within 0.03, 0.01, and 0.005 mag in the u_m , v_m , and $griz_m$ bands, respectively. The detailed data set is compiled in Table A1, and the corresponding light curves are shown in Fig. 6.

4.3 Spectroscopic observations

For the GRBs in our sample, we acquired spectra using the X-shooter instrument mounted on the VLT (J. Vernet et al. 2011), and OSIRIS (Optical System for Imaging and low-Intermediate-Resolution Integrated Spectroscopy) on the Gran Telescopio Canarias (GTC; J. Cepa 1998), except for GRB 241002B, for which we did not get any spectroscopic observation due to scheduling constraints. A complete summary of the VLT/X-shooter and GTC/OSIRIS spectroscopic configurations, exposure details, and observing conditions is provided in Table 3, whereas spectra are shown in Figs A1–A7.

4.3.1 VLT/X-shooter spectrograph

Spectroscopic observations of GRBs 240122A, 240225B, 240619A, 240916A, and 241228B were performed as part of the 'Stargate' GRB program at ESO, using the X-shooter spectrograph (J. Vernet et al. 2011), installed on the ESO VLT UT3 at Cerro Paranal, Chile. X-shooter simultaneously covers the ultraviolet-blue (UVB; 300-560 nm), visible (VIS; 550-1020 nm), and near-infrared (NIR; 1020-2100 nm) wavelength ranges, with resolving powers of $\lambda/\Delta\lambda =$ 5400, 8900, and 5600, respectively. Observations were carried out in the ABBA nodding mode along the slit to enable effective subtraction of the sky emission, especially in the NIR. In addition, a K-band blocking filter was employed to reduce thermal background contamination in the NIR. The data were reduced in STARE mode using calibration files from the night and the standard ESO Xshooter pipeline (P. Goldoni et al. 2006; A. Modigliani et al. 2010), which performs bias and dark correction, flat-fielding, wavelength calibration via arc lamps, and flux calibration based on standard star observations. Following the method described in J. Selsing et al. (2019), individual reduced exposures were directly co-added for the UVB and VIS arms, while A-B nod pairs were pair-subtracted prior to combination for the NIR arm. All reported wavelengths are given as observed in vacuum and corrected for the barycentric motion of the Earth.

The X-shooter observations of GRB 240122A began on 2024 January 23 at 02:25:01 UT ($T_0+15.95\,\mathrm{h}$) under excellent seeing conditions of 0.49 arcsec (A. Saccardi et al. 2024). GRB 240225B was observed on 2024 February 29, starting at 01:45:36 UT ($T_0+3.23\,\mathrm{d}$), with a seeing of 0.66 arcsec (B. Schneider et al. 2024). We observed GRB 240619A on 2024 July 2 starting at 23:20:52 UT ($T_0+13.82\,\mathrm{d}$); our observations targeted the catalogued galaxy PSO J162.3946+17.2828 in spatial coincidence with the optical afterglow and were obtained with a seeing of 0.94 arcsec (L. Cotter et al. 2024). Spectroscopic observations of GRB 240916A were conducted on 2024 September 16, beginning at 00:08:31 UT ($T_0+22.76\,\mathrm{h}$), under a seeing of 1.07 arcsec (D. Pieterse et al. 2024). Finally, X-shooter observations of GRB 241228B were carried out on 2024 December 29, starting at 06:00:45 UT ($T_0+1.07\,\mathrm{d}$), with a seeing of 0.54 arcsec (J. An et al. 2024).

In all, for GRBs 240122A, 240225B, 240619A, 240916A, 241228B observed with VLT/X-shooter, the start times of the observations spanned across the sample from $T_0 + 15.95$ h to $T_0 + 13.82$ d,

 $^{^{13}} https://www.sdss4.org/dr12/algorithms/sdssUBVRITransform/\#Lupton$

seeing ranged from 0.49 to 1.07 arcsec, and each target was obtained in four exposures per arm with per-exposure times of either 600 or 1200 s; for GRB 240619A the slit also encompassed a nearby second galaxy. The full spectroscopic observing log, along with observing conditions, is listed in Table 3. The final column lists the precise redshifts estimated for these GRBs, derived from the analysis of their afterglow spectra. These values were determined through the identification of absorption and/or emission features associated with the host galaxies. The full methodology, including line identification, fitting procedures, and associated uncertainties, is described in detail in Section 6.3.

4.3.2 GTC/OSIRIS

Spectroscopic observations of GRBs 240122A and 240910A were performed using the OSIRIS mounted on the 10.4 m GTC (J. Cepa 1998) at the Observatorio del Roque de los Muchachos (ORM), La Palma (see full spectroscopic log in Table 3). The observations were obtained as part of GTC programs GTCMULTIPLE2J-23B and GTCMULTIPLE4G-24B (PI: J. F. Agüí Fernández). For both targets, the R1000B grism was used in long-slit spectroscopy mode (LSS) with a slit width of 1.0 arcsec and binning of 2×2 pixels, providing a resolving power of $R \sim 600$ and a wavelength coverage of 3650-7800 Å.

The data were acquired in a sequence of three individual exposures, nodding along the slit to cancel the effect of possible artefacts or defects and provide a clean, final reduced product. The OSIRIS spectrum of GRB 240122A was began on 2024 January 22 at 22:56:23 ut ($T_0 + 12.47$ h), approximately 3.5 h prior to the VLT/X-shooter observations (C. C. Thoene et al. 2024), with 3 × 900 s exposures. The GTC/OSIRIS spectrum of GRB 240910A was started on 2024 September 12 at 03:08:33 ut ($T_0 + 47.13$ h), using 3 × 1200 s exposures, under good observing conditions (airmass ~ 1.14 and seeing of 0.8 arcsec; A. de Ugarte Postigo et al. 2024).

Data reduction was carried out using a combination of IRAF-based tasks and custom Python scripts developed for OSIRIS, which included bias subtraction, flat-fielding, wavelength calibration using arc lamps, and flux calibration using spectrophotometric standards. Accurate 1D spectra were extracted using optimal extraction techniques and corrected for instrumental response across the full wavelength range. Later on, Section 6.3 details the methodology, including line identification, fitting, and uncertainty estimation.

4.4 Radio

We observed radio afterglows of GRBs 240122A and 240910A utilizing the Australia Telescope Compact Array (ATCA) and the Karl G. Jansky Very Large Array (VLA), respectively. Furthermore, of the GRBs in our sample, GRBs 240225B and 241002B had no radio observations. GRB 240619A was detected in the radio at 15.5 GHz at $\sim\!\!3.4$ d post-burst using the Arcminute Microkelvin Imager Large Array (AMI-LA; L. Rhodes et al. 2024). GRB 240916A was observed with the VLA at central frequencies of 6, 10, and 15 GHz, yielding surface peak brightnesses of 35, 44, and 135 $\mu\rm{Jy}$ beam $^{-1}$, respectively (S. Giarratana et al. 2024b). The observation details are tabulated in Table A2.

4.4.1 ATCA

Following its optical localization, GRB 240122A was observed with the ATCA under the PanRadio GRB programme C3542 (PI: Ander-

son) on 2024 January 24, 26, 28, and February 12. This program aims to perform high-cadence multifrequency radio monitoring of a large sample of LGRBs in the southern hemisphere (Declinations < -10deg) between minutes to years after the burst to explore the evolution and properties of their afterglows (Leung et al., in preparation; Anderson et al., in preparation). GRB 240122A was observed with a wide range of frequencies centred on 5.5, 9.0, 16.7, and 21.2 GHz, each with a 2048 MHz-wide band. We reduced the visibility data using standard routines in MIRIAD (R. J. Sault, P. J. Teuben & M. C. H. Wright 1995). We used a combination of manual and automatic RFI flagging before calibration, conducted with MIRIAD tasks uvflag and pgflag, respectively. We used PKS 1934-63 to determine the bandpass response and to calibrate the flux density scale for all frequency bands. We used PKS 0607-157 to calibrate the time-variable complex gains for all epochs and frequency bands. After calibration, we inverted the visibilities using a robust weighting of 0.5 and then used the CLEAN algorithm (B. G. Clark 1980) to the target source field using standard MIRIAD tasks INVERT, CLEAN, and RESTOR to obtain the final images. For each observation, we measure the flux density of a detected source by fitting a point-source model to the restored image using the MIRIAD task IMFIT and report a non-detection using the rms sensitivity obtained from the residual image. The 1σ errors reported are purely statistical, as the systematic errors are expected to be much smaller (≤ 5 per cent; e.g. J. Reynolds 1994; S. J. Tingay et al. 2003). We detected the radio counterpart at 9 GHz on both 2024 January 24 and 28 at a position consistent with the GOTO optical counterpart (A. Kumar et al. 2024b). For all other frequencies, we estimated 3σ upper limits (see Table A2).

4.4.2 VLA

We observed GRB 240910A with the VLA 3.1 (2024 September 13; S. Giarratana et al. 2024a), 9.1 (2024 September 19), 21.3 (2024 October 1), and 46.2 (2024 October 26) d post-burst (Project code: SF171028) at the central frequencies of 6 (C band), 10 (X band), and 15 GHz (Ku band), with a bandwidth of 4, 4, and 6 GHz, respectively. The VLA source J0125-0005 was used as a phase calibrator. The distance between the target and the phase calibrator was about 2.7°. Each observation included scans on the flux and bandpass calibrator 3C48. The data were calibrated using the custom CASA pipeline (Version 6.5.4; J. P. McMullin et al. 2007) and visually inspected for possible radio frequency interference. The final images were produced with the tclean task in CASA (Version 6.5.4) using a Briggs weighting scheme (robust = 0.5). Results from the campaign are reported in Table A2. The GRB is detected at all frequencies during the first two epochs, and at 6 GHz it is also detected in the third epoch. The maximum flux densities, measured in the first epoch, are 137 ± 10 , 114 ± 9 , and 86 ± 10 µJy at 6, 10, and 15 GHz, respectively. For each detection, the flux density was measured by fitting a Gaussian to the cleaned image using the imview task in CASA. The final flux density error was estimated as the squared sum of the root mean square (RMS) and a typical 5 per cent accuracy for the amplitude scale calibration. Upper limits are reported with a 5σ confidence level.

5 PROMPT EMISSION ANALYSIS AND PROPERTIES

The prompt gamma-ray emission encodes the immediate output of the central engine and provides key diagnostics of the physical conditions in the relativistic outflow. For the seven GRBs in our

Table 4. Results from fitting the prompt emission spectra of *MAXI/GSC* and *Fermi/GBM* detected GRBs. The models used are those preferred based on the Akaike Information Criterion (AIC, H. Akaike 1974). In order to maximize the number of measured peak energies, the cutoff power-law (CPL) and Band (D. Band et al. 1993) models were chosen when AIC was agnostic between them and the PL model. Hardness ratios (HR) are calculated using the 50–300 and 10–50 keV bands. HR values for *MAXI/GSC* bursts are from extrapolating the 2–20 keV fits to these energies.

GRB (MAXI/GSC)	z	<i>T</i> ₉₀ (s)	Model	Fluence (2–20 keV) $(10^{-7} \text{ erg cm}^{-2})$	α	β	E _p (keV)	PG-Statistic	DoF	HR
240122A	3.163	≈ 36	PL	$1.26^{+0.47}_{-0.94}$	1.9 ± 0.4	-	-	_	-	$1.32^{+1.30}_{-0.65}$
240225B	0.946	≈ 21	PL	$10.7^{+0.63}_{-1.26}$	1.9 ± 0.1	_	_	_	_	$1.32^{+0.25}_{-0.21}$
GRB	z	T_{90}	Model	Fluence (10–1000 keV)	α	β	$E_{ m p}$	PG-Statistic	DoF	HR
(Fermi/GBM)		(s)		$(10^{-5}\mathrm{erg}\mathrm{cm}^{-2})$			(keV)			
240619A	0.396	36.13 ± 0.59	Band	$1.29^{+0.05}_{-0.08}$	$1.36^{+0.14}_{-0.17}$	$1.65^{+0.09}_{-0.04}$	$149.5^{+423.7}_{-143.5}$	241.14	436	$2.28^{+0.06}_{-0.07}$
240910A	1.460	272.39 ± 2.61	Band	$2.16^{+0.18}_{-0.24}$	$1.25^{+0.08}_{-0.05}$	$2.81^{+2.83}_{-0.44}$	$113.3^{+27.5}_{-22.7}$	271.38	324	$1.81^{+0.06}_{-0.07}$
240916A	2.610	32.00 ± 0.81	Band	$2.51^{+0.11}_{-0.15}$	$1.11^{+0.04}_{-0.06}$	$2.16^{+0.32}_{-0.14}$	$665.6^{+231.0}_{-186.1}$	231.02	325	$4.26^{+0.08}_{-0.11}$
241002B	-	64.26 ± 4.38	PL	$0.43^{+0.06}_{-0.07}$	$1.97^{+0.06}_{-0.08}$	-	-	219.85	326	$1.18^{+0.09}_{-0.11}$
241228B	2.674	19.46 ± 0.36	CPL	$4.19^{+0.10}_{-0.13}$	$0.81^{+0.03}_{-0.02}$	-	$350.6^{+17.9}_{-22.9}$	310.74	325	$5.72^{+0.06}_{-0.07}$

sample, we analysed MAXI/GSC and Fermi/GBM data to measure basic spectral and temporal properties, including the photon indices, peak energies $(E_{\rm p})$, isotropic-equivalent gamma-ray energies $(E_{\rm iso})$, and T_{90} ; analyses using other high-energy instruments discussed in Section 3.1 are beyond the scope of this work. These quantities are critical for placing the bursts in the broader GRB population, identifying any outliers, and examining potential links between the prompt emission and the optical afterglows recovered by GOTO. In particular, we aim to investigate whether the unusually hard spectra and high $E_{\rm p}$ values observed in several cases are connected to the optical detectability of these poorly localized events.

5.1 Prompt emission analysis

Here, we describe the methods used to extract and analyse the prompt emission properties for each GRB, using data from the relevant high-energy instruments. The analysis is divided into two parts: *MAXI/GSC* events and the *Fermi/GBM* events.

5.1.1 GRBs 240122A and 240225B with MAXI/GSC

We analysed the prompt emission of GRBs 240122A and 240225B with archival data of *MAXI*/GSC using High Energy Astrophysics Software (HEASOFT¹⁴). X-ray events of *gsc_med* type are processed with MXPRODUCT. Because light curves and spectra produced by MXPRODUCT are not suitable for short and variable transients like GRBs, we performed an additional step to extract light curves with a 1-s time resolution and applied effective area correction. Note that the process is identical to the process used for the *MAXI* GRB catalogue.

Fig. A8 shows the GSC light curves of GRBs 240122A and 240225B in the 2–20, 2–4, 4–10, and 10–20 keV energy bands. We estimated the T_{90} duration in the 2–20 keV band to be \approx 36 s and \approx 21 s for GRBs 240122A and 240225B, respectively. For GRB 240225B, the duration was calculated using data from a single *MAXI*/GSC scan. This value differs from those obtained by other instruments because the scan began at 20:15:30 UT, about 200 s later than the trigger times reported by the others.

Then, we extracted a spectrum of the T_{90} interval and corrected for variations in the effective area. The spectra of GRBs 240122A and 240225B are fit with a single power-law model, and the photon indices are found to be 1.9 ± 0.4 and 1.9 ± 0.1 (1σ error),

respectively. The energy flux in 2–20 keV was $3.5^{+1.3}_{-2.6} \times 10^{-9}$ and $5.1^{+0.3}_{-0.6} \times 10^{-8}$ erg cm⁻² s⁻¹. Fig. A9 shows the spectrum with the best-fitting model. The results of each fit are shown in Table 4.

5.1.2 GRBs 240619A, 240910A, 240916A, 241002B, and 241228B with Fermi/GBM

We analysed the prompt emission of GRBs 240619A, 240910A, 240916A, 241002B, and 241228B using the Fermi/GBM data available from the High Energy Astrophysics Science Archive Research Center (HEASARC¹⁵) archive (D. Gruber et al. 2014; A. von Kienlin et al. 2014; P. N. Bhat et al. 2016; A. von Kienlin et al. 2020). Using the HEASOFT and the Fermi Gamma-ray Data Tools (A. Goldstein, W. H. Cleveland & D. Kocevski 2023), we took the time-tagged event (TTE) data in the T_{90} interval for each burst to use as the source. We used the data from the brightest NaI detectors and the corresponding BGO detectors. These were NaI 0, NaI 1, NaI 2, and BGO 0 for GRB 240619A; NaI 8, NaI 11, and BGO 1 for GRB 240910A; NaI 3, NaI 4, and BGO 0 for GRB 240916A; NaI 10, NaI 11, and BGO 1 for GRB 241002B; and NaI 6, NaI 7, and BGO 1 for GRB 241228B. The background was modelled in the standard way, using a polynomial function fit to the CSPEC data for each burst. Polynomial order increased until the reduced fit statistic was < 1.15, resulting in the models fitting each GRB suitably well. Once the background model was obtained, we interpolated it across the source interval and exported this as the background to be used for spectral analysis. Additionally, we extracted the necessary response files.

We performed our analysis of the spectra using PyXspec (C. Gordon & K. Arnaud 2021) using three models of varying complexity: a simple power-law (PL), which measures a photon index, α ; a power law with a high-energy exponential cutoff (CPL), which measures α and the spectral peak energy, E_p ; and the Band model (D. Band et al. 1993), which measures two photon indices α and β , smoothly connected at a characteristic break energy, E_c . This break energy is converted to a peak energy using $E_p = E_c(2 - \alpha)$. We used the PG-Statistic in our analysis, which is appropriate for Poisson data with a Gaussian background. The results of each fit are shown in Table 4. Figs A10 and A11 present the Fermi/GBM observations of GRBs

¹⁴https://heasarc.gsfc.nasa.gov/docs/software/heasoft/

¹⁵https://heasarc.gsfc.nasa.gov

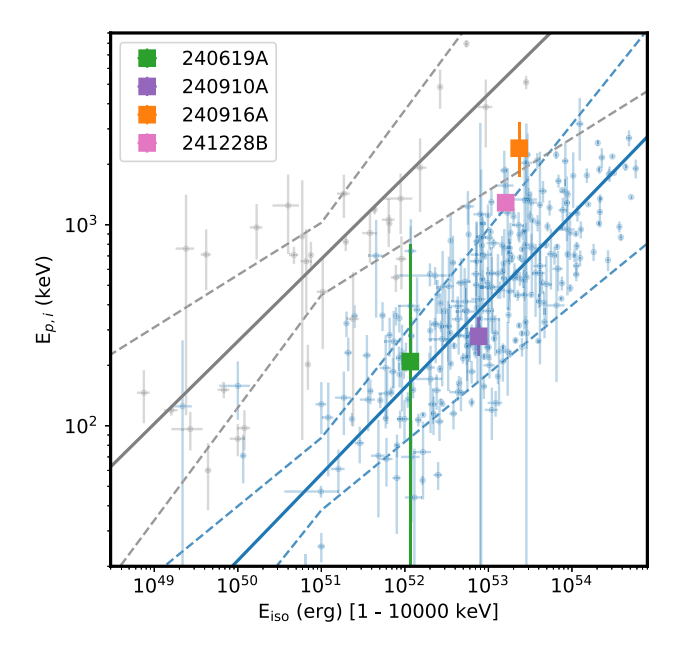


Figure 7. Fermi GRBs in our sample plotted in the Amati plane (L. Amati et al. 2002; L. Amati 2006), showing the relationship between the intrinsic (redshift corrected) peak energy ($E_{p,i}$) and the isotropic-equivalent gammaray energy release (E_{iso}). Lines show the best-fitting correlation (solid) and their 3σ bounds (dashed) for the long (blue) and short (grey) GRB populations. Correlation fits and comparison data are from P. Y. Minaev & A. S. Pozanenko (2020).

240619A, 240910A, 240916A, 241002B, and 241228B, showing the light curves and the corresponding fitted spectra, respectively.

5.2 Prompt emission properties

We plot the four of five Fermi bursts where it was possible to measure both $E_{\rm p}$ and $E_{\rm iso}$ (see Table 4) on the Amati plane (L. Amati et al. 2002; L. Amati 2006) in Fig. 7. GRBs 240916A and 241228B appear to show unusually high redshift-corrected peak energies ($E_{p,i}$) relative to their $E_{\rm iso}$ measurements, and are inconsistent with the Amati relation at the 3σ level. Both bursts lie at the high end of the $E_{\rm iso}$ distribution, indicating intrinsically powerful GRBs. In addition to this, the high energy photon index (β) measured for GRB 240619A is less than 2, indicating that the true peak of the spectrum is at an even higher energy. This may make 240619A an outlier of the Amati relation too. Only GRB 240910A appears to be typical in terms of its measured prompt properties.

We also plot all five *Fermi* and two *MAXI* GRBs on an HR – T_{90} diagram (cf. C. Kouveliotou et al. 1993), see Fig. 8. It is immediately apparent that the *Fermi* GRBs are unusually spectrally hard. Only GRB 241002B (best fit with a power-law model with a photon index of $\alpha = 1.97^{+0.08}_{-0.06}$) sits within the main 'cloud' of LGRBs. The others are either longer in T_{90} (GRB 240910A), or driven to high HR by their abnormally hard (for collapsar GRBs) photon indices (GRBs 240619A, 241228B) and/or high E_p (GRB 240916A). The *MAXI* GRBs also sit at the high end of the GBM HR distribution, but these values are obtained by extrapolating the 2–20 keV spectral fits to 300 keV, and so should be considered upper limits because we have no constraints on any breaks in the spectrum.

Given that the GRBs in our sample were selected based on the recovery of their optical afterglows by a relatively shallow telescope like GOTO, it is perhaps not surprising that they're outliers with

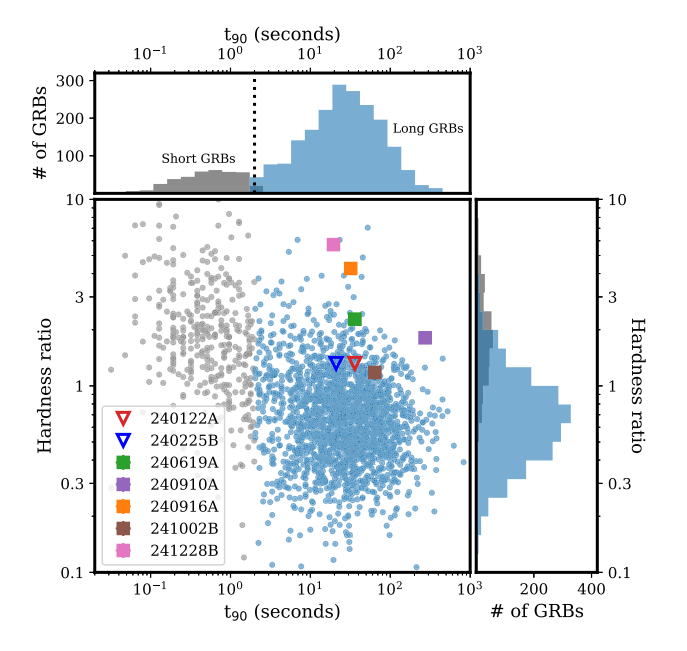


Figure 8. Hardness ratio versus T_{90} for the five *Fermi/GBM* bursts in our sample. The hardness ratio is the 50–300 keV fluence over the 10–50 keV fluence. Comparison data is taken from A. von Kienlin et al. (2020).

respect to the wider sample of GRBs. GRBs 240916A and 241228B both appear to be straightforward cases of intrinsically powerful GRBs, as evidenced by their higher than average $E_{\rm iso}$. However, their measured $E_{p,i}$ is high relative to the Amati relation even when accounting for the large $E_{\rm iso}$.

In contrast, GRB 240619A appears to be a much more energetically typical GRB, but at a low redshift (z=0.3960). The higher hardness ratio in this case may simply be the result of less redshifting than the majority of the detected population, resulting in a harder portion of the synchrotron spectrum falling in the 10–300 keV bandpass than usual. GRB 240910A also appears to be more typical energetically. In this case, a longer central engine duration ($T_{90}=272.39\pm2.61\,\mathrm{s}$) may be responsible for producing the bright afterglow.

All four of the above GRBs (240619A, 240910A, 240916A, and 241228B) have measured low-energy photon indices of $\alpha < 1.5$. This indicates that the low-energy synchrotron break was likely in the bandpass, causing α to be an unusually hard blend of two portions of the synchrotron spectrum (see e.g. M. E. Ravasio et al. 2018, 2019). The positions of these breaks are functions of the underlying physical parameters of the jet, and unusual parameter values may be responsible for the abnormally high hardness ratio. An alternative explanation is that the unusually hard prompt spectra in GRB 240916A and GRB 241228B may reflect jet—stellar-envelope interactions, supported by structured-jet and radiative-transfer simulations of LGRBs (D. Lazzati & M. C. Begelman 2005; D. Lazzati et al. 2013; C. Lundman, A. Pe'er & F. Ryde 2013) and even low-luminosity jets (M. A. Aloy, C. Cuesta-Martínez & M. Obergaulinger 2018).

5.3 T_{90} comparison

The T_{90} duration is a key parameter for classifying GRBs into long and short populations, with a conventional threshold at $T_{90} = 2 \,\mathrm{s}$. Fig. 9 shows the distribution of T_{90} values from the BAT GRB

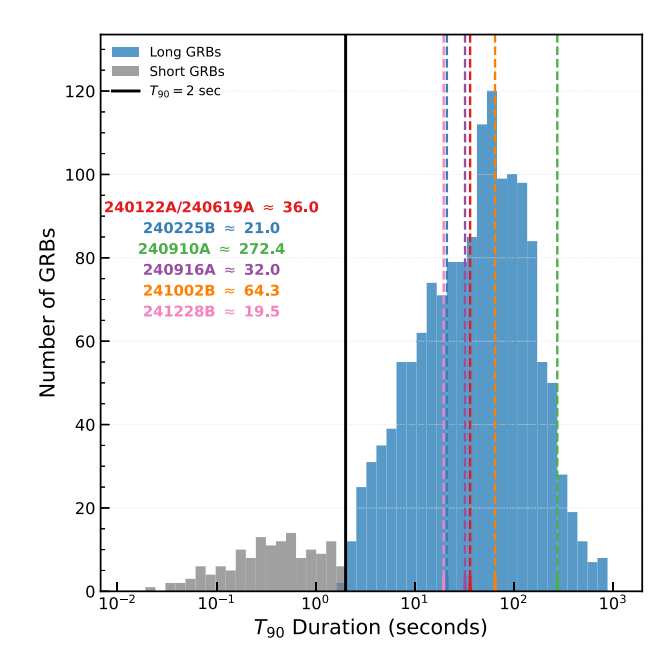


Figure 9. Distribution of T_{90} durations for a sample of GRBs from the BAT catalogue, divided into long (blue) and short (grey) populations. The dashed vertical lines mark the durations of GOTO GRBs, labelled with their respective names and T_{90} values. All GOTO GRBs fall in the long-duration class and cover a wide range of durations.

catalogue, ¹⁶ plotted on a logarithmic scale and separated into long (blue) and short (grey) classes. The histogram illustrates the well-known bimodality in the GRB population, with the majority of events falling in the long-duration category.

Overlaid on this distribution are the durations of the seven GOTO-detected GRBs in our sample, marked with vertical dashed lines and annotated with their names and T_{90} values. All seven events lie securely within the long-duration class, with durations ranging from ~ 20 to ~ 272 s. GRB 241228B (19.5 s) and GRB 240225B (21 s) sit at the lower end of the LGRB population, while GRBs 240122A, 240619A, 240916A, and 241002B (32 - 64 s) are closer to the peak of the LGRB distribution. GRB 240910A (272 s) lies toward the higher end, placing it among the longest events in the Swift sample.

6 AFTERGLOW ANALYSIS AND PROPERTIES

In this section, we analyse the afterglow properties of the GOTO-discovered GRBs across X-ray, UV and optical (photometric and spectroscopic), and radio wavelengths. We characterize their temporal and spectral behaviour, and place the results in the context of the broader GRB afterglow population.

6.1 X-ray

Each Swift/XRT-detected source confirmed its association with the GOTO optical GRB counterpart on the basis of spatial coincidence and, in most cases, temporal fading. For time-domain analysis, we utilized the automated Swift/XRT light curve fits from the UKSSDC pipeline (P. A. Evans et al. 2007, 2009). The X-ray light curves were adequately described by single power-law decays (see Fig. 10 for the

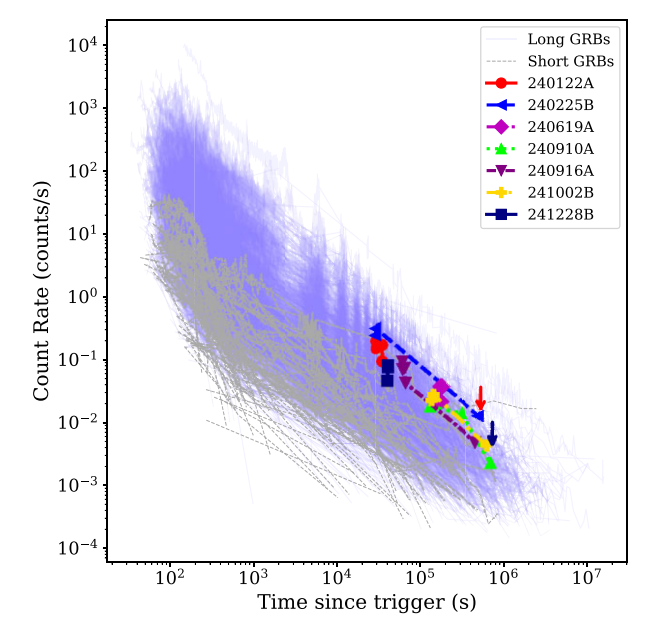


Figure 10. *Swift/XRT* 0.3–10 keV light curves. Archival LGRBs (grey) and SGRBs (blue dashed) are plotted as background. The seven GOTO GRBs are shown with distinct colours and styles.

light curves in counts per second).

Spectra for both source and background regions, along with corresponding ancillary and response files extracted in PC mode from the Swift/XRT repository, were grouped to a minimum of one count per bin using grppha task. Spectral fitting was performed in XSPEC using Cash statistics (W. Cash 1979), appropriate for lowcount Poisson-distributed data. Each spectrum was modelled with a simple absorbed power law, tbabs*ztbabs(zpowerlw) (J. Wilms, A. Allen & R. McCray 2000), accounting for both Galactic foreground and intrinsic absorption in the host galaxy. Galactic column density (NH,g) for each GRB was fixed at a value obtained from Swift Galactic $N_{\rm H}$ tool¹⁷ (R. Willingale et al. 2013), while the intrinsic host galactic absorption $(N_{\rm H,intr})$ and photon index (Γ) were left free to vary. All fits were performed in the 0.3-10.0 keV energy range, and the errors reported here correspond to 90 per cent confidence intervals. Fig. A12 presents the 0.3-10.0 keV XRT count rate spectra for all seven GRBs in our sample, overlaid (red solid line) with their respective best-fitting absorbed power-law models.

Table 5 summarizes the temporal and spectral properties derived from Swift/XRT observations of our GRB sample. Redshifts used for spectral fitting are reported in later sections. Photon indices lie in the range $\Gamma \simeq 1.4-2.9$, consistent with typical afterglow spectra. The intrinsic absorption shows substantial variation: GRBs 240122A and 240910A are consistent with negligible additional absorption beyond the Galactic foreground, whereas others, most notably GRB 240916A, require higher column densities of the order of 10^{22} cm⁻². The inferred unabsorbed 0.3-10 keV fluxes span nearly two orders of magnitude, from $\sim 7 \times 10^{-13}$ to $\sim 1.3 \times 10^{-11}$ erg cm⁻² s⁻¹, with the highest values observed for GRBs 240225B and 240122A, despite their relatively short spectral extraction intervals. Temporal decay slopes cluster around $\alpha_X \approx 1.0-1.3$ for most afterglows, though three cases (GRBs 240619A,

¹⁶https://swift.gsfc.nasa.gov/results/batgrbcat/index_tables.html

¹⁷https://www.swift.ac.uk/analysis/nhtot/

Table 5. Summary of *Swift/XRT* afterglow spectral and temporal properties for our GRB sample. Exp. denotes the spectral extraction time interval. $N_{\rm H,Gal}$ is fixed to the Galactic line-of-sight value, while $N_{\rm H,int}$ is the intrinsic absorption component derived from spectral fitting. Fluxes are unabsorbed values in the 0.3–10.0 keV band. α_X is the X-ray temporal index, where negative values indicate apparent rising trends likely caused by low-count statistics.

GRB	$T - T_0$ (10^3 s)	α_X	Γ	$N_{\rm H,g}$ $(10^{22} {\rm cm}^{-2})$	$N_{\rm H,intr}$ $(10^{22} {\rm cm}^{-2})$	Flux _{0.3-10 keV} $(10^{-12} \text{ erg cm}^{-2} \text{ s}^{-1})$	Exp. (s)	Z
240122A	29.5	$2.50^{+0.70}_{-2.10}$	$1.88^{+0.31}_{-0.24}$	0.105	~0.0	$6.54^{+1.41}_{-1.16}$	926.5	3.163
240225B	461.7	$1.09^{+0.16}_{-0.13}$	$2.19_{-0.59}^{+0.72}$	0.040	$0.29^{+0.49}_{-0.29}$	$12.6^{+6.5}_{-3.2}$	289.7	0.946
240619A	174.0	$-0.94^{+3.69}_{-0.05}$	$1.61^{+0.45}_{-0.71}$	0.028	$0.038^{+0.034}_{-0.038}$	$1.23^{+0.54}_{-0.36}$	1978.0	0.396
240910A	128.3	$1.10^{+0.40}_{-0.30}$	$1.75^{+2.22}_{-0.61}$	0.027	$0.006^{+0.005}_{-0.006}$	$0.69^{+0.49}_{-0.27}$	1983.0	1.460
240916A	61.0	$1.29^{+0.34}_{-0.23}$	$2.90^{+0.80}_{-0.60}$	0.140	$2.17^{+2.63}_{-1.92}$	$4.34^{+3.92}_{-1.52}$	1643.0	2.610
241002B	134.5	$1.10^{+0.40}_{-0.30}$	$1.82^{+1.06}_{-0.70}$	0.030	$0.096^{+0.251}_{-0.096}$	$1.34^{+0.68}_{-0.37}$	2702.0	_
241228B	40.0	$-1.28^{+4.49}_{-0.03}$	$1.44^{+0.46}_{-0.32}$	0.003	< 2.37	$2.81^{+1.65}_{-0.69}$	1809.0	2.674

240910A, and 241228B) show formally flat or rising indices; in each case, the uncertainties are large and the behaviour is consistent with constant flux within errors. At such late phases, exposure times were modest (typically 1–3 ks), naturally limiting the statistical precision of the spectral fits.

6.1.1 Swift/XRT light-curves comparison

To investigate the temporal behaviour of GRB afterglows and compare our GOTO-discovered GRBs against known populations, we compiled a comprehensive sample of *Swift/XRT* light curves, combining both archival GRBs and the GOTO sample (Fig. 10). Light curves were obtained from the UK Swift Science Data Centre (UKSSDC)¹⁸ bulk access portal, using a custom notebook provided by the UKSSDC team to automate downloads. In our visualization, archival LGRBs are shown in blue solid lines, SGRBs in grey dashed lines, and the seven GOTO-discovered GRBs (240122A, 240225B, 240619A, 240910A, 240916A, 241002B, 241228B) are overplotted with distinct markers and colours.

As seen in Fig. 10, the GOTO GRBs lie well within the canonical LGRB distribution, with count rates and temporal slopes consistent with typical long-burst afterglows. Their X-ray light curves track the faint to intermediate range of the LGRB population, showing no evidence for extreme behaviour. GRBs 240225B, 240910A, 240916A, and 241002B in particular seems to follow smooth declines, while others (e.g. GRB 241228B) are represented only by a few points, underscoring the sparse nature of the coverage. This sparseness arises not from the afterglows themselves but from the fact that these bursts were not initially triggered by *Swift*/BAT or XRT, but instead by wide-field, poorly localized instruments such as *Fermi*/GBM and *MAXI*/GSC.

6.2 UV/Optical/NIR

UV/Optical/NIR afterglow light curves for all seven GRBs 240122A, 240225B, 240619A, 240910A, 240916A, 241002B, and 241228B in our sample are shown in Fig. 6 (see Table A1 for complete photometric observations), plotted in both flux density and apparent magnitude space. For visual clarity, magnitudes in different filters have been offset vertically where indicated in the legends. All magnitudes are reported in the AB system and have been corrected for Galactic extinction using the E(B-V) values listed in Table 1, based on the recalibrated dust maps of E. F. Schlafly & D. P. Finkbeiner (2011).

Among the GRBs in our sample, GRB 241228B shows the highest cadence multicolour coverage, with early bright detections in GOTO *L*-band and a well-sampled decline. GRBs 240122A and 240225B each have moderate multiband coverage, while events such as GRBs 241002B and 240916A have sparser data sets but still provide key temporal constraints. The sparse and uneven temporal coverage of the light curves prevents us from robustly constraining decay slopes, break times, or colour evolution. In most cases, only a few photometric points are available per GRB, which precludes detailed afterglow fitting. Nevertheless, these data sets enable comparison with the extended sample of GRB afterglow light curves discussed in the following subsection and provide the basis for the afterglow modelling presented in Section 7.

6.2.1 Optical light curves comparison – Kann plot

To compare the optical behaviour of the GOTO-detected GRBs in our sample with previously well-observed GRB afterglows, we plotted their light curves alongside a reference sample from M. G. Dainotti et al. 2024 (Fig. 11). Three GRBs (240122A, 240225B, 241228B) have well-sampled R-band data, while the remaining four (240619A, 240910A, 240916A, 241002B) are well-observed in the r/r' band (see Fig. 6). In each case, the same filter band from the reference sample is used to minimize colour offsets, and all magnitudes are corrected for Galactic extinction. The reference light curves span a wide range of brightness and decay behaviours, and are plotted in grey for comparison.

The left panel of Fig. 11 shows the R-band events (240122A, 240225B, 241228B) in blue, red, and lime, while the right panel shows the r/r'-band events (240619A, 240910A, 240916A, 241002B) in purple, magenta, maroon, and navy. The afterglow light curves comparison in R – and r/r' bands demonstrates that the afterglows of GOTO-detected GRBs lie within the overall distribution of known GRB afterglows in both brightness and decay behaviour. The R-band events are consistent with the median properties of the sample, whereas the r/r'-band events span a broader range in brightness and decline rates.

To place our events quantitatively within the broader population, we interpolated the extinction-corrected light curves at fixed epochs, using only those with data coverage near the corresponding epochs of our GRBs. In R band at t=0.79 d (close to the first data point for GRB 240225B), the comparison sample spans 14.14–23.93 mag (median 20.45 mag). Our GRBs fall within this range: GRB 240225B is relatively bright (18.79 mag), while GRBs 241228B and 240122A are near the population median (20.49 and 20.98 mag, respectively). In r/r' band at t=1.64 d (a phase where both

¹⁸https://www.swift.ac.uk/xrt_products/bulk.php

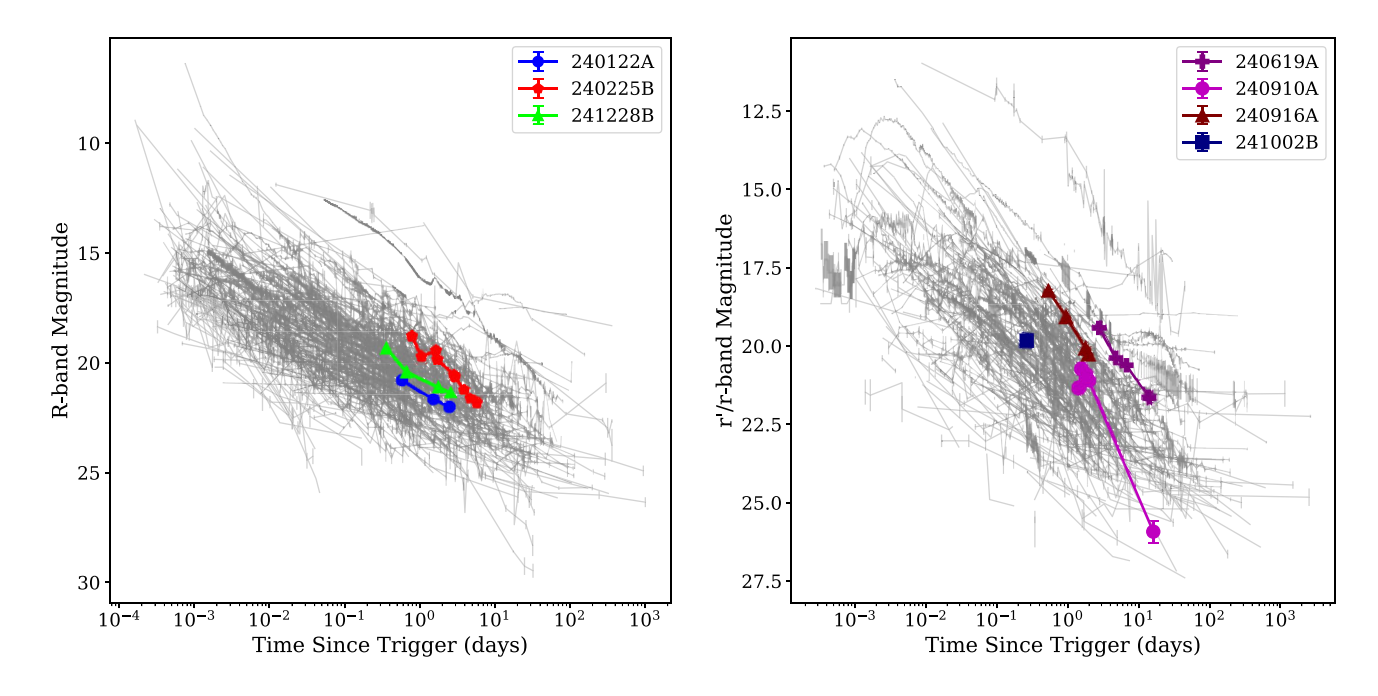


Figure 11. *R*- and *r/r'*-band afterglow light curves for the seven GRBs in our sample compared against archival GRB afterglows compiled by M. G. Dainotti et al. (2024), known as the 'Kann plot'.

GRBs 240910A and 240916A have measurements), the sample spans 14.20–25.50 mag (median 21.13 mag). GRB 240916A is somewhat brighter than average (19.90 mag), while GRB 240910A lies close to the median (20.80 mag) but shows an unusually steep decline, fading by $\Delta m \approx 4.7$ mag over $\Delta t \approx 14.7$ d ($\sim\!0.32$ mag d $^{-1}$). By contrast, GRB 241002B appears relatively faint even at early times. Overall, these comparisons confirm that the GOTO afterglows occupy the central brightness distribution of known GRB afterglows while also sampling the diversity of decline rates and brightness within the population.

6.3 Spectroscopic analysis-redshift estimation

When a GRB explodes, the resulting afterglow light passes through both the interstellar medium of its host galaxy and any intervening material along the line of sight, imprinting a series of absorption features onto the spectrum. In our X-shooter spectra, only the highest redshift absorption system is identified and assigned as the redshift of the GRB since no higher redshift intervening material is physically possible. While additional foreground absorption systems may be present, a detailed analysis and characterization of these intervening absorbers is beyond the scope of this paper and will be addressed in future work. The redshifts are estimated by identifying common absorption lines in GRB afterglows using the line lists of J. P. U. Fynbo et al. (2009) and L. Christensen et al. (2011), and/or emission lines from their host galaxies. The redshift and its associated uncertainty are then derived by fitting Voigt profiles J.-K. Krogager (2018) to the absorption features, prioritizing lowionization, unsaturated, and unblended transitions, and Gaussian profiles to the emission lines.

6.3.1 VLT/X-shooter

Here, we summarize the results from our VLT/X-shooter spectra of GRBs 240122A, 240225B, 240619A, 240916A, and 241228B:

GRB 240122A: The VLT/X-shooter of spectrum GRB 240122A exhibits a strong Ly α absorption feature near 5060 Å, accompanied by a set of metal lines, including Si II, Fe II, C II, Si IV, C IV, Al II, and Mg II. All features are consistent with a common redshift of $z = 3.1634 \pm 0.0003$. The spectrum is shown in Fig. A1, and a detailed list of the identified lines is provided in Table A3. We note the presence of multiple intervening absorbers at the following redshifts: z = 2.7583, 2.5384, 2.4879, 2.4230, 1.5111, and 1.4618.

GRB 240225B: In the case of GRB 240225B, a continuum is detected over the entire wavelength range (from 3300 to 20 400 Å) and the following strong absorption features are identified: Al III, Cr II, Fe II, Mn II, Mg II, Mg I, and Ca II at a common redshift of $z=0.9462\pm0.0002$. At the same redshift, three emission lines ([O II] $\lambda\lambda$ 3727, 3730 and [O III] λ 5008) are identified from the host galaxy. The complete list of identified lines is provided in Table A4. One intervening system is identified at z=0.7056.

GRB 240619A: For GRB 240619A, we identified several strong emission lines as due to [O II] $\lambda\lambda$ 3727, 3730, [Ne III] λ 3870, H γ , H β , [O III] $\lambda\lambda$ 4960, 5008, and H α at a common redshift of $z=0.3960\pm0.0001$. A second fainter object is visible in the Legacy Survey images, located about 1.7 arcsec west of the GRB afterglow position. This source was also covered by the X-shooter slit, and a redshift of z=1.34 was derived from the detection of the emission lines of [O II] doublet and H α . Due to its larger angular offset, we consider this galaxy to be unrelated to the GRB. The spectrum of the host galaxy and the identified lines are shown in Fig. A4 and Table A5.

GRB 240916A: The reduced spectrum of GRB 240916A reveals a prominent HI Ly α absorption feature at ~4400 Å, along with a rich set of metal absorption lines including Si II, Al III, and Fe II. In addition, we detect several fine-structure transitions such as Fe II* and Ni II*. From these features, we derive a redshift of $z=2.6100\pm0.0002$. The spectrum and line identifications are shown in Fig. A6 and listed in Table A7. Two intervening absorbers are identified at z=2.2904 and z=2.2140.

GRB 241228B: GRB 241228B spectrum displays a clear Ly α absorption line at ~4470 Å, along with numerous metal absorption features, including N v, S II, Si II, Fe II, and O I. Several fine-structure transitions such as Si II*, O I*, C II*, Fe II*, and Ni II* are also detected. In addition, a strong Ly α emission line is observed from the host galaxy. These features indicate a redshift of $z=2.6745\pm0.0004$. The spectrum and complete line identifications are presented in Fig. A7 and Tables A8 and A9. Absorption features corresponding to the intervening systems at z=2.4576, 2.0004, 1.8244, 0.9504 are also observed.

6.3.2 GTC/OSIRIS

Here, we summarize the results from our GTC spectra of GRBs 240122A and 240910A:

GRB 240122A: Despite poorer observing conditions (seeing of \sim 1.7 arcsec), the GTC/OSIRIS spectrum of GRB 240122A clearly reveals a strong Ly α absorption feature near 5060 Å, along with a consistent set of metal lines, including Si II, Fe II, C II, Si IV, C IV, Al II, and Mg II. These features confirm a redshift similar to that derived from the higher resolution VLT spectrum ($z=3.163\pm0.003$). The reduced OSIRIS spectrum is shown in Fig. A2, with identified features listed in Table A3.

GRB 240910A: In the case of GRB 240910A, the afterglow continuum is clearly detected across the full spectral range, and the spectrum reveals a rich set of absorption features. Prominent lines include Si II, C IV, Fe II, Al II, Al III, Cr II, Mn I, Mn II, Ni II*, Mg II, and Mg I, along with several fine-structure transitions such as Fe II* and Ni II*. All lines are consistent with a common redshift of $z = 1.4605 \pm 0.0007$. The reduced spectrum is presented in Fig. A5, and a complete list of identified lines is provided in Table A6.

In summary, our spectroscopic follow-up of seven GRBs using VLT/X-shooter and GTC/OSIRIS reveals a wide range of redshifts ($z \sim 0.40$ to $z \sim 3.16$), with absorption and emission features tracing both the GRB host environments and the intervening interstellar medium. High-quality afterglow spectra enable precise redshift measurements and identification of various ionic species, including fine-structure transitions. These results provide critical context for understanding the physical conditions in GRB host galaxies and lay the foundation for future studies of metallicity, dust content, and kinematics in GRB environments.

6.3.3 Redshift comparison

To show the redshift distribution of GRBs in our sample, we compare them against the broader GRB population presented in the comprehensive compilation by M. G. Dainotti et al. (2024). Fig. 12 shows a histogram of GRBs with measured redshifts from that sample, classified into long and short categories. The majority of GRBs in the M. G. Dainotti et al. (2024) sample are LGRBs, with a redshift distribution peaking around $z \sim 0.5 - 2$, consistent with the star formation history of the universe. SGRBs appear more frequently at lower redshifts, consistent with their likely origin from compact object mergers with longer delay times.

Overlaid on this distribution are the measured redshifts of the GOTO GRBs, shown as vertical dashed lines with annotations above the axis. Our sample spans from z=0.40 (GRB 240619A) to z=3.16 (GRB 240122A). It is worth noting that the optical selection imposed by GOTO inherently limits detections to $z \lesssim 5$, since at higher redshifts the Lyman forest progressively enters and

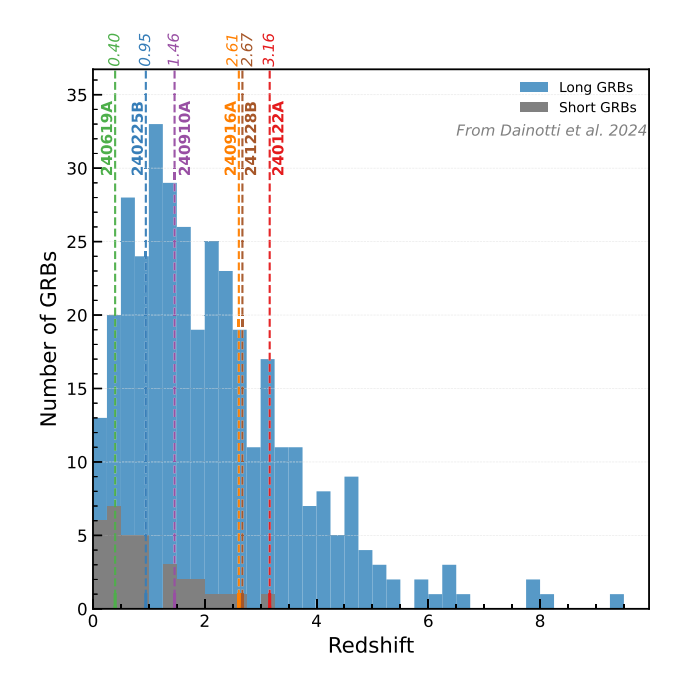


Figure 12. Histogram of redshift distribution for long (blue) and short (grey) GRBs from the sample of M. G. Dainotti et al. (2024). Overlaid are the redshifts of six GRBs with optical afterglows discovered by GOTO in 2024, marked with vertical dashed lines, labelled by GRB name within the plot, and redshift values above. This visual comparison highlights the diversity in redshift of GOTO-discovered GRBs and demonstrates their placement within the broader GRB population.

then highly absorbs flux across the GOTO L-band (400–700 nm). GRBs 240225B (z=0.95) and 240910A (z=1.46) fall near the central peak of the LGRB distribution, while GRB 240916A (z=2.61) and GRB 241228B (z=2.67) occupy the higher redshift tail together with GRB 240122A at z=3.16. This spread highlights that the GOTO sample encompasses both low- and high-redshift GRBs, demonstrating the survey's capability to probe the wide observed redshift range of the LGRB population.

From a physical perspective, the low-redshift events, such as GRB 240619A, are particularly valuable for detailed host-galaxy and supernova connection studies, where high signal-to-noise follow-up is achievable. Conversely, the higher redshift events (e.g. GRBs 240916A, 241228B, and 240122A) provide critical leverage for probing star-forming environments in the early universe and for constraining the role of GRBs as tracers of cosmic star formation beyond z > 2.

6.4 Radio

The radio light curves of GRBs 240122A, 240619A, 240910A, and 240916A are shown in Fig. 13, plotted in flux density (left) and luminosity (right). For context, we compare these with the historical population of GRBs compiled at 8–10 GHz. The GOTO GRBs lie within the locus of LGRBs, showing flux densities and luminosities consistent with this population. None displays the systematically fainter or more rapidly fading behaviour typical of SGRBs. Within the sample, GRB 240122A is among the brightest radio afterglows, while GRB 240910A and GRB 240916A fall at the lower end of the distribution, illustrating the intrinsic spread in LGRB radio emission. Despite this variation, their temporal evolution remains broadly consistent with expectations for LGRB afterglows, reinforcing the

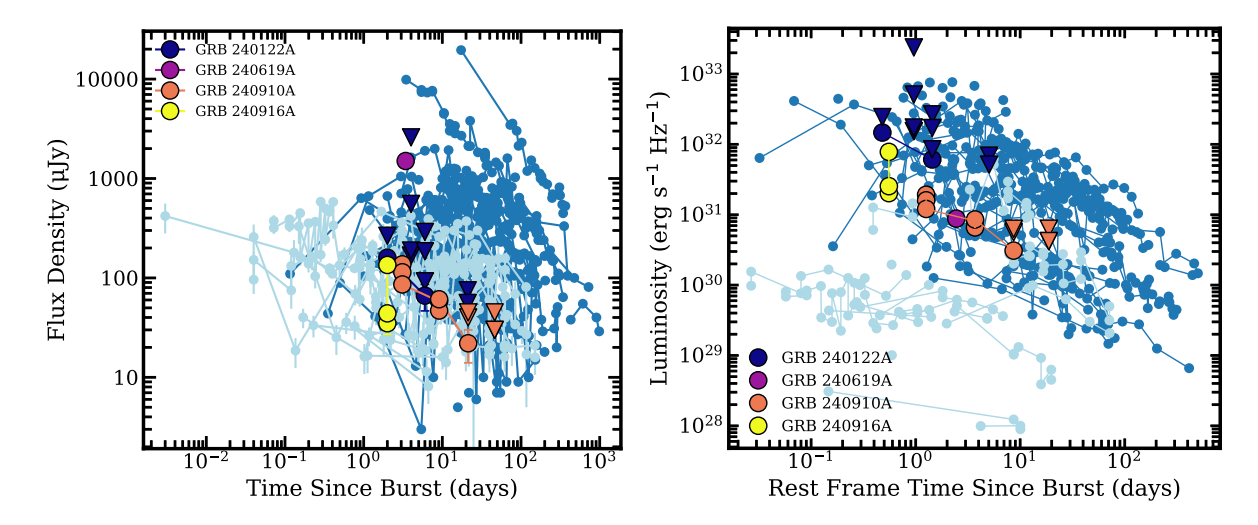


Figure 13. Left panel: 8–10 GHz radio afterglow light curves of GRBs, showing flux density (in μJy) as a function of observer-frame time since burst. The coloured markers represent four LGRBs discovered by GOTO with available radio follow-up observations: GRB 240122A (dark blue), GRB 240619A (magenta), GRB 240910A (orange), and GRB 240916A (yellow), from a sample of seven GOTO GRBs. For comparison, literature LGRB afterglows are shown in dark blue, and SGRBs in grey. Right panel: rest-frame radio luminosity light curves of the same GRBs, showing monochromatic luminosity (in erg s⁻¹ Hz⁻¹) as a function of rest-frame time since explosion. The GOTO events are consistent with the broader LGRB population in terms of both luminosity and temporal evolution, highlighting the capability of GOTO to detect GRBs with typical radio afterglow properties. References: G. B. Taylor et al. (1998), D. A. Frail et al. (1999, 2000, 2005, 2006), F. A. Harrison et al. (1999), E. Berger et al. (2000, 2001a, 2005), T. J. Galama et al. (2000, 2003), E. Berger, S. R. Kulkarni & D. A. Frail (2001b), S. G. Djorgovski et al. (2001), F. A. Harrison et al. (2001), P. A. Price et al. (2002), A. M. Soderberg, D. A. Frail & M. H. Wieringa (2004b), A. M. Soderberg et al. (2004a, 2006), S. B. Cenko et al. (2006), E. Rol et al. (2007), P. Chandra et al. (2008), D. A. Perley et al. (2008), A. J. van der Horst et al. (2008), P. Chandra et al. (2010), S. B. Cenko et al. (2011, 2012), P. J. Hancock et al. (2012), J. Greiner et al. (2013), A. Moin et al. (2013), D. A. Perley et al. (2014), W. Fong et al. (2014), A. Horesh et al. (2015), T. Laskar et al. (2016, 2018, 2022, 2023), G. P. Lamb et al. (2019), W. Fong et al. (2021), B. O'Connor et al. (2023), G. E. Anderson et al. (2024, 2025), L. Rhodes et al. (2024), G. Schroeder et al. (2024), A. J. Levan et al. (2024).

conclusion that the radio properties of the GOTO events trace the same underlying population.

7 AFTERGLOW MODELLING

For the afterglow light-curve modelling, we used the afterglowpy module (version 0.8.0; G. Ryan et al. 2020). This Python-based tool utilizes the single-shell approximation (H. van Eerten et al. 2010; H. van Eerten 2018) to model GRB afterglow light curves by accounting for the effects of complex jet structures and an off-axis observer position. We modelled multiband light curves for each of the GOTO-discovered GRBs presented in this paper. For our modelling, we assumed the simplest TopHat profile of the jet structure and fixed some parameters where required (see Table 6).

All afterglow analyses were conducted using dynesty nested sampling within the Bilby framework (version 2.4.0; G. Ashton et al. 2019). The data set mostly consisted of relatively sparse data in optical bands, complemented by X-ray data from Swift/XRT. To ensure robustness and minimize bias, our priors were set to be broad, and the prior probabilities for most parameters were modelled using uniform distributions (see Table 6). We used a Gaussian likelihood and the dynesty nested sampler with 1500 live points and a stopping tolerance of $\Delta \log \mathcal{Z} = 0.1$.

When modelling GRBs with sparsely sampled afterglow data, we adopt a flexible strategy in which a subset of parameters is fixed to literature-informed medians that are representative of LGRBs drawn from previous population studies (M. D. Aksulu et al. 2022; A. A. Chrimes et al. 2022) to assess consistency with the typical long-GRB population. These works analysed large samples of LGRBs and reported values for key microphysical parameters: ϵ_e (M. D. Aksulu et al. 2022), and ϵ_B , n_0 , and p (A. A. Chrimes et al. 2022).

A value for $\log_{10} \epsilon_e$ is not reported in A. A. Chrimes et al. (2022), from which we take most other fixed parameters owing to its larger sample. We therefore adopt ϵ_e from M. D. Aksulu et al. (2022). We do not take all parameters from M. D. Aksulu et al. (2022) because its GRB sample is smaller; combining their ϵ_e with the broader A. A. Chrimes et al. (2022) set maximizes coverage. Our adopted value is slightly below the peak $\epsilon_e \sim 0.13-0.15$ inferred from radio peaks by P. Beniamini & A. J. van der Horst (2017), but it lies within the $\epsilon_e \sim 0.01-0.16$ range for a homogeneous medium reported by R. A. Duncan, A. J. van der Horst & P. Beniamini (2023), who used radio peaks together with constraints from the prompt gamma-ray emission efficiency.

For GRBs where full sampling over all parameters led to unconstrained, multimodal, or non-convergent posteriors, we fixed one or more of these quantities to their literature-based mean values. This approach allows stable and interpretable modelling when the data cannot independently constrain all parameters. Fixing select values based on well-motivated priors reduces degeneracies, avoids overfitting, and maintains physical plausibility in the resulting fits.

Results overview. We modelled six GOTO-discovered GRBs (excluding GRB 241002B; no redshift) with the TopHat (uniform) jet model in afterglowpy using dynesty nested sampling via Bilby. Posterior summaries (medians with 16-84 per cent credible intervals) are listed in Table 6; multiband light curves and posterior corner plots are shown in Figs 14 and 15, respectively. Unless stated otherwise, we adopt $\xi_N=1$ (fraction of electrons accelerated) as our baseline; for sparsely constrained events, we fix a subset of microphysical parameters $(p, n_0, \text{ and, where noted, } \epsilon_B$; see Table 6) to population-informed values to suppress degeneracies. With this setup, the events are well described by narrow, near-on-axis geometries; expected covariances

Table 6. Parameter estimation priors and marginalized posteriors for the GOTO-discovered GRBs using the afterglowpy TopHat model. Posteriors are medians with 16-84 per cent credible intervals.

	θ_v (rad)	$\log_{10}(E_0)$ (erg)	θ_c (rad)	$\log_{10}(n_0) \text{ (cm}^{-3})$	p	$\log_{10} \epsilon_e$	$\log_{10}\epsilon_B$	ξ_N	d_L (Mpc)
			GRB 240122	2A; GOTO24eu					
Priors	U(0.0; 0.5)	U(49; 57)	U(0.0; 0.5)	-0.379	2.119	-1.246	-4.290	1.0	27708.87
Posteriors	$2.15^{+0.09}_{-0.10} \times 10^{-2}$	$54.97^{+0.02}_{-0.02}$	$2.39^{+0.12}_{-0.12} \times 10^{-2}$	-0.379	2.119	-1.246	-4.290	1.0	27708.87
	0.10	0.02		5B; GOTO24tz					
Priors	U(0.0; 0.5)	U(49; 57)	U(0.0; 0.5)	U(-5.0; 3.0)	2.119	-1.246	-4.290	1.0	6342.55
Posteriors	$9.43^{+0.38}_{-0.41} \times 10^{-2}$	$54.27^{+0.04}_{-0.04}$	$7.23^{+0.31}_{-0.31} \times 10^{-2}$	$1.87^{+0.09}_{-0.11}$	2.119	-1.246	-4.290	1.0	6342.55
	-0.41	-0.04		A; GOTO24cvn					
Priors	U(0.0; 0.5)	U(49; 57)	U(0.0; 0.5)	-0.379	2.119	U(-5.0;	U(-5.0;	1.0	2217.13
						0.0)	0.0)		
Posteriors	$0.41^{+0.04}_{-0.07}$	$52.70^{+0.42}_{-0.35}$	$0.45^{+0.04}_{-0.07}$	-0.379	2.119			1.0	2217.13
	0.07	0.55	0.07			$-0.85^{+0.3}_{-0.3}$	$^{32}_{99}$ $-2.18^{+0.12}_{-0.15}$	2	
			GRB 240910	A; GOTO24fvl		0.2	,, 0.1.		
Priors	U(0.0; 0.5)	U(49; 57)	U(0.0; 0.5)	-0.379	2.119	-1.246	-4.290	0.180	10826.91
Posteriors	$4.25^{+0.07}_{-0.12} \times 10^{-2}$	$54.77^{+0.01}_{-0.01}$	$4.07^{+0.08}_{-0.12} \times 10^{-2}$	-0.379	2.119	-1.246	-4.290	1.0	10826.91
	0.12	0.01		A; GOTO24fzn					
Priors	U(0.0; 0.5)	U(49; 57)	U(0.0; 0.5)	-0.379	2.119	U(-5; 0)	U(-5; 0)	0.180	22000.43
Posteriors	$2.29^{+0.71}_{-0.78} \times 10^{-2}$	$54.40^{+1.03}_{-0.63}$	$4.73^{+1.16}_{-1.26} \times 10^{-2}$	-0.379	2.119			1.0	22000.43
	0.70	0.05	1.20			$-1.34^{+0.5}_{-0.6}$	$^{59}_{05}$ $-1.47^{+0.9}_{-0.7}$! !	
			GRB 241228	B; GOTO24jmz		0.7	0.7.	,	
Priors	U(0.0; 0.5)	U(49; 57)	U(0.0; 0.5)	-0.379	2.119	-1.246	-4.290	0.180	22653.17
Posteriors	$4.86^{+0.14}_{-0.11} \times 10^{-3}$	$55.429^{+0.004}_{-0.004}$	$10.56^{+0.05}_{-0.07} \times 10^{-3}$	-0.379	2.119	-1.246	-4.290	0.180	22653.17

Note. θ_v – viewing angle; E_0 – isotropic-equivalent kinetic energy; θ_c – half-opening angle of jet core; n_0 – density of the surrounding ISM; p – electron energy distribution power-law index; ϵ_e – fraction of energy that goes into electrons; ϵ_B – fraction of energy that goes into the magnetic field; ξ_N – fraction of shock-accelerated electrons; d_L – luminosity distance.

(e.g. $E_0 - \theta_c$) are present but posteriors are unimodal and not prior-bound.

For completeness, we provide short remarks on a subset of GRBs in our sample for which extra clarification is useful. These notes highlight only the key features or caveats, while the overall methodology and global results are presented above.

GRB 240122A: A three-parameter TopHat fit $(\theta_v, \theta_c, \log_{10} E_0)$ with microphysics fixed as explained above reproduces the broadband evolution (Table 6; Figs 14, 15). Radio points lie slightly *above* the model, while late-time X-ray points are slightly *below*; since synchrotron self-absorption would further suppress early-time radio, it cannot explain the positive radio residuals – more plausible are a reverse shock, mild energy injection, a density bump, or calibration offsets.

GRB 240910A: A three-parameter TopHat fit $(\theta_v, \theta_c, \log_{10} E_0)$ with the other microphysics held fixed reproduces the optical and X-ray light curves with a single parameter set (Table 6; Figs 14, 15). The model shows a modest, systematic overprediction in the radio bands. This behaviour is consistent with fixed microphysics - at fixed ϵ_e , adopting $\xi_N = 1$ raises $F_{\nu,\text{max}}$ and lowers ν_m , which naturally boosts the radio while leaving higher frequency bands close to the data. For completeness, we also explored fits in which additional microphysical parameters were allowed to vary, including ξ_N ; these trials slightly reduced the radio residuals but degraded the X-ray agreement and produced broader, strongly correlated posteriors. For uniformity across the sample, we therefore retain the three-parameter fit and interpret the residual radio offsets as secondary systematics related to normalization and propagation effects (e.g. synchrotron self-absorption; R. Sari et al. 1998; J. Granot & R. Sari 2002) and interstellar scintillation (J. Goodman 1997; D. A. Frail et al. 1997); possible host free-free absorption is also plausible (see e.g. K. W. Weiler et al. 2002).

GRB 240916A. A five-parameter TopHat (uniform) jet fit $(\theta_v, \theta_c, \log_{10} E_0, \log_{10} \epsilon_e, \log_{10} \epsilon_B)$ yields a clean broad-band match with

unimodal posteriors. The geometry is nearly on-axis with small angles. The microphysics favour a comparatively lower ϵ_e and a moderately higher ϵ_B within typical afterglow ranges. Magnetized internal-shock models for the *prompt* phase indicate that magnetization can alter radiative efficiency and shift the characteristic synchrotron/IC spectral peaks (e.g. P. Mimica & M. A. Aloy 2012). However, the ϵ_B inferred here is the *downstream* magnetic energy fraction of the *afterglow* forward shock and is not directly comparable to the prompt-phase shell magnetization; any putative link to $E_{p,i}$ is therefore model-dependent and not required by our data.

GRB 241002B: No secure redshift is available. We sampled z with a broad prior, but the redshift posterior remained unconstrained; redshift-dependent quantities (d_L , E_0 , and rest-frame times) track the priors, and the angles are only weakly informed. We therefore do not report parameter estimates and exclude this burst from population-level comparisons.

GRB 241228B. We model the afterglow with a three-parameter TopHat jet, sampling $(\theta_v, \theta_c, \log_{10} E_0)$ while holding the microphysics fixed $(p, n_0, \epsilon_e, \epsilon_B, \xi_N)$. This minimal configuration reproduces the optical and X-ray evolution at early-to-intermediate epochs (Table 6; Figs 14, 15). Small, band-dependent residuals appear around the X-ray band and the bluest optical filters, consistent with a cooling break lying close to the optical and/or modest host galaxy extinction; these offsets remain at a low level under reasonable microphysical choices. Because the microphysics are fixed, the fit can trade flux normalization against geometry, and the posterior favours an effectively on-axis view with a very narrow core. We therefore regard the recovered θ_c as a model-dependent lower bound – allowing, for example, ϵ_B to vary with a broad log-uniform prior would broaden the θ_c posterior and plausibly shift its median upward, at the cost of a higher E_0 .

At late times, the model systematically underpredicts the flux across bands, indicating additional physics not captured by a single forward-shock component. Plausible explanations include mild,

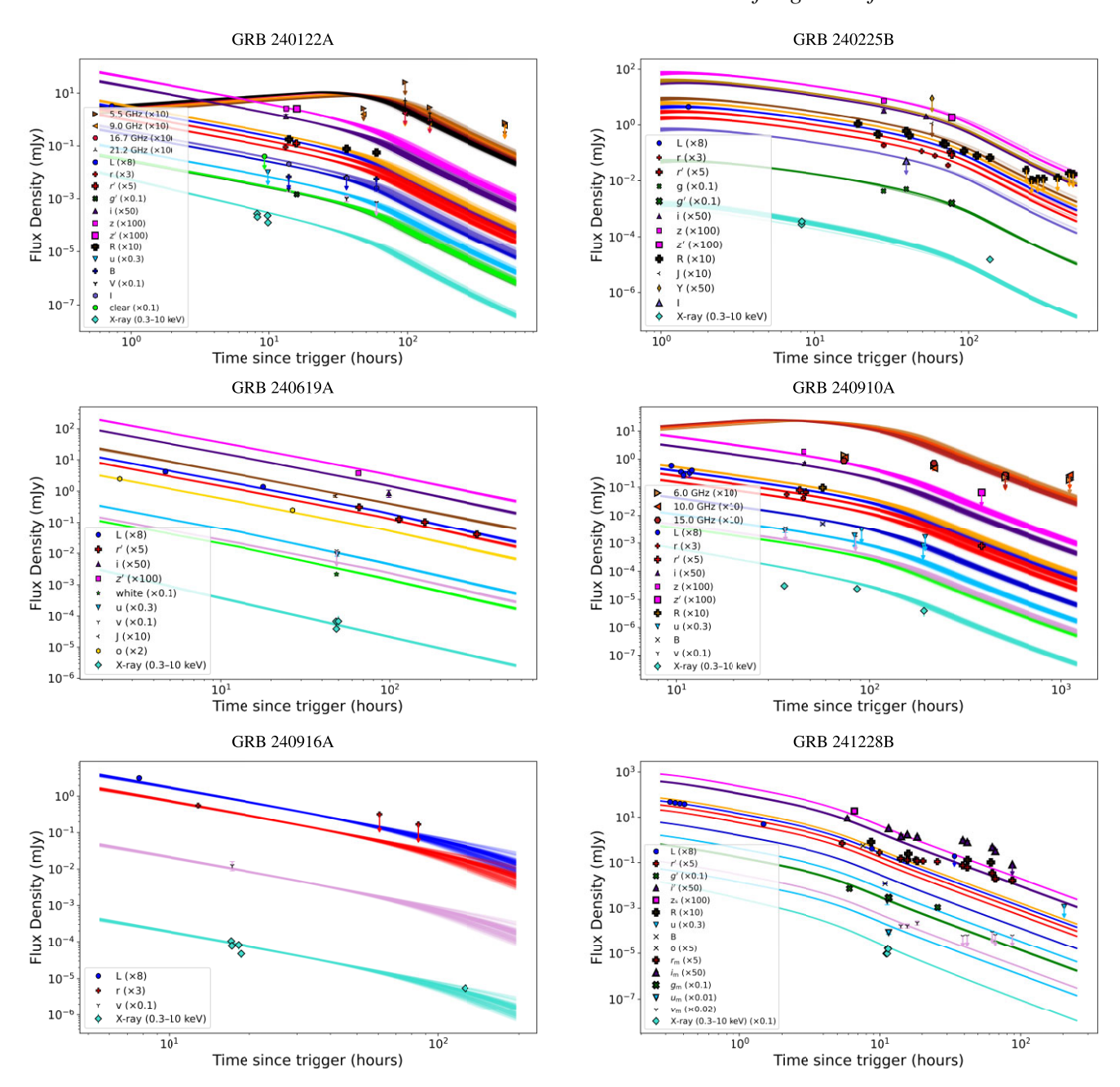


Figure 14. Multiwavelength afterglow light curves for six GRBs modelled in this work: GRBs 240122A, 240225B, 240619A, 240910A, 240916A, and 241228B. Each panel shows the observed data points (UV/optical/NIR, X-ray, and radio, where available), overlaid with the best-fitting afterglow model using a TopHat (uniform) jet scenario (see the text for details). Photometric data are compiled from our observations and published GCN Circulars. Fluxes are rescaled for clarity as indicated in the legends.

sustained energy injection (refreshed shocks), interaction with a local density enhancement, or an additional outflow component (e.g. a wider jet or cocoon). These effects can maintain the late-time emission above the single-jet prediction without disrupting the early-time agreement. Given the limited leverage to discriminate among scenarios, we retain the three-parameter TopHat fit for the main analysis and note the late-time excess as a likely secondary component.

Beaming factor and jet energetics. For each GRB in our sample (see Table 6) we compute the beaming factor and the beaming-corrected jet energy using the relations $f_b = 1 - \cos \theta_c$, $E_{\rm jet} = f_b E_0$.

```
Per-burst summary (medians with 16–84 per cent uncertainties): 240122A: f_b = (2.86^{+0.31}_{-0.28}) \times 10^{-4}, E_{\rm jet} = (2.66^{+0.20}_{-0.19}) \times 10^{51} erg. 240225B: f_b = (2.61^{+0.22}_{-0.22}) \times 10^{-3}, E_{\rm jet} = (4.83^{+0.06}_{-0.05}) \times 10^{51} erg. 240619A: f_b = (9.79^{+1.76}_{-2.73}) \times 10^{-2}, E_{\rm jet} = (4.80^{+6.51}_{-0.51}) \times 10^{51} erg. 240910A: f_b = (8.29^{+0.33}_{-0.50}) \times 10^{-4}, E_{\rm jet} = (4.82^{+0.15}_{-0.21}) \times 10^{51} erg. 240916A: f_b = (1.12^{+0.62}_{-0.52}) \times 10^{-3}, E_{\rm jet} = (2.89^{+14.20}_{-1.93}) \times 10^{51} erg.
```

241228B: $f_b = (5.58^{+0.05}_{-0.08}) \times 10^{-5}$, $E_{\rm jet} = (1.50^{+0.01}_{-0.01}) \times 10^{51}$ erg. Overall, the parameters inferred from our TopHat (uniform) jet fits – specifically the observer angle (θ_v) , the jet half-opening angle $(\theta_j \equiv \theta_c$ in this model), and the isotropic-equivalent kinetic energy (E_0) – are consistent with the ranges reported in previous studies of

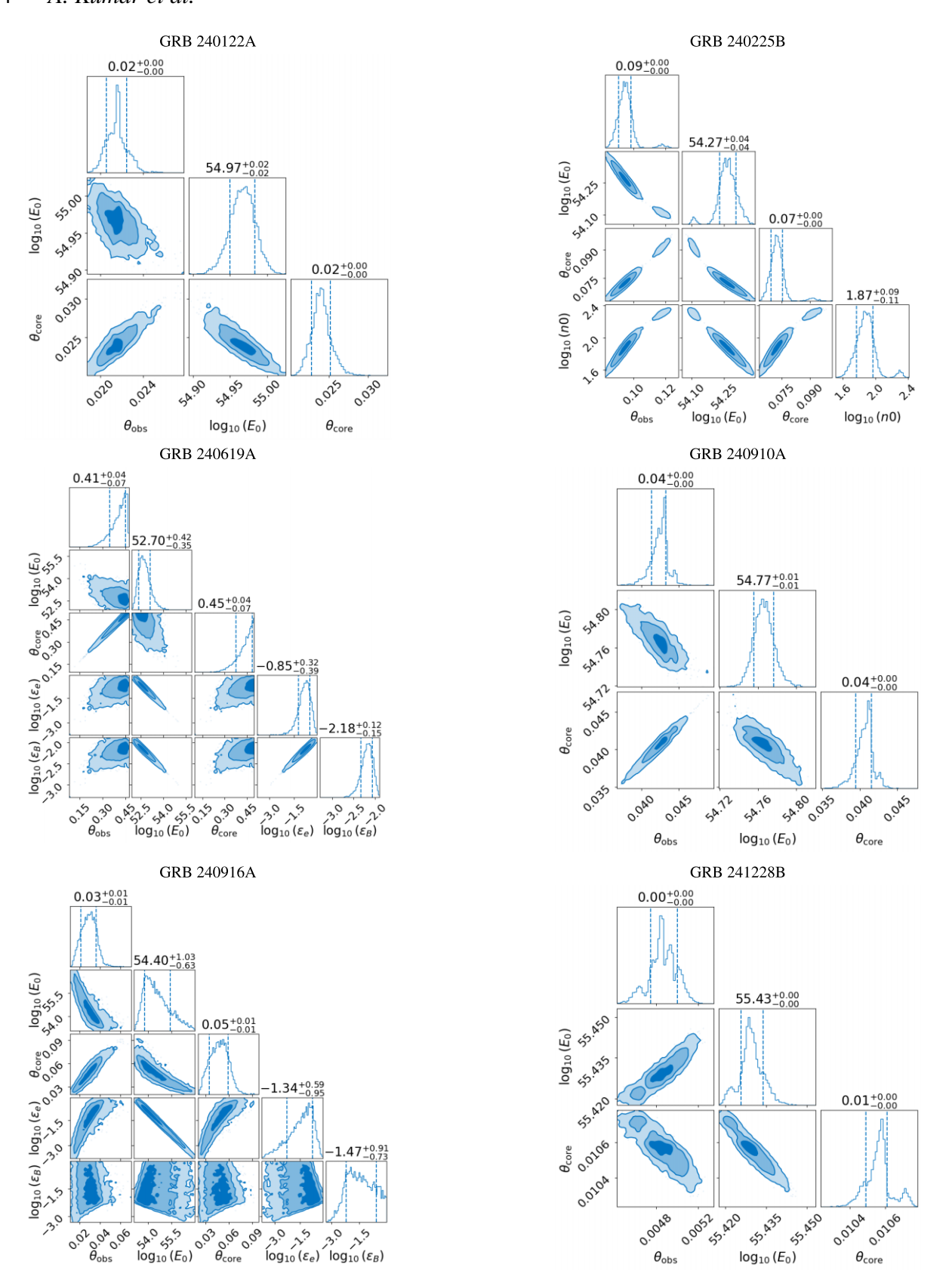


Figure 15. Posterior distributions for the TopHat-jet afterglow model parameters inferred for six GRBs analysed in this work: GRBs 240122A, 240225B, 240619A, 240910A, 240916A, and 241228B. Each panel shows the marginalized 1D and 2D posterior distributions from the dynesty nested-sampling run (via Bilby), with contours representing 68 per cent and 95 per cent credible regions. Inferred parameters include the observer angle, core angle, isotropic-equivalent energy, and microphysical quantities (see the text for details).

long-duration GRB afterglows. In all cases, we recover θ_v and θ_j of order a few degrees, in line with the narrow jet geometries commonly found in broad-band afterglow fits [e.g. D. A. Frail et al. (2001), J. S. Bloom, D. A. Frail & S. R. Kulkarni (2003), A. S. Friedman & J. S. Bloom (2005), J. L. Racusin et al. (2009)]. We use E_0 to estimate the beaming-corrected jet kinetic energy, yielding values that cluster around $10^{51}-10^{52}$ erg, consistent with the canonical long-GRB energy scale (e.g. A. S. Friedman & J. S. Bloom 2005). This agreement in both angular geometry and energetics supports the robustness of our TopHat-jet modelling and places these events firmly within the established population of classical long-duration GRBs.

8 SUMMARY AND CONCLUSION

Over the past few years, the GOTO has become instrumental in the search for, and rapid follow-up of, optical counterparts to poorly localized transients such as GRBs and GW events. Since achieving first light in June 2017, GOTO has steadily progressed from its prototype (GOTO-4) phase into a fully operational dual-site facility (GOTO-36).

During the prototype era (2017–2020), the GOTO-4 system responded to 77 Fermi/GBM and 29 Swift/BAT triggers, securing its first optical afterglow detection with GRB 171205A. Following its expansion to GOTO-36, GOTO attempted follow-up observations of more than 257 Fermi, 43 Swift, 28 EP, and 7 GECAM triggers up to 2024 December 31. Whereas, to date, GOTO has issued nearly 80 GCN circulars and yielded \approx 28 confirmed afterglow detections, ranging from rapid identifications such as GRB 230818A within 4.43 min of the trigger, to wide-field discoveries of poorly localized events including GRB 230911A and the SGRB 241105A. Collectively, these results highlight GOTO's ability to respond on time-scales as short as 36 s and to cover hundreds of square degrees in order to identify optical afterglows under challenging localization conditions.

Within this broader context, this study focuses on the first systematic sample of LGRB afterglows detected by GOTO, discovered during 2024. Our sample comprises seven LGRBs (GRBs 240122A, 240225B, 240619A, 240910A, 240916A, 241002B, and 241228B), including two MAXI/GSC events (GRBs 240122A and 240225B), localized to arcminute precision and detected serendipitously during survey operations, and five Fermi/GBM events (GRBs 240619A, 240910A, 240916A, 241002B, and 241228B), recovered through rapid, targeted tiling of degree-scale localization regions. For all seven LGRBs, GOTO provided the earliest optical detections, with response times ranging from \sim 19.3 min to 9.4 h and with sky coverage exceeding 75 per cent of the 95 per cent probability regions for the GBM bursts.

Notably, GRB 241228B provides an illustrative example: its afterglow was identified on the 94.5 per cent probability contour, outside the typical GBM 90 per cent localization region. While the majority of GRB counterparts are recovered within the 90 per cent region, a small fraction are expected to lie beyond, making this a noteworthy case that highlights both the statistical nature of localization regions and the importance of wide-field optical follow-up. These results highlight the adaptability and efficiency of the GOTO network in responding to both well-localized (MAXI/GSC) and more uncertain (Fermi/GBM) GRBs. Regardless of the size or shape of the localization area, GOTO's rapid tiling strategy enabled meaningful coverage and facilitated the identification of several optical afterglows within its fields.

These rapid identifications enabled immediate triggering of Swift/XRT and UVOT observations and coordinated multiwavelength follow-up using facilities around the globe, underscoring the central role of optical discovery of poorly localized GRBs in constraining their properties. The follow-up campaign yielded detections in the X-ray, UV, optical, and radio bands for most of the events in our sample. Swift/XRT confirmed X-ray counterparts for all bursts. Optical photometry from multiple facilities provided light curves extending from minutes to days post-trigger, showing a broad range of brightnesses and decay rates. Spectroscopy for five events using the VLT/X-shooter (GRBs 240122A, 240225B, 240619A, 240916A, and 241228B) and for two events using GTC/OSIRIS (GRBs 240122A and 240910A) delivered precise redshifts spanning $z \approx 0.40 - 3.16$, along with absorption line diagnostics tracing both host galaxy interstellar media and, for the higher redshift bursts, intervening absorbers. Radio detections for four GRBs (240122A, 240619A, 240910A, and 240916A) utilizing mainly ATCA and VLA confirmed long-lived synchrotron emission, most likely arising from forward shocks. Taken together, this multiwavelength data set has enabled robust classification and placed each burst in the broader context of the LGRB population.

Analysis of the prompt emission using *MAXI*/GSC and *Fermi*/GBM data revealed a spectrally hard sample, with four events yielding measurable $E_{\rm p}$ values (GRBs 240619A, 240910A, 240916A, and 241228B). Two bursts, GRBs 240916A and 241228B, stand out as $>3\sigma$ outliers to the Amati relation, while others displayed unusually hard low-energy photon indices, pointing to diversity in jet microphysics and, in some cases, potentially high magnetization. The measured T_{90} durations, ranging from \sim 20 s to over 270 s, confirm all seven events as LGRBs, encompassing both short-engine and long-engine members of the class.

Comparisons with the broader GRB population reinforce this conclusion. The GOTO-detected afterglows occupy the established luminosity-time phase space of LGRBs in both X-rays and optical, while their radio detections likewise follow the known locus of synchrotron afterglows. Their redshifts ($z \sim 0.40-3.16$) span both nearby and distant events. Taken together, these results demonstrate that the GOTO sample is representative of the wider population, probing afterglows across X-ray, optical, and radio wavelengths and capturing their diversity in temporal evolution and redshift. This highlights GOTO's capability to deliver well-localized optical counterparts that integrate seamlessly with multiwavelength studies of GRBs.

The contrast between typical afterglow behaviour and spectrally hard prompt emission in the GOTO sample likely reflects an observational bias: GRBs with higher $E_{\rm p}$ generally have larger $E_{\rm iso}$ and correspondingly brighter afterglows, making them easier to detect at optical wavelengths. While this tendency favours luminous events in poorly localized searches, it also provides a useful window into jet microphysics and central engine diversity. At the same time, it highlights the importance of wide-field optical facilities in complementing high-energy triggered samples and extending GRB studies across both nearby and high-redshift regimes.

We modelled the afterglows of six of seven GRBs in our sample (excluding GRB 241002B, which lacks a redshift). TopHat-jet parameters inferred here, observer angle ($\theta_{\rm obs}$), jet core angle (θ_c), and isotropic-equivalent kinetic energy (E_0), are consistent with ranges typically found for LGRB afterglows. In all cases, we recover $\theta_{\rm obs}$ and θ_c of order a few degrees, in line with the narrow jet geometries commonly obtained from broad-band afterglow fits. Using E_0 to estimate the true energy budget, the beaming-corrected jet kinetic energies cluster around $10^{51}-10^{52}$ erg, consistent with the canonical

LGRB energy scale after correcting for beaming. Microphysical posteriors are broadly consistent with expectations for external-shock synchrotron emission. One event, GRB 241228B, shows a late-time flux excess relative to the best-fitting TopHat model, suggestive of an additional emission component or prolonged central-engine activity. Taken together, the geometry, energetics, and microphysics inferred from our uniform fits place these GOTO-discovered GRBs squarely within the established population of classical long-duration bursts while clarifying the levers that drive diversity in light-curve morphology. GOTO's early discovery and dense optical cadence provide key leverage for constraining pre-break behaviour and for enabling robust, comparable modelling across events.

In all, the results presented in this study clearly demonstrate that GOTO's wide-field, dual-site, fully robotic design, combined with adaptive trigger specific strategies, is highly effective for bridging the gap between poorly localized high-energy triggers and the precise positions needed for multiwavelength follow-up. The detections presented here highlight GOTO's ability to recover GRB afterglows in a wide range of redshifts, localization scales, and intrinsic properties, spanning both representative events and rare, energetically extreme outliers. In the emerging era of multimessenger astronomy, GOTO's demonstrated capability for rapid, deep optical searches makes it a critical asset for identifying and characterizing counterparts to both gravitational wave events and gamma-ray bursts, thus advancing our understanding of the most energetic explosions in the Universe.

ACKNOWLEDGEMENTS

This work makes use of the Gravitational-wave Optical Transient Observer (GOTO) observations that led to the discovery of the optical afterglows presented in this study. GOTO project acknowledges support from the Science and Technology Facilities Council (STFC, grant numbers ST/T007184/1, ST/T003103/1, ST/T000406/1, ST/X001121/1 and ST/Z000165/1) and the GOTO consortium institutions; University of Warwick; Monash University; University of Sheffield; University of Leicester; Armagh Observatory & Planetarium; the National Astronomical Research Institute of Thailand (NARIT); University of Manchester; Instituto de Astrofísica de Canarias (IAC); University of Portsmouth; University of Turku.

This work is partly based on observations collected at the European Organisation for Astronomical Research in the Southern Hemisphere under ESO programmes 110.24CF and 114.27PZ (Co-PIs Tanvir, Malesani, Vergani).

It is also partly based on data obtained with the instrument OSIRIS, built by a Consortium led by the Instituto de Astrofísica de Canarias in collaboration with the Instituto de Astronomía of the Universidad Autónoma de México. OSIRIS was funded by GRANTECAN and the National Plan of Astronomy and Astrophysics of the Spanish Government.

It is also partly based on data obtained with the ATCA and we acknowledge the Gomeroi people as the traditional owners of the ATCA observatory site. The ATCA is part of the Australia Telescope National Facility, which is funded by the Australian Government for operation as a National Facility managed by CSIRO.

It is also partly based on observations made with the Nordic Optical Telescope, owned in collaboration by the University of Turku and Aarhus University, and operated jointly by Aarhus University, the University of Turku and the University of Oslo, representing Denmark, Finland and Norway, the University of Iceland and Stockholm University at the Observatorio del Roque

de los Muchachos, La Palma, Spain, of the Instituto de Astrofisica de Canarias. The NOT data were obtained under program IDs 68-020, 69-023, and 70-507 (PIs Malesani, Fynbo, Xu). The National Radio Astronomy Observatory and Green Bank Observatory are facilities of the U.S. National Science Foundation operated under cooperative agreement by Associated Universities, Inc. Mephisto is developed at and operated by the South-Western Institute for Astronomy Research of Yunnan University (SWIFAR-YNU), funded by the 'Yunnan University Development Plan for World-Class University' and 'Yunnan University Development Plan for World-Class Astronomy Discipline'. Based on observations made at the Observatorio de Sierra Nevada (OSN), operated by the Instituto de Astrofísica de Andalucía (IAA-CSIC).

AK and JRM are supported by the UK Science and Technology Facilities Council (STFC) Consolidated grant ST/V000853/1. BPG acknowledges support from STFC grant No. ST/Y002253/1. BPG and DO acknowledge support from the Leverhulme Trust grant no. RPG-2024-117. BS and SDV acknowledge the support of the French Agence Nationale de la Recherche (ANR), under grant ANR-23-CE31-0011 (project PEGaSUS). DS is supported by the UK Science and Technology Facilities Council (STFC, grant numbers ST/T007184/1, ST/T003103/1, and ST/T000406/1). SG acknowledges support from the Istituto Nazionale di Astrofisica (INAF), project number: 1.05.24.07.04. BK acknowledges support from the 'Special Project for High-End Foreign Experts,' Xingdian Funding from Yunnan Province; the Yunnan Key Laboratory of Survey Science (grant 202449CE340002), and National Key Research and Development Program of China (grant 2024YFA1611603). BW is supported by the UKRI's STFC studentship grant funding, project reference ST/X508871/1. RLCS and SM acknowledge support from the Leverhulme Trust grant RPG-2023-240. NH, POB, and NRT acknowledge support from UKRI/STFC grant ST/W000857/1. JDL acknowledges support from a UK Research and Innovation Future Leaders Fellowship (MR/T020784/1). JC is supported by the Spanish Ministry of Science via the Plan de Generaci\'on de Conocimiento through grant PID2022-143331NB-100. TLK acknowledges a Warwick Astrophysics prize post-doctoral fellowship made possible thanks to a generous philanthropic donation. MAA acknowledges support from grants PID2021-127495NB-I00 (funded by MCIN/AEI/10.13039/501100011033, EU), ASFAE/2022/026 (funded by MCIN, EU NextGenerationEU PRTR-C17.I1), and CIPROM/2022/13 (Generalitat Valenciana). DLC acknowledges support from the UK Science and Technology Facilities Council (STFC) grant number ST/X001121/1. AS acknowledges support by a postdoctoral fellowship from the CNES. AR acknowledges support from the INAF project Supporto Arizona & Italia. AMC and LC acknowledge support from the Irish Research Council Postgraduate Scholarship No. GOIPG/2022/1008. MEW and IW are supported by the UKRI Science and Technology Facilities Council (STFC). DBM is funded by the European Union (ERC, HEAVYMETAL, 101071865). Views and opinions expressed are, however, those of the authors only and do not necessarily reflect those of the European Union or the European Research Council. Neither the European Union nor the granting authority can be held responsible for them. The Cosmic Dawn Center (DAWN) is funded by the Danish National Research Foundation under grant DNRF140. NSP and ASP are grateful to the Russian Science Foundation (project no. 23-12-00220) for their partial support of the data reduction, analysis of data. EVK is grateful to the Ministry of Science and Higher Education of the Russian Federation for financial support of this work; the AZT-33IK telescope is part of the Center for Common Use 'Angara'.

DATA AVAILABILITY

All data sets supporting this study are provided in the paper. Additional data are available from the corresponding author upon reasonable request.

REFERENCES

```
Abbott B. P. et al., 2017a, Phys. Rev. Lett., 119, 161101
```

Abbott B. P. et al., 2017b, ApJ, 848, L13

Ahumada T. et al., 2021, Nat. Astron., 5, 917

Akaike H., 1974, IEEE Trans. Automat. Control., 19, 716

Aksulu M. D., Wijers R. A. M. J., van Eerten H. J., van der Horst A. J., 2022, MNRAS, 511, 2848

Aloy M. Á., Obergaulinger M., 2021, MNRAS, 500, 4365

Aloy M. A., Müller E., Ibáñez J. M., Martí J. M., MacFadyen A., 2000, ApJ, 531, L119

Aloy M. A., Cuesta-Martínez C., Obergaulinger M., 2018, MNRAS, 478, 3576

Amati L., 2006, MNRAS, 372, 233

Amati L., Della Valle M., 2013, Int. J. Mod. Phys. D, 22, 1330028

Amati L. et al., 2002, A&A, 390, 81

An J. et al., 2024, GCN Circ., 38704, 1

Anderson G. E., Leung J. K., Murphy T., Lenc E., Rhodes L., van der Horst A. J., Rowell G., 2023, GCN Circ., 33475, 1

Anderson G. E. et al., 2024a, ApJ, 975, L13

Anderson G. E., Gulati A., Rhodes L., Leung J. K., van der Horst A. J., Chastain S., PanRadio GRB Collaboration, 2024b, GCN Circ., 35642, 1

Anderson G. E. et al., 2025, preprint (arXiv:2508.14650)

Ashton G. et al., 2019, ApJS, 241, 27

Band D. et al., 1993, ApJ, 413, 281

Belkin S. et al., 2023, GCN Circ., 34681, 1

Belkin S. et al., 2024, Res. Notes Am. Astron. Soc., 8, 6

Beniamini P., van der Horst A. J., 2017, MNRAS, 472, 3161

Beniamini P., Granot J., Gill R., 2020, MNRAS, 493, 3521

Berger E. et al., 2000, ApJ, 545, 56

Berger E. et al., 2001a, ApJ, 556, 556

Berger E., Kulkarni S. R., Frail D. A., 2001b, ApJ, 560, 652

Berger E. et al., 2005, Nature, 438, 988

Bhat P. N. et al., 2016, ApJS, 223, 28

Björnsson G., Gudmundsson E. H., Jóhannesson G., 2004, ApJ, 615, L77

Bloom J. S., Frail D. A., Kulkarni S. R., 2003, ApJ, 594, 674

Boch T., Fernique P., Bonnarel F., Chaitra C., Bot C., Pineau F. X., Baumann M., Michel L., 2020, in Pizzo R., Deul E. R., Mol J. D., de Plaa J., Verkouter H., eds, ASP Conf. Ser. Vol. 527, Astronomical Data Analysis Software and Systems XXIX. Astron. Soc. Pac., San Francisco, p. 121

Bradley L. et al., 2024, astropy/photutils: 2.0.2

Breeveld A. A., Landsman W., Holland S. T., Roming P., Kuin N. P. M., Page M. J., 2011, in McEnery J. E., Racusin J. L., Gehrels N., eds, AIP Conf. Proc. Vol. 1358, Gamma Ray Bursts 2010. Am. Inst. Phys., New York, p. 373

Bromberg O., Nakar E., Piran T., Sari R., 2013, ApJ, 764, 179

Burrows D. N. et al., 2005, Space Sci. Rev., 120, 165

Cano Z., Wang S.-Q., Dai Z.-G., Wu X.-F., 2017, Adv. Astron, 2017, 8929054

Cash W., 1979, ApJ, 228, 939

Cenko S. B. et al., 2006, ApJ, 652, 490

Cenko S. B. et al., 2011, ApJ, 732, 29

Cenko S. B. et al., 2012, ApJ, 753, 77

Cepa J., 1998, Ap&SS, 263, 369

Chambers K. C. et al., 2016, preprint (arXiv:1612.05560)

Chandra P. et al., 2008, ApJ, 683, 924

Chandra P. et al., 2010, ApJ, 712, L31

Chen Y. et al., 2020, Sci. Sinica Phys. Mech. Astron., 50, 129507

Chen X. et al., 2024, ApJ, 971, L2

Cheng Y. et al., 2025, ApJ, 979, 38

Cheung C. C., Woolf R., Kerr M., Grove J. E., Goldstein A., Wilson-Hodge C. A., Kocevski D., Briggs M. S., 2024, GCN Circ., 35848, 1

Chrimes A. A. et al., 2022, MNRAS, 515, 2591

```
Christensen L., Fynbo J. P. U., Prochaska J. X., Thöne C. C., de Ugarte
Postigo A., Jakobsson P., 2011, ApJ, 727, 73
```

Clark B. G., 1980, A&A, 89, 377

Costa E. et al., 1997, Nature, 387, 783

Cotter L. et al., 2024, GCN Circ., 36813, 1

Craig M. et al., 2017, astropy/ccdproc: v1.3.0.post1. https://doi.org/10.5281/ zenodo.1069648

Dafcikova M. et al., 2024a, GCN Circ., 36724, 1

Dafcikova M. et al., 2024b, GCN Circ., 37543, 1

Dai C.-Y., Guo C.-L., Zhang H.-M., Liu R.-Y., Wang X.-Y., 2024, ApJ, 962, L37

Dainotti M. G. et al., 2024, MNRAS, 533, 4023

Dalessi S., Meegan C., Fermi Gamma-ray Burst Monitor Team, 2024, GCN Circ., 36717, 1

de Ugarte Postigo A. et al., 2024, GCN Circ., 37467, 1

DeLaunay J., Tohuvavohu A., Ronchini S., Raman G., Kennea J. A., Parsotan T., 2024a, GCN Circ., 37704, 1

DeLaunay J., Ronchini S., Tohuvavohu A., Raman G., Kennea J. A., Parsotan T., 2024b, GCN Circ., 38700, 1

Demianski M., Piedipalumbo E., Sawant D., Amati L., 2017, A&A, 598, A112

Dereli H., Boër M., Gendre B., Amati L., Dichiara S., Orange N. B., 2017, ApJ, 850, 117

Devyatkin A. V., Gorshanov D. L., Kouprianov V. V., Verestchagina I. A., 2010, Sol. Syst. Res., 44, 68

Di Lalla N., Holzmann Airasca A., Khalil T., Lopez S., Depalo D., Cheung C. C., Bartolini C., Fermi-LAT Collaboration, 2025, GCN Circ., 38843, 1

Dimple P. J. et al., 2025, MNRAS, available at: https://doi.org/10.1093/mnras/staf1574

Djorgovski S. G., Frail D. A., Kulkarni S. R., Bloom J. S., Odewahn S. C., Diercks A., 2001, ApJ, 562, 654

Djupvik A. A., Andersen J., 2010, in Diego J. M., Goicoechea L. J., González-Serrano J. I., Gorgas J., eds, Astrophysics and Space Science Proceedings, Vol. 14, Highlights of Spanish Astrophysics V. Springer, Berlin, p. 211

Duncan R. A., van der Horst A. J., Beniamini P., 2023, MNRAS, 518, 1522

Durbak J., Guiffreda O., Atri S., Kutyrev A. S., Troja E., De K., Cenko S. B., 2024a, GCN Circ., 37700, 1

Durbak J., Guiffreda O., Atri S., Kutyrev A. S., Troja E., De K., Cenko S. B., 2024b, GCN Circ., 37712, 1

Dyer M. J. et al., 2020, in Marshall H. K., Spyromilio J., Usuda T., eds, Proc. SPIE Conf. Ser. Vol. 11445, Ground-based and Airborne Telescopes VIII. SPIE, Bellingham, p. 114457G

Dyer M. J. et al., 2024, in Marshall H. K., Spyromilio J., Usuda T., eds, Proc. SPIE Conf. Ser. Vol. 13094, Ground-based and Airborne Telescopes X. SPIE, Bellingham, p. 130941X

Eichler D., Livio M., Piran T., Schramm D. N., 1989, Nature, 340, 126

Evans P. A. et al., 2007, A&A, 469, 379

Evans P. A. et al., 2009, MNRAS, 397, 1177

Fermi GBM Team, 2024a, GCN Circ., 36694, 1

Fermi GBM Team, 2024b, GCN Circ., 37441, 1

Fermi GBM Team, 2024c, GCN Circ., 37518, 1 Fermi GBM Team, 2024d, GCN Circ., 37668, 1

Fermi GBM Team, 2024e, GCN Circ., 37008, 1

Fermi GBM Team, 2024f, GCN Circ., 38682, 1

Fiore F., 2001, in Inoue H., Kunieda H., eds, ASP Conf. Ser. Vol. 251, New Century of X-ray Astronomy. Astron. Soc. Pac., San Francisco, p. 168

Flewelling H., 2018, American Astronomical Society Meeting Abstracts, Vol. 231, 436.01

Fong W. et al., 2014, ApJ, 780, 118

Fong W. et al., 2021, ApJ, 906, 127

Fontana A. et al., 2014, A&A, 570, A11

Frail D. A., Kulkarni S. R., Nicastro L., Feroci M., Taylor G. B., 1997, Nature, 389, 261

Frail D. A. et al., 1999, ApJ, 525, L81

Frail D. A. et al., 2000, ApJ, 538, L129

Frail D. A. et al., 2001, ApJ, 562, L55

Frail D. A., Soderberg A. M., Kulkarni S. R., Berger E., Yost S., Fox D. W., Harrison F. A., 2005, ApJ, 619, 994

```
Frail D. A. et al., 2006, ApJ, 646, L99
Frederiks D., Lysenko A., Ridnaia A., Svinkin D., Tsvetkova A., Ulanov M.,
   Cline T., Konus-Wind Team, 2024, GCN Circ., 35835, 1
Friedman A. S., Bloom J. S., 2005, ApJ, 627, 1
Fynbo J. P. U. et al., 2009, ApJS, 185, 526
Galama T. J. et al., 1998, IAU Circ., 6895
Galama T. J. et al., 2000, ApJ, 541, L45
Galama T. J., Frail D. A., Sari R., Berger E., Taylor G. B., Kulkarni S. R.,
   2003, ApJ, 585, 899
Gehrels N. et al., 2004, ApJ, 611, 1005
Ghosh A., Razzaque S., Moskvitin A., Sotnikova Y., Dukiya N., Gupta R.,
   2024, GCN Circ., 38702, 1
Giallongo E. et al., 2008, A&A, 482, 349
Giarratana S., Giroletti M., Ghirlanda G., Di Lalla N., Omodei N., Salafia O.
   S., 2024a, GCN Circ., 37569, 1
Giarratana S., Giroletti M., Ghirlanda G., Di Lalla N., Omodei N., Salafia O.
   S., 2024b, GCN Circ., 37788, 1
Goldoni P., Royer F., François P., Horrobin M., Blanc G., Vernet J., Modigliani
   A., Larsen J., 2006, in McLean I. S., Iye M., eds, Proc. SPIE Conf. Ser.
   Vol. 6269, Ground-based and Airborne Instrumentation for Astronomy.
   SPIE, Bellingham, p. 822
Goldstein A. et al., 2017, ApJ, 848, L14
Goldstein A., Cleveland W. H., Kocevski D., 2023, Fermi Gamma-Ray Data
   Tools: v2.0.0. Available at: https://github.com/USRA-STI/gdt-fermi
Gompertz B. P. et al., 2020, MNRAS, 497, 726
Gompertz B. P. et al., 2023a, Nat. Astron., 7, 67
Gompertz B. et al., 2023b, GCN Circ., 34023, 1
Gompertz B. P. et al., 2023c, GCN Circ., 34480, 1
Gompertz B. P. et al., 2024a, GCN Circ., 35805, 1
Gompertz B. P. et al., 2024b, GCN Circ., 36715, 1
Gompertz B. P. et al., 2024c, GCN Circ., 37522, 1
Goodman J., 1997, New Astron., 2, 449
Gordon C., Arnaud K., 2021, record ascl:2101.014
Górski K. M., Hivon E., Banday A. J., Wandelt B. D., Hansen F. K., Reinecke
   M., Bartelmann M., 2005, ApJ, 622, 759
Gottlieb O., Bromberg O., Singh C. B., Nakar E., 2020, MNRAS, 498, 3320
Granot J., Sari R., 2002, ApJ, 568, 820
Greiner J. et al., 2013, A&A, 560, A70
Gruber D. et al., 2014, ApJS, 211, 12
Guiffreda O., Durbak J., Atri S., Kutyrev A. S., Troja E., Cenko S. B., 2024,
   GCN Circ., 37736, 1
Hancock P. J., Murphy T., Gaensler B., Zauderer A., 2012, GCN Circ., 12804,
Harrison F. A. et al., 1999, ApJ, 523, L121
Harrison F. A. et al., 2001, ApJ, 559, 123
He J. et al., 2025, Exp. Astron., 59, 15
Horesh A., Cenko S. B., Perley D. A., Kulkarni S. R., Hallinan G., Bellm E.,
   2015, ApJ, 812, 86
Huang B. et al., 2024, ApJS, 271, 13
Izzo L. et al., 2019, Nature, 565, 324
Izzo L. et al., 2024, GCN Circ., 38167, 1
Joshi J., Waratkar G., Vibhute A., Bhalerao V., Bhattacharya D., Rao A. R.,
   Vadawale S., AstroSat CZTI Collaboration, 2024, GCN Circ., 35798, 1
Julakanti Y. et al., 2024a, GCN Circ., 37459, 1
Julakanti Y. et al., 2024b, GCN Circ., 38088, 1
Kawakubo Y. et al., 2024, GCN Circ., 35811, 1
Killestein T. L. et al., 2021, MNRAS, 503, 4838
Klebesadel R. W., Strong I. B., Olson R. A., 1973, ApJ, 182, L85
Kouprianov V., 2012, in 39th COSPAR Scientific Assembly, Apex II +
   FORTE: Data Acquisition Software for Space Surveillance. Mysore,
Kouveliotou C., Meegan C. A., Fishman G. J., Bhat N. P., Briggs M. S.,
   Koshut T. M., Paciesas W. S., Pendleton G. N., 1993, ApJ, 413, L101
Krogager J.-K., 2018, preprint (arXiv:1803.01187)
Kulkarni S., Desai S., 2017, Ap&SS, 362, 70
```

```
Kumar A. et al., 2024c, GCN Circ., 37676, 1
Kumar A. et al., 2024d, GCN Circ., 38684, 1
Lamb G. P., Kobayashi S., 2017, MNRAS, 472, 4953
Lamb G. P. et al., 2019, ApJ, 883, 48
Lang D., Hogg D. W., Mierle K., Blanton M., Roweis S., 2010, AJ, 139, 1782
Laskar T. et al., 2013, ApJ, 776, 119
Laskar T., Berger E., Margutti R., Perley D., Zauderer B. A., Sari R., Fong
    W.-f., 2015, ApJ, 814, 1
Laskar T. et al., 2016, ApJ, 833, 88
Laskar T. et al., 2018, ApJ, 859, 134
Laskar T. et al., 2022, ApJ, 935, L11
Laskar T. et al., 2023, ApJ, 946, L23
Lazzati D., Begelman M. C., 2005, ApJ, 629, 903
Lazzati D., Morsony B. J., Margutti R., Begelman M. C., 2013, ApJ, 765,
Levan A., Crowther P., de Grijs R., Langer N., Xu D., Yoon S.-C., 2016,
   Space Sci. Rev., 202, 33
Levan A. J. et al., 2024, Nature, 626, 737
LHAASO Collaboration 2023, Science, 380, 1390
Liang E., Zhang B., Virgili F., Dai Z. G., 2007, ApJ, 662, 1111
Lundman C., Pe'er A., Ryde F., 2013, MNRAS, 428, 2430
Luongo O., Muccino M., 2021, Galaxies, 9, 77
Lupton R. H. et al., 2005, American Astronomical Society Meeting Abstracts,
   133.08
Maeder A., Meynet G., 2012, Rev. Mod. Phys., 84, 25
Margutti R. et al., 2013, ApJ, 778, 18
Matsuoka M. et al., 2009, PASJ, 61, 999
Mazets E. P., Golenetskii S. V., Aptekar R. L., Gurian I. A., Ilinskii V. N.,
    1981, Nature, 290, 378
McMullin J. P., Waters B., Schiebel D., Young W., Golap K., 2007, in Shaw
   R. A., Hill F., Bell D. J., eds, ASP Conf. Ser. Vol. 376, Astronomical Data
    Analysis Software and Systems XVI. Astron. Soc. Pac., San Francisco,
   p. 127
Meegan C. A., Fishman G. J., Wilson R. B., Paciesas W. S., Pendleton G. N.,
   Horack J. M., Brock M. N., Kouveliotou C., 1992, Nature, 355, 143
Meegan C. et al., 2009, ApJ, 702, 791
Mészáros P., 2013, Astropart. Phys., 43, 134
Metzger B. D., 2019, Living Rev. Relativ., 23, 1
Metzger M. R., Djorgovski S. G., Kulkarni S. R., Steidel C. C., Adelberger
   K. L., Frail D. A., Costa E., Frontera F., 1997, Nature, 387, 878
Miceli D., Nava L., 2022, Galaxies, 10, 66
Mihara T. et al., 2011, PASJ, 63, S623
Mimica P., Aloy M. A., 2012, MNRAS, 421, 2635
Mimica P., Giannios D., Aloy M. A., 2009, A&A, 494, 879
Mimica P., Giannios D., Aloy M. A., 2010, MNRAS, 407, 2501
Minaev P. Y., Pozanenko A. S., 2020, MNRAS, 492, 1919
Mo G. et al., 2023, GCN Circ., 36739, 1
Mo G., Karambelkar V., Frostig D., Stein R., Lourie N., Ahumada T., Simcoe
    R., Kasliwal M., 2024, GCN Circ., 35829, 1
Modigliani A. et al., 2010, in Silva D. R., Peck A. B., Soifer B.T., eds,
   Proc. SPIE Conf. Ser. Vol. 7737, Observatory Operations: Strategies,
    Processes, and Systems III. SPIE, Bellingham, p. 572
Moin A. et al., 2013, ApJ, 779, 105
Mong Y. L. et al., 2021, MNRAS, 507, 5463
Moresco M. et al., 2022, Living Rev. Relativ., 25, 6
Moskvitin A. S., Spiridonova O. I., GRB follow-up Team., 2024a, GCN Circ.,
   35828, 1
Moskvitin A. S., Spiridonova O. I., GRB follow-up Team., 2024b, GCN Circ.,
Moskvitin A. S., Spiridonova O. I., Sotnikova Y. V., Volnova A., Pozanenko
   A., Ghosh A., Razzaque S., GRB follow-up Team, 2024c, GCN Circ.,
   38733, 1
Mundell C. G. et al., 2007, ApJ, 660, 489
Nakajima M. et al., 2024, GCN Circ., 35796, 1
Narayan R., Paczynski B., Piran T., 1992, ApJ, 395, L83
Nasa High Energy Astrophysics Science Archive Research Center (Heasarc),
   2014, record ascl:1408.004
```

Negoro H. et al., 2024, GCN Circ., 35593, 1

Kumar P., Zhang B., 2015, Phys. Rep., 561, 1

Kumar A. et al., 2024a, MNRAS, 531, 3297

Kumar A. et al., 2024b, GCN Circ., 35596, 1

```
Nicholl M. et al., 2023, ApJ, 954, L28
O'Connor B. et al., 2023, Sci. Adv., 9, eadi1405
Obergaulinger M., Aloy M. Á., 2021, MNRAS, 503, 4942
Obergaulinger M., Aloy M. Á., 2022, MNRAS, 512, 2489
Oganesyan G., Ascenzi S., Branchesi M., Salafia O. S., Dall'Osso S.,
   Ghirlanda G., 2020, ApJ, 893, 88
Ortega-Casas I. et al., 2024, GCN Circ., 38692, 1
Panaitescu A., Kumar P., 2002, ApJ, 571, 779
Pankov N., Pozanenko A., Kouprianov V., Belkin S., 2022, in Pozanenko A.,
   Stupnikov S., Thalheim B., Mendez E., Kiselyova N., eds, Data Analytics
   and Management in Data Intensive Domains. Springer International
   Publishing, Cham, p. 104
Pawar D., 2024, GCN Circ., 37519, 1
Perley D. A. et al., 2008, ApJ, 688, 470
Perley D. A. et al., 2014, ApJ, 781, 37
Petitjean P., Vergani S. D., 2011, C. R. Phys., 12, 288
Pian E. et al., 2017, Nature, 551, 67
Pieterse D. et al., 2024, GCN Circ., 37532, 1
Price P. A. et al., 2002, ApJ, 572, L51
Racusin J. L. et al., 2009, ApJ, 698, 43
Rastinejad J. C. et al., 2022, Nature, 612, 223
Ravasio M. E., Oganesyan G., Ghirlanda G., Nava L., Ghisellini G., Pescalli
   A., Celotti A., 2018, A&A, 613, A16
Ravasio M. E., Ghirlanda G., Nava L., Ghisellini G., 2019, A&A, 625, A60
Reynolds J., 1994, A Revised Flux Scale for the at Compact Array. Available
   at: https://www.atnf.csiro.au/observers/memos/d96783 1.pdf
Rhoads J. E., 1999, ApJ, 525, 737
Rhodes L. et al., 2024, MNRAS, 533, 4435
Rhodes L., Fender R., Green D., Titterington D., 2024, GCN Circ., 36744, 1
Ripa J. et al., 2024, GCN Circ., 37450, 1
Roberts O. J., Meegan C., Fermi Gamma-ray Burst Monitor Team, 2024a,
   GCN Circ., 37535, 1
Roberts O. J., Hamburg R., Meegan C., Fermi Gamma-ray Burst Monitor
   Team, 2024b, GCN Circ., 37711, 1
Rol E. et al., 2007, ApJ, 669, 1098
Roming P. W. A. et al., 2005, Space Sci. Rev., 120, 95
Ror A. K., Pandey S. B., Gupta R., Aryan A., Pandey S., 2024, GCN Circ.,
   35830.1
Ror A. K., Gupta A., Pranshu, Pandey S. B., Mishra K., 2025, GCN Circ.,
   38816, 1
Rossi A. et al., 2022, ApJ, 932, 1
Ryan G., van Eerten H., Piro L., Troja E., 2020, ApJ, 896, 166
Saccardi A. et al., 2023, A&A, 671, A84
Saccardi A. et al., 2024, GCN Circ., 35599, 1
Saccardi A. et al., 2025, preprint (arXiv:2506.04340)
Sari R., Piran T., 1999, A&AS, 138, 537
Sari R., Piran T., Narayan R., 1998, ApJ, 497, L17
Sasada M. et al., 2024, GCN Circ., 35831, 1
Sault R. J., Teuben P. J., Wright M. C. H., 1995, in Shaw R. A., Payne H. E.,
   Hayes J. J. E., eds, ASP Conf. Ser. Vol. 77, Astronomical Data Analysis
   Software and Systems IV. Astron. Soc. Pac., San Francisco, p. 433
Savaglio S., Fall S. M., 2004, ApJ, 614, 293
Schlafly E. F., Finkbeiner D. P., 2011, ApJ, 737, 103
Schneider B. et al., 2024, GCN Circ., 35832, 1
Schroeder G. et al., 2024, ApJ, 970, 139
Schulze S. et al., 2011, A&A, 526, A23
Scotton L., Meegan C., Fermi Gamma-ray Burst Monitor Team, 2024, GCN
   Circ., 38714, 1
Selsing J. et al., 2019, A&A, 623, A92
Shingles L. et al., 2021, Transient Name Server AstroNote, 7, 1
Siegel M. H., D'Elia V., Swift/UVOT Team, 2024, GCN Circ., 35613, 1
Soderberg A. M. et al., 2004a, ApJ, 606, 994
Soderberg A. M., Frail D. A., Wieringa M. H., 2004b, ApJ, 607, L13
Soderberg A. M. et al., 2006, ApJ, 650, 261
```

Steeghs D. et al., 2017, GCN Circ., 22190, 1 Steeghs D. et al., 2022, MNRAS, 511, 2405

Strobl J., Jelinek M., 2024, GCN Circ., 38715, 1

Steele I. A. et al., 2004, in Oschmann Jacobus M. J., ed., Proc. SPIE Conf. Ser. Vol. 5489, Ground-based Telescopes. SPIE, Bellingham, p. 679

```
Strong I. B., Klebesadel R. W., Olson R. A., 1974, ApJ, 188, L1
Sun H. et al., 2025, Natl. Sci. Rev., 12, nwae401
Svinkin D., Frederiks D., Ulanov M., Tsvetkova A., Lysenko A., Ridnaia A.,
   Cline T., Konus-Wind Team, 2024, GCN Circ., 36768, 1
SVOM/GRM Team, 2024, GCN Circ., 37445, 1
SVOM/VT Team, 2024, GCN Circ., 37503, 1
Tanaka M., 2016, Adv. Astron., 2016, 634197
Tanvir N. R. et al., 2009, Nature, 461, 1254
Tanvir N. R. et al., 2017, ApJ, 848, L27
Taylor G. B., Frail D. A., Kulkarni S. R., Shepherd D. S., Feroci M., Frontera
   F., 1998, ApJ, 502, L115
Thoene C. C. et al., 2024, GCN Circ., 35598, 1
Tingay S. J., Jauncey D. L., King E. A., Tzioumis A. K., Lovell J. E. J.,
   Edwards P. G., 2003, PASJ, 55, 351
Tody D., 1986, in Crawford D. L., ed., Proc. SPIE Conf. Ser. Vol. 627,
   Instrumentation in Astronomy VI. SPIE, Bellingham, p. 733
Tomaney A. B., Crotts A. P. S., 1996, AJ, 112, 2872
Tonry J. L. et al., 2018, PASP, 130, 064505
Torii S. et al., 2024, GCN Circ., 36719, 1
Torreiro Martínez M. et al., 2024, GCN Circ., 37692, 1
Troja E. et al., 2017, Nature, 551, 71
Troja E. et al., 2022, Nature, 612, 228
Valenti S. et al., 2017, ApJ, 848, L24
van Eerten H., 2018, Int. J. Mod. Phys. D, 27, 1842002
van Eerten H., Zhang W., MacFadyen A., 2010, ApJ, 722, 235
van Paradijs J. et al., 1997, Nature, 386, 686
van der Horst A. J. et al., 2008, A&A, 480, 35
Vernet J. et al., 2011, A&A, 536, A105
von Kienlin A. et al., 2014, ApJS, 211, 13
von Kienlin A. et al., 2020, ApJ, 893, 46
Wang H. et al., 2017, ApJ, 851, L18
Wei J. et al., 2016, preprint (arXiv:1610.06892)
Weiler K. W., Panagia N., Montes M. J., Sramek R. A., 2002, ARA&A, 40,
Willingale R., Starling R. L. C., Beardmore A. P., Tanvir N. R., O'Brien P.
   T., 2013, MNRAS, 431, 394
Wilms J., Allen A., McCray R., 2000, ApJ, 542, 914
Woosley S. E., 1993, ApJ, 405, 273
Woosley S. E., Bloom J. S., 2006, ARA&A, 44, 507
Yang J. et al., 2022, Nature, 612, 232
Yang Y.-P. et al., 2024, ApJ, 969, 126
Yi S.-X., Wu X.-F., Zou Y.-C., Dai Z.-G., 2020, ApJ, 895, 94
York D. G. et al., 2000, AJ, 120, 1579
Yuan W. et al., 2015, preprint (arXiv:1506.07735)
Yuan X. et al., 2020, in Marshall H. K., Spyromilio J., Usuda T., eds, Proc.
   SPIE Conf. Ser. Vol. 11445, Ground-based and Airborne Telescopes VIII.
   SPIE, Bellingham, p. 114457M
Yuan W., Zhang C., Chen Y., Ling Z., 2022, in Bambi C., Sangangelo A.,
   eds, Handbook of X-ray and Gamma-ray Astrophysics, Springer Living
   Reference Work. Springer, Singapore, p. 86
Zhang B., 2019, The Physics of Gamma-Ray Bursts. Cambridge Univ. Press,
   Cambridge
Zhang B., Kobayashi S., 2005, ApJ, 628, 315
Zhang W., Woosley S. E., Heger A., 2004, ApJ, 608, 365
Zhang B., Fan Y. Z., Dyks J., Kobayashi S., Mészáros P., Burrows D. N.,
   Nousek J. A., Gehrels N., 2006, ApJ, 642, 354
Zhang B. et al., 2009, ApJ, 703, 1696
```

Zou X. et al., 2025, preprint (arXiv:2505.19831)

APPENDIX:

Zhang B. B. et al., 2021, Nat. Astron., 5, 911

Zhang F.-W., Shao L., Yan J.-Z., Wei D.-M., 2012, ApJ, 750, 88

Zhang L.-L., Zhong S.-Q., Xin L.-P., Liang E.-W., 2024, ApJ, 972, 170

Table A1. Optical afterglow observations of GRBs 240122A, 240225B, 240619A, 240910A, 240916A, 241002B, and 241228B compiled within this work, along with those collected from the reported GCNs. All the tabulated magnitudes are in AB system.

$T-T_0$ (h)	Instrument/Telescope	Exp. Time	Filter	Mag	Mag err	Source
		GRB 240122A (T ₀ =				
0.728	GOTO-S	$4 \times 45 \mathrm{s}$	L	17.581	0.037	This work
9.800	0.6m BOOTES-2	$14 \times 60 \mathrm{s}$	clear	>17.81		This work
9.836	UVOT/Swift	481 s	и	>20.4		M. H. Siegel, V. D'Elia &
12 210	OCIDIC/CTC	20 -	/	20, 421	0.115	Swift/UVOT Team (2024)
2.318	OSIRIS/GTC	30 s	r'	20.431	0.115	This work
3.837	1.5m OSN	$10 \times 90 \mathrm{s}$	V	20.73	0.18	This work
3.865	1.5m OSN	$11 \times 90 \mathrm{s}$	В	>22.09	0.00	This work
3.892	1.5m OSN	$10 \times 90 \mathrm{s}$	I	20.73	0.08	This work
3.907	1.5m OSN	$11 \times 90 \mathrm{s}$	R	20.94	0.09	This work
3.168	IO:O/LT	$3 \times 60 \mathrm{s}$	r	20.396	0.207	This work
3.237	IO:O/LT	$3 \times 60 \mathrm{s}$	i	20.489	0.200	This work
3.307	IO:O/LT	$3 \times 60 \mathrm{s}$	z	20.461	0.255	This work
5.666	X-shooter/VLT	$11 \times 20 \mathrm{s}$	r'	20.652	0.033	This work
5.689	X-shooter/VLT	$3 \times 60 \mathrm{s}$	r'	20.610	0.046	This work
5.778	X-shooter/VLT	$3 \times 60 \mathrm{s}$	g'	21.277	0.026	This work
5.827	X-shooter/VLT	$3 \times 60 \mathrm{s}$	z'	20.494	0.029	This work
6.198	1.5m OSN	$10 \times 90 \mathrm{s}$	B	>22.15		This work
6.225	1.5m OSN	$10 \times 90 \mathrm{s}$	V	21.56	0.28	This work
5.253	1.5m OSN	$10 \times 90 \mathrm{s}$	R	21.83	0.18	This work
6.280	1.5m OSN	$10 \times 90 \mathrm{s}$	I	22.05	0.15	This work
9.202	1.5m OSN	$12 \times 150 \mathrm{s}$	В	>22.31	****	This work
9.247	1.5m OSN	$12 \times 150 \mathrm{s}$ $12 \times 150 \mathrm{s}$	V	>21.96		This work
9.291	1.5m OSN	$12 \times 150 \mathrm{s}$ $12 \times 150 \mathrm{s}$	R	22.19	0.18	This work
9.336	1.5m OSN	$12 \times 150 \mathrm{s}$ $12 \times 150 \mathrm{s}$	I I	23.01	0.28	This work This work
9.330	1.5111 OSIN	GRB 240225B (T_0 =			0.26	THIS WOLK
.501	GOTO-N	$4 \times 45 \mathrm{s}$		17.118	0.043	This wouls
			L			This work
8.90	0.5m HMT	$30 \times 90 \mathrm{s}$	R	18.88	0.12	This work
5.29	0.5m HMT	$30 \times 90 \mathrm{s}$	R	19.81	0.3	This work
5.914	GOTO-N	$4 \times 45 \mathrm{s}$	$L_{'}$	19.694	0.178	This work
6.167	ALFOSC/NOT	$3 \times 300 \mathrm{s}$	r'	19.159	0.016	This work
8.096	IO:O/LT	$2 \times 75 \mathrm{s}$	g	19.971	0.123	This work
8.150	IO:O/LT	$2 \times 75 \mathrm{s}$	r	19.513	0.151	This work
8.204	IO:O/LT	$2 \times 75 \mathrm{s}$	i	19.442	0.105	This work
28.258	IO:O/LT	$2 \times 75 \mathrm{s}$	Z	19.281	0.143	This work
9.312	50cm MITSuME-Akeno	$79 \times 60 \mathrm{s}$	g	19.78	0.13	M. Sasada et al. (2024)
9.312	50cm MITSuME-Akeno	$79 \times 60 \mathrm{s}$	R	19.53	0.10	M. Sasada et al. (2024)
9.312	50cm MITSuME-Akeno	$79 \times 60 \mathrm{s}$	I	>19.7		M. Sasada et al. (2024)
1.261	CMOS/AZT-33IK (Mondy)	$60 \times 60 \mathrm{s}$	R	19.93	0.07	This work
9.359	IO:O/LT	$15 \times 120 \mathrm{s}$	r	20.04	0.05	This work
2.804	3.6m DOT	60 s	i	19.96	0.04	A. K. Ror et al. (2024)
7.656	WINTER/Palomar	$8 \times 120 \mathrm{s}$	J	>18.8		G. Mo et al. (2024)
7.656	WINTER/Palomar	$8 \times 120 \mathrm{s}$	Y	>18.3		G. Mo et al. (2024)
0.238	IO:O/LT	$15 \times 120 \mathrm{s}$	r	20.444	0.124	This work
8.194	CMOS/AZT-33IK (Mondy)	$60 \times 60 \mathrm{s}$	R	20.64	0.11	This work
0.337	Zeiss-1000 (SAO-RAS)	$8 \times 300 \mathrm{s}$	R	20.72	0.02	A. S. Moskvitin, O. I.
0.557	20135 1000 (5/10 1015)	0 X 300 B		20.72	0.02	Spiridonova & GRB
						follow-up Team. (2024a)
3.160	IO:O/LT	$15 \times 180 \mathrm{s}$	**	21.303	0.126	This work
		$3 \times 300 \mathrm{s}$	$rac{r}{r'}$		0.120	This work
5.762	ALFOSC/NOT			20.660		
7.280	X-shooter/VLT	60 s	r'	20.879	0.031	This work
7.324	X-shooter/VLT	$3 \times 60 \mathrm{s}$	r'	20.956	0.035	This work
7.410	X-shooter/VLT	$3 \times 60 \mathrm{s}$	g'	21.055	0.082	This work
7.477	X-shooter/VLT	$3 \times 60 \mathrm{s}$	z'	20.79	0.129	This work
3.367	Zeiss-1000 (SAO RAS)	$8 \times 300 \mathrm{s}$	R	21.32	0.04	A. S. Moskvitin, O. I.
						Spiridonova & GRB
						follow-up Team. (2024b)
13.026	CMOS/AZT-33IK (Mondy)	$60 \times 60 \mathrm{s}$	R	21.73	0.19	This work
37.128	CMOS/AZT-33IK (Mondy)	$60 \times 60 \mathrm{s}$	R	21.92	0.24	This work
		$90 \times 60 \mathrm{s}$	R	>23.02		This work
235.750	CMOS/AZT-33IK (Mondy)	90 X 00 S	1	>23.02		THIS WOLK
35.750 59.086	CMOS/AZT-33IK (Mondy) CMOS/AZT-33IK (Mondy)	$90 \times 60 \text{ s}$ $114 \times 60 \text{ s}$	R R	>23.92		This work This work

Table A1 - continued

$T-T_0$ (h)	Instrument/Telescope	Exp. Time	Filter	Mag	Mag err	Source
308.135	CMOS/AZT-33IK (Mondy)	$120 \times 60 \mathrm{s}$	R	>23.82		This work
379.454	CMOS/AZT-33IK (Mondy)	$150 \times 60 \mathrm{s}$	R	>23.72		This work
450.107	CMOS/AZT-33IK (Mondy)	$142 \times 60 \mathrm{s}$	R	>23.31		This work
476.372	CMOS/AZT-33IK (Mondy)	$150 \times 60 \mathrm{s}$	R	>23.39		This work
	•	GRB 240619A ($T_0 = 2$	2460480.65522)	; GOTO24cvn		
2.532	ATLAS	30 s	0	16.242	0.014	ATLAS FP
4.689	GOTO-S	$3 \times 90 \mathrm{s}$	L	17.171	0.170	This work
17.955	GOTO-N	$4 \times 90 \mathrm{s}$	L	18.381	0.086	This work
26.705	ATLAS	30 s	0	18.724	0.125	ATLAS FP
48.010	WINTER/1m Palomar	$30 \times 120 \mathrm{s}$	J	19.3	_	G. Mo et al. (2023)
48.810	UVOT/Swift	81.3 s	v	>18.78		This work
48.684	UVOT/Swift	628 s	white	20.64	0.10	This work
49.174	UVOT/Swift	1070.9 s	и	20.29	0.14	This work
66.054	ALFOSC/NOT	$5 \times 300 \mathrm{s}$	r'	19.489	0.030	This work
65.482	ALFOSC/NOT	$9 \times 200 \mathrm{s}$	z'	20.01	0.04	This work
98.758	PS1-GPC1	300 s	i	20.86	0.28	TNS, 215607
113.909	ALFOSC/NOT	$5 \times 300 \mathrm{s}$	r'	20.452	0.037	This work
161.494	ALFOSC/NOT	$5 \times 300 \mathrm{s}$	r'	20.681	0.051	This work
331.618	X-shooter/VLT	$10 \times 10 \mathrm{s}$	r'	21.705	0.101	This work
551.010	TI SHOOLET, I EI	GRB 240910A (T_0 =			0.101	11110 110111
9.430	GOTO-S	$4 \times 90 \mathrm{s}$	L	19.329	0.130	This work
10.559	GOTO-S	$4 \times 90 \mathrm{s}$	L	19.879	0.152	This work
10.885	GOTO-S	$3 \times 90 \text{ s}$	$\stackrel{L}{L}$	20.161	0.243	This work
11.689	GOTO-S	$4 \times 90 \mathrm{s}$	L	19.970	0.320	This work
12.014	GOTO-S	$4 \times 90 \text{ s}$ $4 \times 90 \text{ s}$	$\stackrel{L}{L}$	19.740	0.123	This work This work
36.613	UVOT/Swift	1561.5 s	u	21.59	0.123	This work This work
36.758	UVOT/Swift	378.7 s	v	>20.08	0.16	This work
37.344	ALT/100C	$10 \times 300 \mathrm{s}$		20.8	0.2	This work
43.504	ALFOSC/NOT	$3 \times 300 \mathrm{s}$	$rac{r}{r'}$	20.985	0.247	This work
				21.12		This work
45.428	IO:O/LT	$6 \times 180 \mathrm{s}$	r		0.13	
45.908	IO:O/LT	$6 \times 180 \mathrm{s}$	z ·	20.76	0.09	This work
46.148	IO:O/LT	$6 \times 180 \mathrm{s}$	i ,	21.09	0.10	This work
47.066	OSIRIS/GTC	30 s	r'	21.156	0.028	This work
57.841	VT/SVOM		R	21.50	0.05	SVOM/VT Team et al.
			-	22.24	0.05	(2024)
57.841	VT/SVOM		B	22.24	0.07	SVOM/VT Team et al.
						(2024)
84.022	UVOT/Swift	670.8 s	и	>22.04		This work
84.958	UVOT/Swift	1758.4 s	v	>20.96		This work
91.237	UVOT/Swift	315.7 s	и	>21.53		This work
191.928	UVOT/Swift	3313.0 s	и	>22.95		This work
196.643	UVOT/Swift	768.2 s	и	>22.19		This work
386.321	LBC/LBT	900 s	z'	>24.5		This work
386.321	LBC/LBT	900 s	r'	25.99	0.35	This work
		GRB 240916A ($T_0 = 2$	2460569.557581); GOTO24fzn		
7.731	GOTO-S	$4 \times 90 \mathrm{s}$	L	17.801	0.055	This work
12.872	ALT/100C	$4 \times 300 \mathrm{s}$	r	18.60	0.05	This work
17.064	UVOT/Swift	237 s	white	20.93	0.18	This work
17.126	UVOT/Swift	188.2 s	v	19.08	0.31	This work
18.339	UVOT/Swift	1185.6 s	и	21.14	0.24	This work
22.750	X-shooter/VLT	$19 \times 30 \mathrm{s}$	r'	19.437	0.023	This work
42.674	ALFOSC/NOT	$3 \times 300 \mathrm{s}$	r'	20.433	0.035	This work
46.373	X-shooter/VLT	$7 \times 30 \mathrm{s}$	r'	20.627	0.033	This work
60.595	ALT/100C	$6 \times 300 \mathrm{s}$	r	>19.2		This work
84.684	ALT/100B	$8 \times 180 \mathrm{s}$	r	>19.9		This work
101.853	UVOT/Swift	916.3 s	white	>22.60		This work
156.200	UVOT/Swift	1693.2 s	white	>22.92		This work
	- · · · · · · · · · · · · · · · · ·	GRB 241002B ($T_0 = 2$				
3.051	GOTO-S	$4 \times 90 \text{ s}$	L	19.53	0.09	This work
6.206	QHY600 CMOS/40cm	500 s	g	20.18	0.3	M. Torreiro Martínez et al
0.200	LCOGT	500 8	8	20.10	0.5	(2024)
6.348	QHY600 CMOS/40cm	500 s	r	19.90	0.25	M. Torreiro Martínez et al
0.570	LCOGT	2008	,	17.70	0.23	(2024)
16			ī	20.0	0.2	' '
16	1.8m PRIME		J	20.0	0.2	J. Durbak et al. (2024a)

Table A1 - continued

$T-T_0$ (h)	Instrument/Telescope	Exp. Time	Filter	Mag	Mag err	Source
16	1.8m PRIME		Н	19.6	0.1	J. Durbak et al. (2024a)
38.986	UVOT/Swift	2619.0 s	и	21.99	0.18	This work
40	1.8m PRIME		J	20.6	0.2	J. Durbak et al. (2024b)
40	1.8m PRIME		H	20.3	0.1	J. Durbak et al. (2024b)
64	1.8m PRIME		H	20.8	0.2	O. Guiffreda et al. (2024)
172.080	UVOT/Swift	4302.1 s	и	>23.17		This work
		GRB 241228B ($T_0 = 2$	2460672.67575)	; GOTO24jmz		
0.322	GOTO-N	$4 \times 90 \mathrm{s}$	L	14.543	0.007	This work
0.349	GOTO-N	$4 \times 90 \mathrm{s}$	L	14.647	0.008	This work
0.377	GOTO-N	$4 \times 90 \mathrm{s}$	L	14.713	0.008	This work
0.405	GOTO-N	$4 \times 90 \mathrm{s}$	L	14.778	0.009	This work
1.483	GOTO-N	$4 \times 90 \mathrm{s}$	L	17.001	0.045	This work
5.420	1m LCOGT	600 s	r'	18.62	0.06	I. Ortega-Casas et al. (2024)
5.899	1m LCOGT	600 s	i'	18.31	0.09	I. Ortega-Casas et al. (2024)
6.095	1m LCOGT	600 s	g'	19.40	0.06	I. Ortega-Casas et al. (2024)
6.609	1m LCOGT	600 s	z'	18.25	0.28	I. Ortega-Casas et al. (2024)
7.602	ATLAS	30 s	0	18.861	0.057	ATLAS FP
8.664	0.7m TRT/SBO	$4 \times 300 \mathrm{s}$	R	19.41	0.04	This work
8.794	GOTO-S	$4 \times 90 \mathrm{s}$	L	19.702	0.099	This work
9.957	1m LCOGT	600 s	r'	19.62	0.05	I. Ortega-Casas et al. (2024)
10.976	1m LCOGT	1200 s	B	21.35	0.03	A. Ghosh et al. (2024)
11.362	UVOT/Swift	1778.5 s	и	21.98	0.33	This work
11.628	1.6m Mephisto	$300 \times 4 \mathrm{s}$	u_m	21.69	0.17	This work
11.628	1.6m Mephisto	$300 \times 4 \mathrm{s}$	g_m	20.36	0.08	This work
11.629	1.6m Mephisto	$300 \times 4 \mathrm{s}$	i_m	19.41	0.05	This work
14.175	1.6m Mephisto	$300 \times 3 \mathrm{s}$	v_m	21.71	0.22	This work
14.175	1.6m Mephisto	$300 \times 3 \mathrm{s}$	r_m	20.27	0.05	This work
14.212	1.6m Mephisto	$300 \times 2 \mathrm{s}$	i_m	20.30	0.24	This work
15.739	1.6m Mephisto	$300 \times 3 \mathrm{s}$	v_m	21.70	0.23	This work
15.739	1.6m Mephisto	$300 \times 3 \mathrm{s}$	r_m	20.42	0.07	This work
15.740	1.6m Mephisto	$300 \times 3 \mathrm{s}$	i_m	20.10	0.06	This work
15.991	CMOS/AZT-33IK (Mondy)	$30 \times 120 \mathrm{s}$	R	20.49	0.04	This work
18	D50	$24 \times 120 \mathrm{s}$	r'	20.4	0.1	J. Strobl & M. Jelinek
						(2024)
18.469	1.6m Mephisto	$300 \times 3 \mathrm{s}$	v_m	21.38	0.23	This work
18.469	1.6m Mephisto	$300 \times 3 \mathrm{s}$	r_m	20.54	0.08	This work
18.469	1.6m Mephisto	$300 \times 3 \mathrm{s}$	i_m	20.35	0.10	This work
20.327	ALFOSC/NOT	$2 \times 150 \mathrm{s}$	r'	20.560	0.061	This work
25.591	X-shooter/VLT	10 s	r'	20.626	0.029	This work
25.640	X-shooter/VLT	$3 \times 60 \mathrm{s}$	r'	20.617	0.032	This work
25.688	X-shooter/VLT	$3 \times 60 \mathrm{s}$	g'	21.448	0.011	This work
25.775	X-shooter/VLT	$3 \times 60 \mathrm{s}$	z'	20.267	0.023	This work
33.933	GOTO-S	$4 \times 45 \mathrm{s}$	$\stackrel{\circ}{L}$	>20.52		This work
39.066	1.6m Mephisto	$300 \times 4 \mathrm{s}$	v_m	>22.85		This work
39.066	1.6m Mephisto	$300 \times 4 \mathrm{s}$	r_m	21.02	0.09	This work
39.068	1.6m Mephisto	$300 \times 4 \text{ s}$	i_m	20.72	0.10	This work
41.972	1.6m Mephisto	$300 \times 5 \mathrm{s}$	v_m	>22.80	0.10	This work
41.972	1.6m Mephisto	$300 \times 5 \mathrm{s}$	r_m	21.24	0.11	This work
41.972	1.6m Mephisto	300×3 s	i_m	20.94	0.14	This work
42.175	Zeiss-1000 (SAO RAS)	$12 \times 300 \mathrm{s}$	R	21.18	0.06	A. S. Moskvitin et al.
	,					(2024c)
61.619	1.3m DFOT	$24 \times 300 \mathrm{s}$	R	21.44	0.05	A. K. Ror et al. (2025)
63.023	1.6m Mephisto	$300 \times 4 \mathrm{s}$	v_m	>22.42		This work
63.023	1.6m Mephisto	$300 \times 4 \mathrm{s}$	r_m	21.87	0.15	This work
63.025	1.6m Mephisto	$300 \times 4 \mathrm{s}$	i_m	21.50	0.14	This work
66.200	1.6m Mephisto	$300 \times 4 \mathrm{s}$	v_m	>22.74		This work
66.200	1.6m Mephisto	$300 \times 4 \mathrm{s}$	r_m	22.49	0.19	This work
66.203	1.6m Mephisto	$300 \times 4 \mathrm{s}$	i_m	21.92	0.19	This work
87.254	1.6m Mephisto	$300 \times 5 \mathrm{s}$	v_m	>22.81		This work
87.254	1.6m Mephisto	$300 \times 5 \mathrm{s}$	r_m	22.70	0.20	This work
87.254	1.6m Mephisto	$300 \times 5 \mathrm{s}$	i_m	>23.40		This work
204.161	UVOT/Swift	4273.9 s	и	>22.59		This work

Table A2. Log of radio follow-up observations. The flux density errors are 1 sigma and the upper limits correspond to three times the image RMS.

Observation date	Telescope	Time post-burst	Frequency	Flux density	Source
(UTC)		(d)	(GHz)	(μ J y)	
		GRB 240	0122A		
2024-01-24 12:01:00.0 UT	ATCA	2.06	5.5	<159.2	G. E. Anderson et al. (2024b)
	ATCA		9.0	160.0 ± 20.0	G. E. Anderson et al. (2024b)
2024-01-26 06:39:24.9 UT	ATCA	3.84	5.5	<1555.0	This work
	ATCA		9.0	<100.5	This work
	ATCA		16.7	<113.1	This work
	ATCA		21.2	<333.0	This work
2024-01-28 10:37:34.9 UT	ATCA	6.01	5.5	<174.0	This work
	ATCA		9.0	66.3 ± 19.7	This work
	ATCA		16.7	<55.5	This work
	ATCA		21.2	<111.3	This work
2024-02-12 03:03:54.9 UT	ATCA	20.69	5.5	<45.0	This work
	ATCA		9.0	<33.6	This work
		GRB 240	0619A		
2024-06-22 13:45:34 UT	AMI-LA	3.42	15.5	1500 ± 60	L. Rhodes et al. (2024)
		GRB 240	0910A		
2024-09-13 06:34:25.6 UT	VLA	3.11	6	137 ± 10	S. Giarratana et al. (2024a)
2024-09-13 06:56:22.1 UT	VLA	3.12	10	114 ± 9	S. Giarratana et al. (2024a)
2024-09-13 06:16:03.7 UT	VLA	3.09	15	86 ± 10	S. Giarratana et al. (2024a)
2024-09-19 06:33:15.8 UT	VLA	9.10	6	58 ± 7	This work
2024-09-19 06:54:57.2 UT	VLA	9.12	10	47 ± 8	This work
2024-09-19 06:14:53.8 UT	VLA	9.09	15	71 ± 10	This work
2024-10-01 11:12:12.0 UT	VLA	21.30	6	22 ± 6	This work
2024-10-01 11:34:09.0 UT	VLA	21.31	10	<24	This work
2024-10-01 10:53:51.0 UT	VLA	21.29	15	<27	This work
2024-10-26 09:15:46.0 UT	VLA	46.22	6	<18	This work
2024-10-26 09:38:12.0 UT	VLA	46.23	10	<27	This work
2024-10-26 08:55:00.0 UT	VLA	46.20	15	<18	This work
		GRB 240	0916A		
2024-09-18 00:43:57 UT	VLA	1.97	6	35 ± 8	S. Giarratana et al. (2024b)
	VLA		10	44 ± 8	S. Giarratana et al. (2024b)
	VLA		15	135 ± 8	S. Giarratana et al. (2024b)

Table A3. Absorption features identified in the afterglow spectrum of GRB 240122A ($z=3.1634\pm0.0003$), based on observations with VLT/X-shooter and GTC/OSIRIS. The UVB, VIS, and NIR designations refer to the respective arms of the VLT/X-shooter spectrograph.

λ _{obs} (Å)	λ_{rest} (Å)	Feature	Type	Arm
3796.2	911.8	Ly limit	abs	UVB
5061.6	1215.7	Lyα	abs	UVB
5247.9	1260.4	Si II	abs	UVB
5556.5	1334.5	Сп	abs	UVB
5803.1	1393.8	Si IV	abs	VIS
5840.6	1402.8	Si IV	abs	VIS
6356.6	1526.7	Si II	abs	VIS
6446.1	1548.2	CIV	abs	VIS
6456.8	1550.8	Cıv	abs	VIS
6956.5	1670.8	Al II	abs	VIS
11642.9	2796.4	Mg II	abs	NIR
11672.8	2803.5	Mg II	abs	NIR

Table A4. Absorption and emission features identified in the afterglow spectrum of GRB 240225B ($z=0.9462\pm0.0002$), obtained with VLT/X-shooter.

$\lambda_{obs} \ (\mathring{A})$	$\lambda_{rest} \ (\mathring{A})$	Feature	Type	Arm
3610.2	1854.7	Al III	abs	UVB
3625.9	1862.8	Al III	abs	UVB
4002.5	2056.3	Cr II	abs	UVB
4379.4	2249.9	Fe II	abs	UVB
4563.0	2344.2	Fe II	abs	UVB
4621.9	2374.5	Fe II	abs	UVB
4638.1	2382.8	Fe II	abs	UVB
4650.9	2389.4	Fe II*	abs	UVB
4664.5	2396.4	Fe II*	abs	UVB
4671.6	2400.0	Fe II*	abs	UVB
5015.9	2576.9	Mn II	abs	UVB
5034.9	2586.6	Fe II	abs	UVB
5050.2	2594.5	Mn II	abs	UVB
5061.2	2600.2	Fe II	abs	UVB
5443.1	2796.4	Mg II	abs	UVB
5457.1	2803.5	Mg II	abs	UVB
5553.4	2853.0	Mg I	abs	UVB
7254.8	3727.1	[O II]	em	VIS
7260.2	3729.9	[O II]	em	VIS
7659.0 ^a	3934.8	Ca II	abs	VIS
7726.8	3969.6	Ca II	abs	VIS
9748.5	5008.2	[OIII]	em	VIS

Table A5. Absorption and emission features identified in the afterglow spectrum of GRB 240619A ($z=0.3960\pm0.0001$), obtained with VLT/X-shooter. Here, ^a marks lines affected by telluric absorption.

λ _{obs} (Å)	λ _{rest} (Å)	Feature	Туре	Arm
5203.0	3727.1	[O II]	em	UVB
5206.9	3729.9	[O II]	em	UVB
5402.7	3870.2	[Ne III]	em	UVB
6061.0	4341.7	Нγ	em	VIS
6788.3	4862.7	$H\beta$	em	VIS
6924.6^{a}	4960.3	[O III]	em	VIS
6991.5	5008.2	[O III]	em	VIS
9164.2	6564.6	Ηα	em	VIS

Table A6. Absorption features identified in the afterglow spectrum of GRB 240910A ($z=1.4605\pm0.0007$), obtained with GTC/OSIRIS. Here, ^a marks lines affected by telluric absorption.

3808.4 1548.2 C IV abs 3956.8 1608.5 Fe II abs 3967.3 1612.8 Fe II* abs 4110.0 1670.8 Al II abs 4447.5 1808.0 Si II abs 4562.4 1854.7 Al III abs 4984.5 2026.3 Cr II abs 5058.3 2056.3 Cr II abs 5058.6 2066.2 Cr II abs 5328.6 2166.2 Ni II* abs 4563.4 2185.6 Mn I abs 5669.1 2316.8 Ni II* abs 5766.5 2344.2 Fe II abs 5861.4 2382.8 Fe II abs 5894.7 2396.3 Fe II* abs 6338.9° 2576.9 Mn II abs 6363.0° 2586.7 Fe II abs 6368.6 2796.3 Mg II abs 6896.3 2803.5 Mg II abs 6896.3	λ _{obs} (Å)	λ_{rest} (Å)	Feature	Type
3956.8 1608.5 Fe II abs 3967.3 1612.8 Fe II* abs 4110.0 1670.8 Al II abs 4447.5 1808.0 Si II abs 4562.4 1854.7 Al III abs 4984.5 2026.3 Cr II abs 5058.3 2056.3 Cr II abs 5082.6 2066.2 Cr II abs 5328.6 2166.2 Ni II* abs 5376.4 2185.6 Mn I abs 5561.3 2260.8 Fe II abs 5699.1 2316.8 Ni II* abs 5766.5 2344.2 Fe II abs 5841.0 2374.5 Fe II abs 5861.4 2382.8 Fe II abs 5894.7 2396.3 Fe II* abs 6338.9a 2576.9 Mn II abs 6338.9a 2576.9 Mn II abs 6363.0a 2586.7 Fe II abs 6396.2a 2600.2 Fe II abs 6878.6 2796.3 Mg II abs 6886.3 2803.5 Mg II abs	3755.5	1526.7	Si II	abs
3967.3 1612.8 Fe II* abs 4110.0 1670.8 Al II abs 4447.5 1808.0 Si II abs 4562.4 1854.7 Al III abs 5058.3 2026.3 Cr II abs 5082.6 2066.2 Cr II abs 5328.6 2166.2 Ni II* abs 5376.4 2185.6 Mn I abs 5699.1 2316.8 Ni II* abs 5766.5 2344.2 Fe II abs 5841.0 2374.5 Fe II abs 5861.4 2382.8 Fe II abs 6338.9a 2576.9 Mn II abs 6338.9a 2576.9 Mn II abs 6363.0a 2586.7 Fe II abs 66896.3 Le II* Abs Al III Abs Abs Al III Abs Abs Al III Abs Abs Abs Ab III* Abs	3808.4	1548.2	CIV	abs
4110.0 1670.8 Al II abs 4447.5 1808.0 Si II abs 4562.4 1854.7 Al III abs 4984.5 2026.3 Cr II abs 5058.3 2056.3 Cr II abs 5082.6 2066.2 Cr II abs 5328.6 2166.2 Ni II* abs 5376.4 2185.6 Mn I abs 5561.3 2260.8 Fe II abs 5699.1 2316.8 Ni II* abs 5766.5 2344.2 Fe II abs 5841.0 2374.5 Fe II abs 5861.4 2382.8 Fe II abs 5894.7 2396.3 Fe II* abs 6338.9a 2576.9 Mn II abs 6338.9a 2576.9 Mn II abs 6363.0a 2586.7 Fe II abs 6396.2a 2600.2 Fe II abs 6896.3 2803.5 Mg II abs	3956.8	1608.5	Fe II	abs
4447.5 1808.0 Si II abs 4562.4 1854.7 Al III abs 4984.5 2026.3 Cr II abs 5058.3 2056.3 Cr II abs 5082.6 2066.2 Cr II abs 5328.6 2166.2 Ni II* abs 5376.4 2185.6 Mn I abs 5561.3 2260.8 Fe II abs 5699.1 2316.8 Ni II* abs 5766.5 2344.2 Fe II abs 5841.0 2374.5 Fe II abs 5861.4 2382.8 Fe II abs 6338.9a 2576.9 Mn II abs 6338.9a 2576.9 Mn II abs 6363.0a 2586.7 Fe II abs 6396.2a 2600.2 Fe II abs 6878.6 2796.3 Mg II abs 6896.3 2803.5 Mg II abs	3967.3	1612.8	Fe II*	abs
4562.4 1854.7 Al III abs 4984.5 2026.3 Cr II abs 5058.3 2056.3 Cr II abs 5082.6 2066.2 Cr II abs 5328.6 2166.2 Ni II* abs 5376.4 2185.6 Mn I abs 5561.3 2260.8 Fe II abs 5699.1 2316.8 Ni II* abs 5766.5 2344.2 Fe II abs 5841.0 2374.5 Fe II abs 5861.4 2382.8 Fe II abs 5894.7 2396.3 Fe II* abs 6338.9a 2576.9 Mn II abs 6338.9a 2576.9 Mn II abs 6363.0a 2586.7 Fe II abs 6396.2a 2600.2 Fe II abs 6896.3 2803.5 Mg II abs	4110.0	1670.8	Alπ	abs
4984.5 2026.3 Cr II abs 5058.3 2056.3 Cr II abs 5082.6 2066.2 Cr II abs 5328.6 2166.2 Ni II* abs 5376.4 2185.6 Mn I abs 5561.3 2260.8 Fe II abs 5699.1 2316.8 Ni II* abs 5766.5 2344.2 Fe II abs 5841.0 2374.5 Fe II abs 5861.4 2382.8 Fe II abs 5894.7 2396.3 Fe II* abs 6338.9a 2576.9 Mn II abs 6363.0a 2586.7 Fe II abs 6396.2a 2600.2 Fe II abs 6878.6 2796.3 Mg II abs	4447.5	1808.0	Si II	abs
5058.3 2056.3 Cr II abs 5082.6 2066.2 Cr II abs 5328.6 2166.2 Ni II* abs 5376.4 2185.6 Mn I abs 5561.3 2260.8 Fe II abs 5699.1 2316.8 Ni II* abs 5766.5 2344.2 Fe II abs 5841.0 2374.5 Fe II abs 5861.4 2382.8 Fe II abs 6338.9a 2576.9 Mn II abs 6338.9a 2576.9 Mn II abs 6396.2a 2600.2 Fe II abs 6878.6 2796.3 Mg II abs 6896.3 2803.5 Mg II abs	4562.4	1854.7	Al III	abs
$\begin{array}{cccccccccccccccccccccccccccccccccccc$	4984.5	2026.3	Cr II	abs
$\begin{array}{cccccccccccccccccccccccccccccccccccc$	5058.3	2056.3	Cr II	abs
$\begin{array}{cccccccccccccccccccccccccccccccccccc$	5082.6	2066.2	Cr II	abs
$\begin{array}{cccccccccccccccccccccccccccccccccccc$	5328.6	2166.2	Ni II*	abs
$\begin{array}{cccccccccccccccccccccccccccccccccccc$	5376.4	2185.6	Mn I	abs
$\begin{array}{cccccccccccccccccccccccccccccccccccc$	5561.3	2260.8	Fe II	abs
$\begin{array}{cccccccccccccccccccccccccccccccccccc$	5699.1	2316.8	Ni II*	abs
$\begin{array}{cccccccccccccccccccccccccccccccccccc$	5766.5	2344.2	Fe II	abs
$\begin{array}{cccccccccccccccccccccccccccccccccccc$	5841.0	2374.5	Fe II	abs
$\begin{array}{cccccccccccccccccccccccccccccccccccc$	5861.4	2382.8	Fe II	abs
$\begin{array}{cccccccccccccccccccccccccccccccccccc$	5894.7	2396.3	Fe II*	abs
$\begin{array}{cccccccccccccccccccccccccccccccccccc$	6338.9^{a}	2576.9	Mn II	abs
6878.6 2796.3 Mg II abs 6896.3 2803.5 Mg II abs	6363.0^{a}	2586.7	Fe II	abs
6896.3 2803.5 Mg II abs	6396.2^a	2600.2	Fe II	abs
8	6878.6	2796.3	Mg II	abs
7018.0 2852.7 Mg I abs	6896.3	2803.5	Mg II	abs
	7018.0	2852.7	Mg I	abs

Table A7. Absorption features identified in the afterglow spectrum of GRB 240916A ($z=2.6100\pm0.0002$), obtained with VLT/X-shooter. Superscript symbols indicate excited-state transitions (*, **), while ^a marks lines affected by telluric absorption.

miles affected by tenune absorption.					
λ _{obs} (Å)	λ _{rest} (Å)	Feature	Туре	Arm	
4388.6	1215.7	$Ly\alpha$	abs	UVB	
4513.2	1250.2	SII	abs	UVB	
4524.8	1253.4	SII	abs	UVB	
4546.4	1259.4	SII	abs	UVB	
4566.1	1264.8	Si II*	abs	UVB	
4700.8	1302.2	Oı	abs	UVB	
4708.8	1304.4	Si II	abs	UVB	
4710.5	1304.9	O I*	abs	UVB	
4714.8	1306.0	O I**	abs	UVB	
4726.5	1309.3	Si II*	abs	UVB	
4817.7	1334.5	CII	abs	UVB	
4821.9	1335.7	C II*	abs	UVB	
5031.5	1393.8	Si IV	abs	UVB	
5064.0	1402.8	Si IV	abs	UVB	
5511.4	1526.7	Si 11	abs	UVB	
5535.7	1533.4	Si II*	abs	UVB	
5589.0	1548.2	CIV	abs	VIS	
5598.3	1550.8	CIV	abs	VIS	
5806.5	1608.5	Fe II	abs	VIS	
5822.2	1612.8	Fe II*	abs	VIS	
6031.5	1670.8	Al II	abs	VIS	
6144.2	1702.0	Fe II*	abs	VIS	
6287.0	1741.6	Ni II	abs	VIS	
6526.9	1808.0	Si II	abs	VIS	
6695.5	1854.7	Al III	abs	VIS	
6724.7	1862.8	Al III	abs	VIS	
7315.6	2026.5	Mg I	abs	VIS	
7314.4	2026.1	Zn II	abs	VIS	
7314.9	2026.3	Cr II	abs	VIS	
7423.1	2056.3	Cr II	abs	VIS	
7444.5	2062.2	Cr II	abs	VIS	
7445.4	2062.4	Zn II	abs	VIS	
7459.0	2066.2	Cr II	abs	VIS	
7820.0	2166.2	Ni Ⅱ*	abs	VIS	
8004.1	2217.2	Ni Ⅱ*	abs	VIS	
8027.2	2223.6	Ni Ⅱ*	abs	VIS	
8122.1	2249.9	Fe II	abs	VIS	
8161.5	2260.8	Fe II*	abs	VIS	
8363.3	2316.7	Ni II*	abs	VIS	
8404.4	2328.1	Fe II*	abs	VIS	
8423.9	2333.5	Fe II*	abs	VIS	
8442.7	2338.7	Fe II*	abs	VIS	
8462.6	2344.2	Fe II	abs	VIS	
8479.9	2349.0	Fe II*	abs	VIS	
8539.8	2365.6	Fe II*	abs	VIS	
8571.8	2374.5	Fe II	abs	VIS	
8601.8	2382.8	Fe II	abs	VIS	
8625.6	2389.4	Fe II*	abs	VIS	
8650.8	2396.4	Fe II*	abs	VIS	
8664.0	2400.0	Fe II*	abs	VIS	
8684.2	2405.6	Fe II*	abs	VIS	
8690.7	2407.4	Fe II*	abs	VIS	
8704.8	2411.3	Fe II*	abs	VIS	
8714.9	2414.1	Fe II*	abs	VIS	
9302.5^{a}	2576.9	Mn II	abs	VIS	
9337.8 ^a	2586.6	Fe II	abs	VIS	
9386.6^{a}	2600.2	Fe II	abs	VIS	
9409.3^{a}	2606.5	Mn II	abs	VIS	
9414.5 ^a	2607.9	Fe II*	abs	VIS	

Table A7 - continued

λ _{obs} (Å)	λ _{rest} (Å)	Feature	Type	Arm
9431.8 ^a	2612.7	Fe II*	abs	VIS
9452.4^{a}	2618.4	Fe II*	abs	VIS
9491.1 ^a	2629.1	Fe II*	abs	VIS
9501.3a	2631.9	Fe II*	abs	VIS
10094.8	2796.4	Mg II	abs	VIS
10120.7	2803.5	Mg II	abs	VIS

Table A8. Absorption and emission features identified in the afterglow spectrum of GRB 241228B ($z=2.6745\pm0.0004$), obtained with VLT/X-shooter. Superscript symbols denote excited-state transitions (*, **, etc.), while ^a marks features affected by telluric absorption.

λ _{obs} (Å)	λ _{rest} (Å)	Feature	Type	Arm
4467.0	1215.7	Lyα	abs	UVB
4551.8	1238.8	NV	abs	UVB
4566.5	1242.8	Nv	abs	UVB
4593.7	1250.2	S II	abs	UVB
4605.5	1253.4	S II	abs	UVB
4627.5	1259.4	S II	abs	UVB
4631.2	1260.4	Si II	abs	UVB
4647.6	1264.8	Si II*	abs	UVB
4784.8	1302.2	Oı	abs	UVB
4792.9	1304.4	Si II	abs	UVB
4794.7	1304.9	O I*	abs	UVB
4798.8	1306.0	O I**	abs	UVB
4810.9	1309.3	Si II*	abs	UVB
4839.9	1317.2	Ni II	abs	UVB
4903.1	1334.4	Сп	abs	UVB
4907.9	1335.7	C II*	abs	UVB
5034.3	1370.1	Ni II	abs	UVB
5121.2	1393.8	Si IV	abs	UVB
5154.3	1402.8	Si IV	abs	UVB
5345.5	1454.8	Ni II	abs	UVB
5391.4	1467.3	Ni II	abs	UVB
5393.3	1467.8	Ni II	abs	UVB
5609.7	1526.7	Si II	abs	VIS
5634.3	1533.4	Si II*	abs	VIS
5688.7	1548.2	CIV	abs	VIS
5698.3	1550.8	Cıv	abs	VIS
5728.4	1559.0	Fe II****	abs	VIS
5757.0	1566.8	Fe II*	abs	VIS
5910.1	1608.5	Fe II	abs	VIS
5920.2	1611.2	Fe II	abs	VIS
5926.1	1612.8	Fe II*	abs	VIS
6016.5	1637.4	Fe II*	abs	VIS
6139.0	1670.8	Аl II	abs	VIS
6253.8	1702.0	Fe II*	abs	VIS
6281.8	1709.6	Ni II	abs	VIS
6399.3	1741.6	Ni II	abs	VIS
6437.2	1751.9	Ni II	abs	VIS
6643.3	1808.0	Si II	abs	VIS
6676.0	1816.9	Si II*	abs	VIS
6678.2	1817.5	Si II*	abs	VIS
6716.4	1827.9	MgI	abs	VIS
6814.9	1854.7	Al III	abs	VIS
6844.5	1862.8	Al III	abs	VIS
7444.7	2026.1	Zn II	abs	VIS
7445.4	2026.3	CrII	abs	VIS
7446.2	2026.5	MgI	abs	VIS
7555.7	2056.3	Cr II	abs	VIS
7577.3	2062.2	CrII	abs	VIS
7579.0^{a}	2062.7	Zn II	abs	VIS

Table A8 - continued

λ _{obs} (Å)	$\lambda_{rest} \ (\mathring{A})$	Feature	Type	Arm
7592.0 ^a	2066.2	Cr II	abs	VIS
7959.5	2166.2	Ni Ⅱ*	abs	VIS
8146.9	2217.2	Ni Ⅱ*	abs	VIS
8170.4	2223.6	Ni Ⅱ*	abs	VIS
8267.0	2249.9	Fe II	abs	VIS
8307.1	2260.8	Fe II	abs	VIS
8512.8	2316.8	Ni Ⅱ*	abs	VIS
8554.4	2328.1	Fe II*	abs	VIS
8574.2	2333.5	Fe II*	abs	VIS
8593.3	2338.7	Fe II*	abs	VIS
8613.5	2344.2	Fe II	abs	VIS

Table A9. GRB 241228B (continued).

$\lambda_{obs} \; (\mathring{A})$	$\lambda_{rest} \ (\mathring{A})$	Feature	Type	Arm
8616.5	2345.0	Fe II*	abs	VIS
8631.2	2349.0	Fe II*	abs	VIS
8670.8	2359.8	Fe II*	abs	VIS
8692.2	2365.6	Fe II*	abs	VIS
8724.9	2374.5	Fe II	abs	VIS
8750.6	2381.5	Fe II*	abs	VIS
8755.4	2382.8	Fe II	abs	VIS
8779.6	2389.4	Fe II*	abs	VIS
8805.0	2396.3	Fe II*	abs	VIS
8818.6	2400.0	Fe II*	abs	VIS
8845.8	2407.4	Fe II*	abs	VIS
8859.9	2411.2	Fe II*	abs	VIS
8861.9	2411.8	Fe II*	abs	VIS
9468.6 ^a	2576.9	Mn II	abs	VIS
9504.4 ^a	2586.7	Fe II	abs	VIS
9533.2^{a}	2594.5	Mn II	abs	VIS
9554.2 ^a	2600.2	Fe II	abs	VIS
9577.3 ^a	2606.5	Mn II	abs	VIS
9582.5^{a}	2607.9	Fe II*	abs	VIS
9600.1 ^a	2612.7	Fe II*	abs	VIS
9607.1 ^a	2614.6	Fe II*	abs	VIS
9621.0^{a}	2618.4	Fe II*	abs	VIS
9636.1a	2622.5	Fe II*	abs	VIS
9650.8 ^a	2626.5	Fe 11*	abs	VIS
9660.4^{a}	2629.1	Fe II*	abs	VIS
10274.9	2796.3	Mg II	abs	NIR
10301.2	2803.5	Mg II	abs	NIR
10483.1	2853.0	MgI	abs	NIR
14585.9	3969.6	Сап	abs	NIR
15535.0	4227.9	Caı	abs	NIR

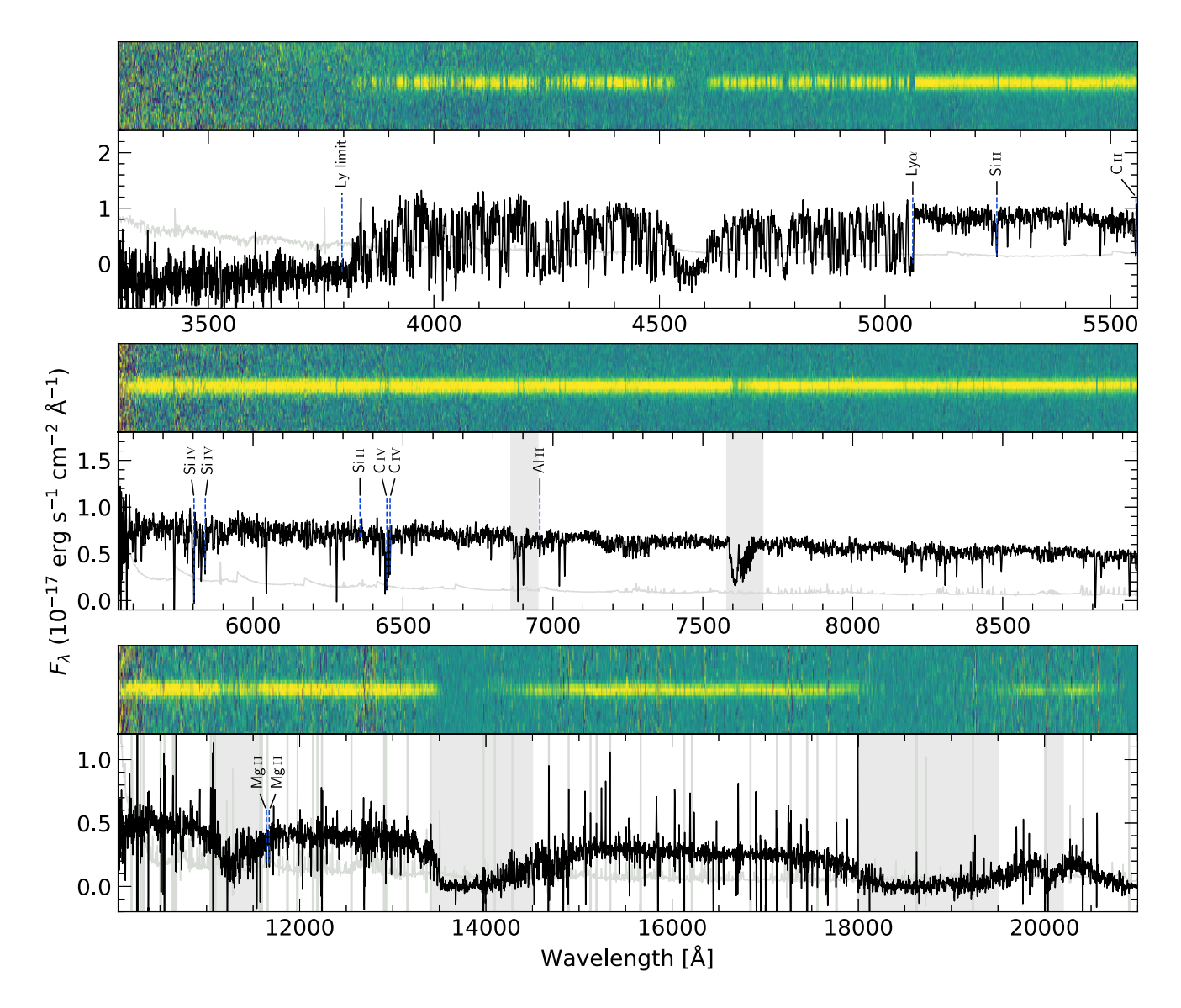


Figure A1. X-shooter spectra of GRB 240122A at $z=3.1634\pm0.0003$, observed at 16.130 h post-trigger. The three panels show the spectra from the UVB, VIS, and NIR arms (top to bottom). Each panel displays the 2D spectrum (upper sub-panel) and the corresponding 1D extracted spectrum in black with the error spectrum in grey (lower sub-panel). Absorption lines identified at the redshift of the GRB are marked in blue and labelled, while grey-shaded regions indicate telluric absorption. The 1D spectra have been smoothed with a Savitzky-Golay filter to enhance the visibility of spectral features. The same colour scheme is adopted for all spectra presented throughout this work.

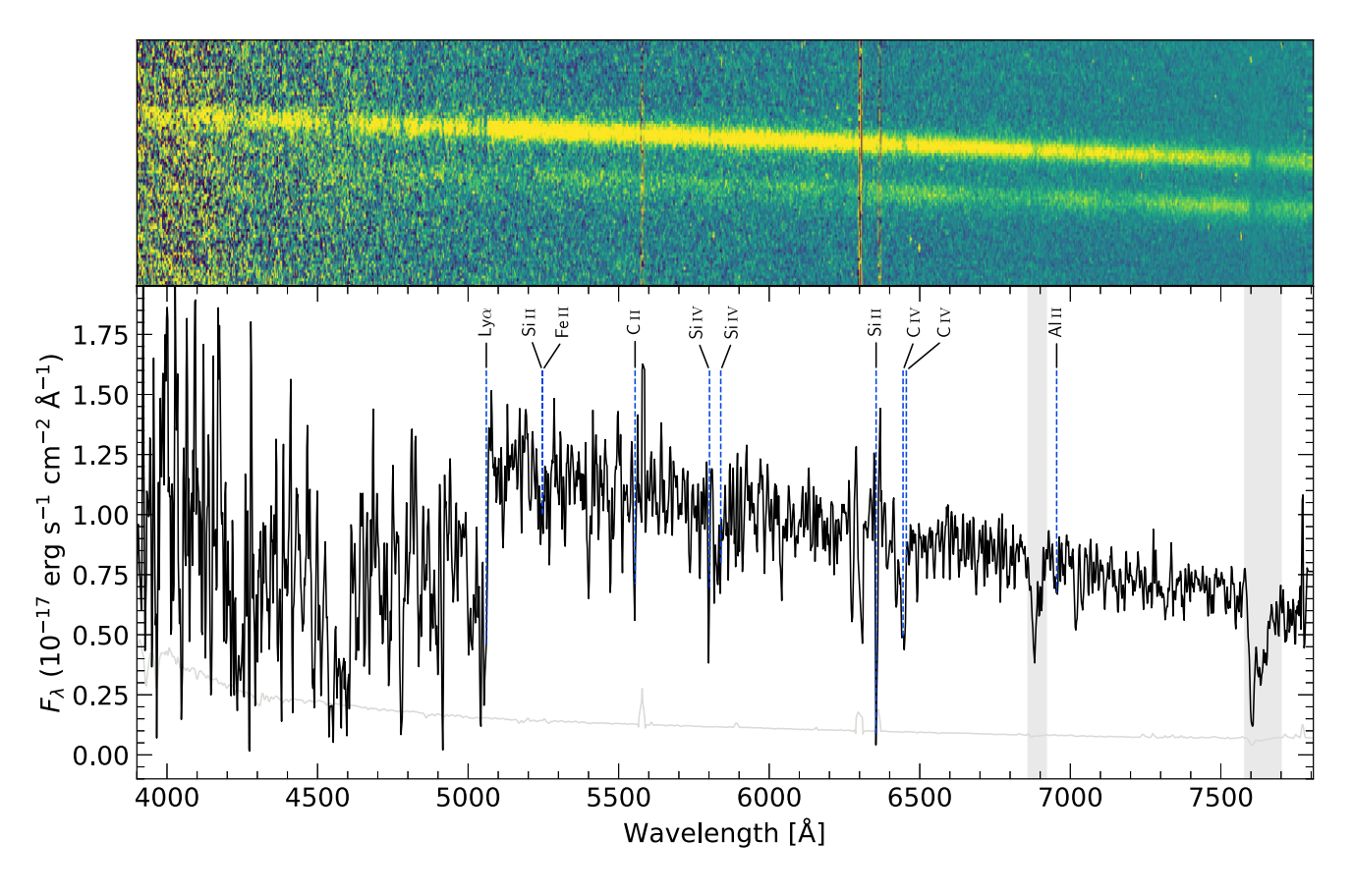


Figure A2. GTC/OSIRIS spectrum of GRB 240122A at $z=3.1634\pm0.0003$, obtained 12.857 h after the trigger. The upper panel displays the 2D spectrum, and the lower panel shows the extracted 1D spectrum in black with its error spectrum in grey. Absorption features at the GRB redshift are highlighted in blue and labelled, while grey-shaded regions mark telluric absorption. The 1D spectra were smoothed using a Savitzky-Golay filter to improve the visibility of spectral features.

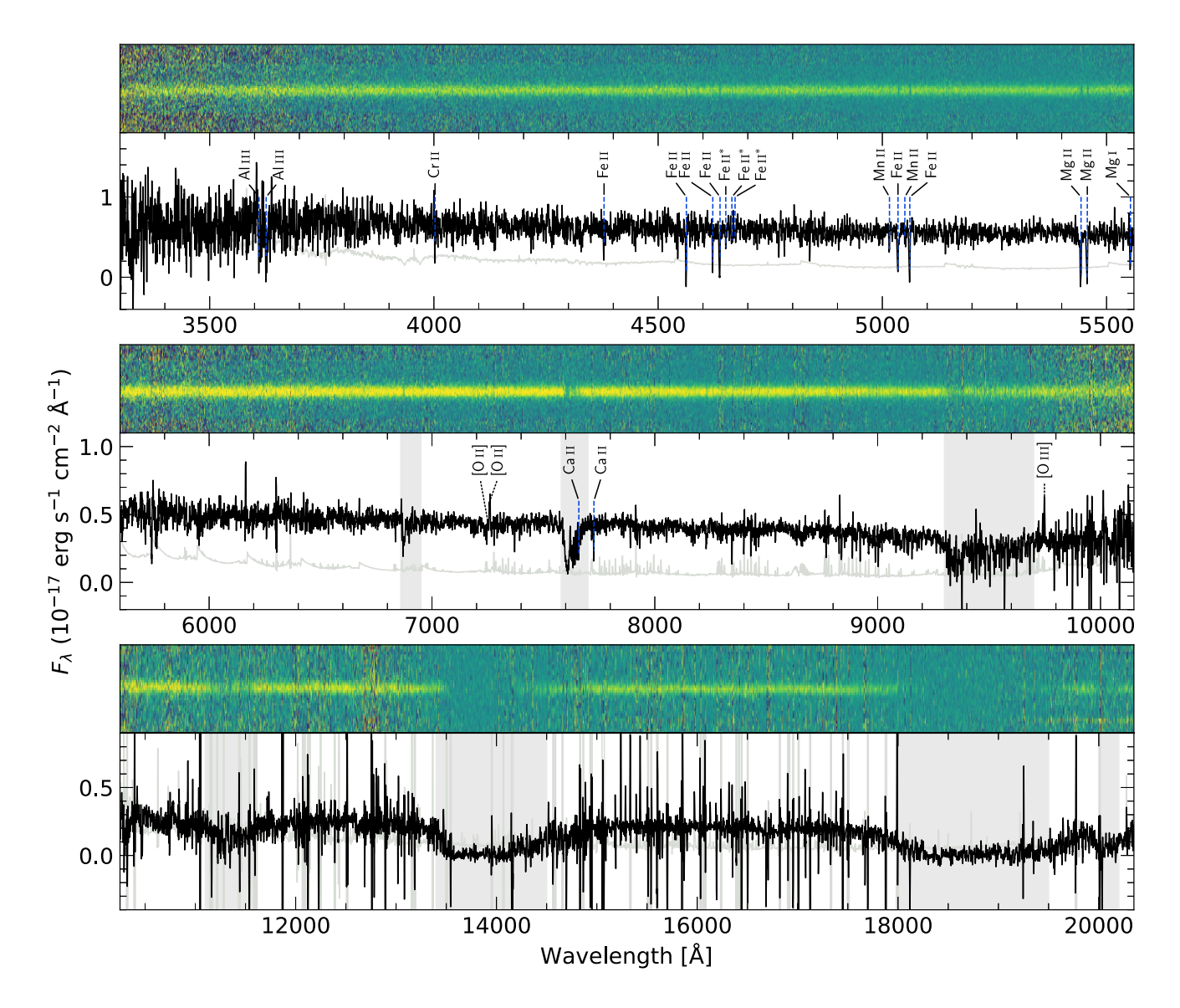


Figure A3. VLT/X-shooter spectra of GRB 240225B at $z=0.9462\pm0.0002$, taken at 3.237 d post-trigger. Absorption lines identified at the GRB redshift are marked in blue and labelled accordingly, while emission lines are indicated by black dotted vertical lines. A Savitzky-Golay filter was applied to the 1D spectra to enhance the clarity of spectral features.

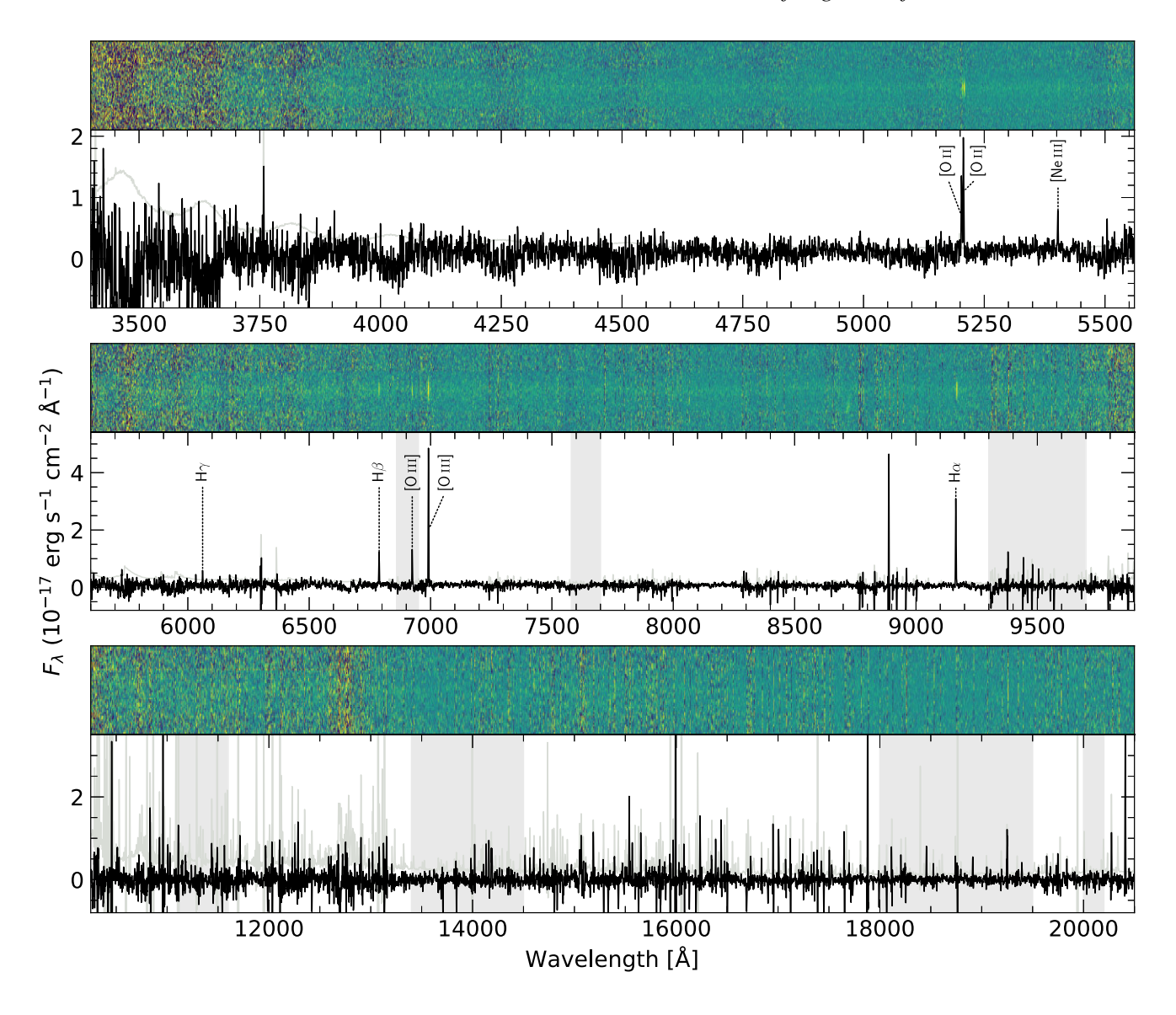


Figure A4. VLT/X-shooter spectra of GRB 240619A at $z=0.3960\pm0.0001$, observed at 13.826 d post-trigger. Emission lines are indicated by black dotted vertical lines and labelled accordingly. To highlight spectral features, the 1D spectra were smoothed with a Savitzky-Golay filter.

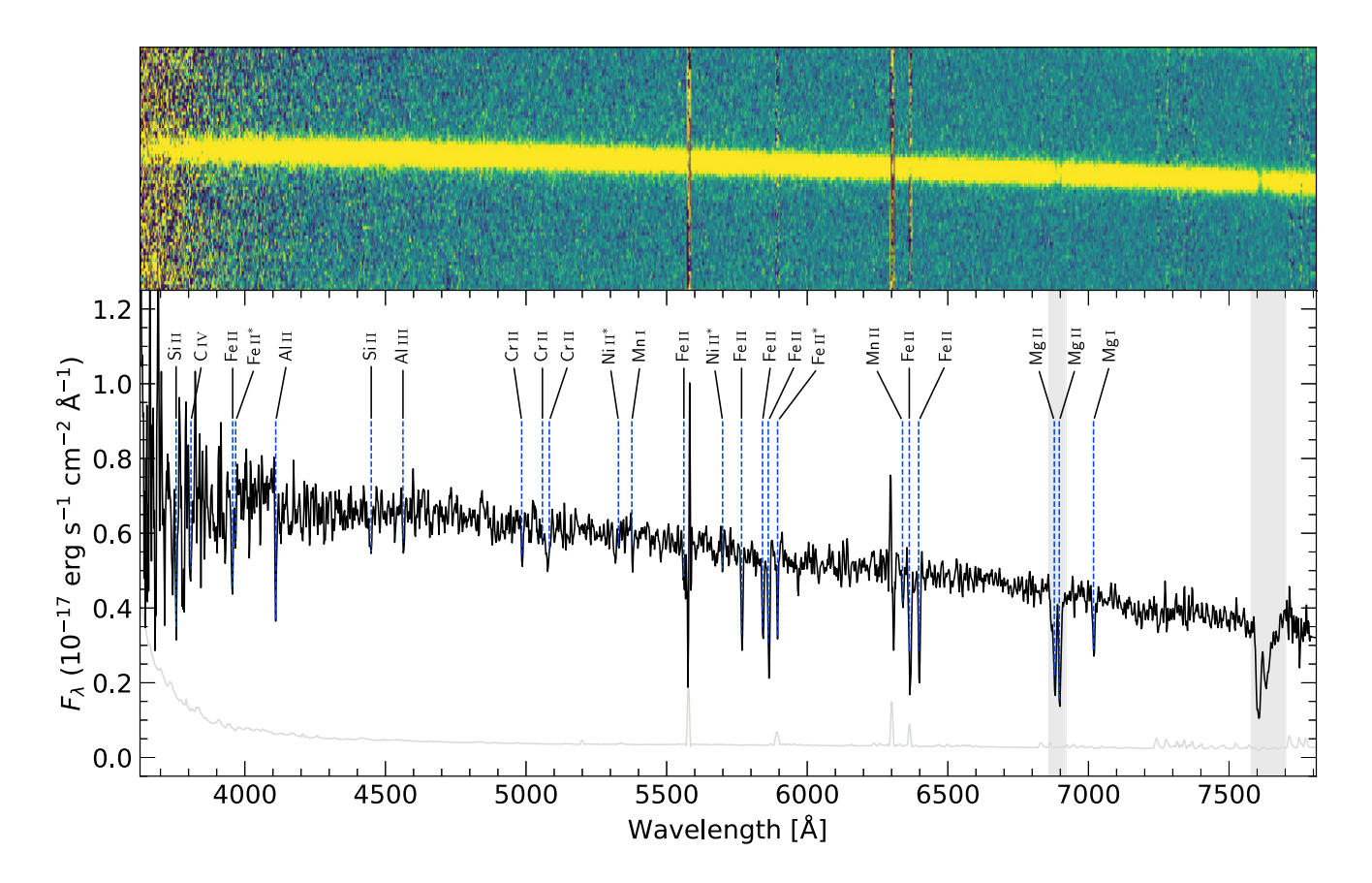


Figure A5. GTC/OSIRIS spectrum of GRB 240910A at $z = 1.4605 \pm 0.0007$ at 1.964 d post-trigger. The upper panel presents the 2D spectrum, while the lower panel shows the extracted 1D spectrum in black with its associated error in grey. Absorption features at the GRB redshift are indicated in blue and labelled, and grey-shaded regions denote telluric absorption. For improved feature visibility, the 1D spectra were smoothed using a Savitzky-Golay filter.

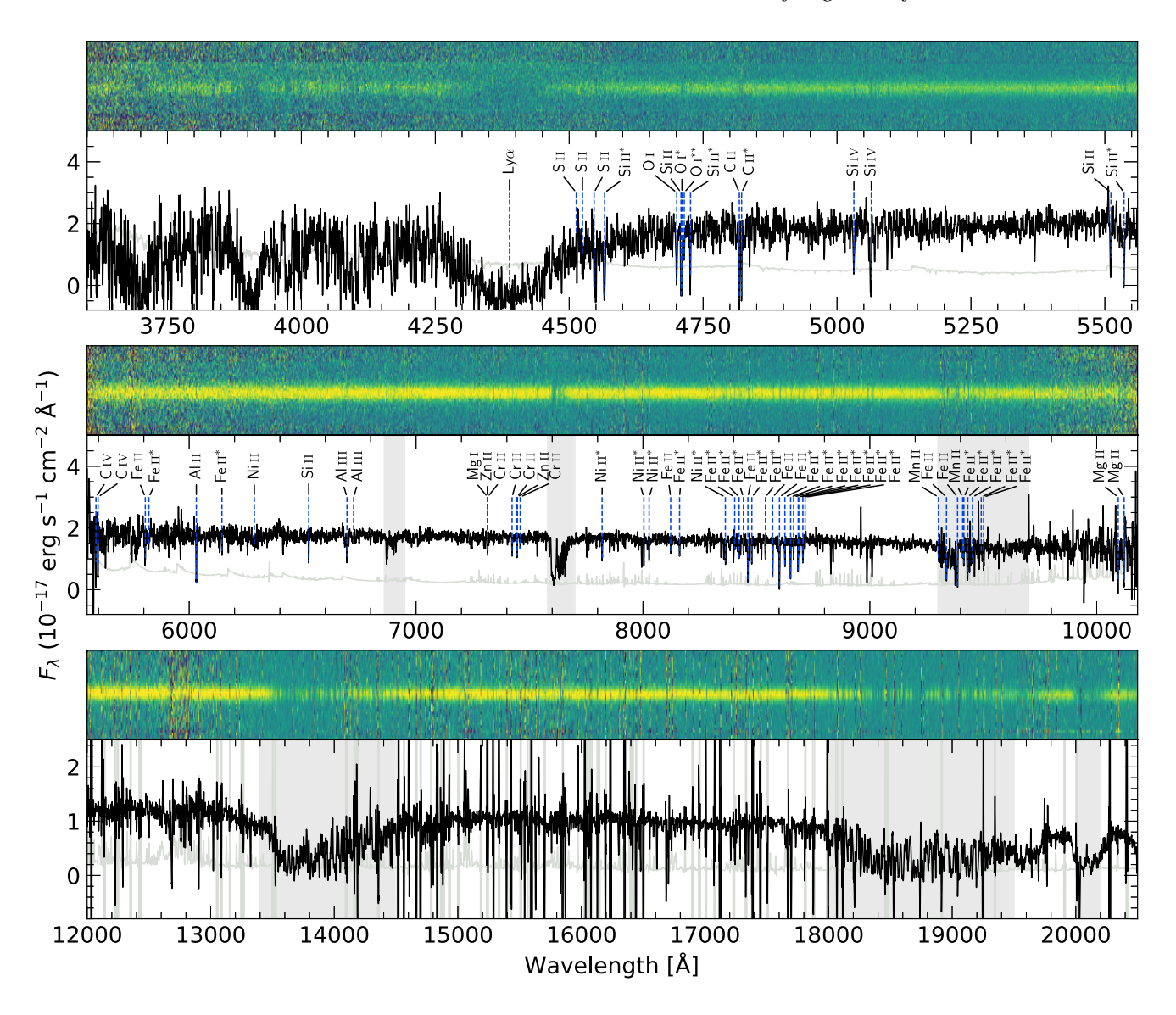


Figure A6. VLT/X-shooter spectra of GRB 240916A at $z = 2.6100 \pm 0.0002$, taken at 22.962 h post-trigger. Absorption lines identified at the redshift of the GRB are marked in blue and labelled accordingly. The 1D spectra were filtered with a Savitzky-Golay function to enhance the prominence of spectral features.

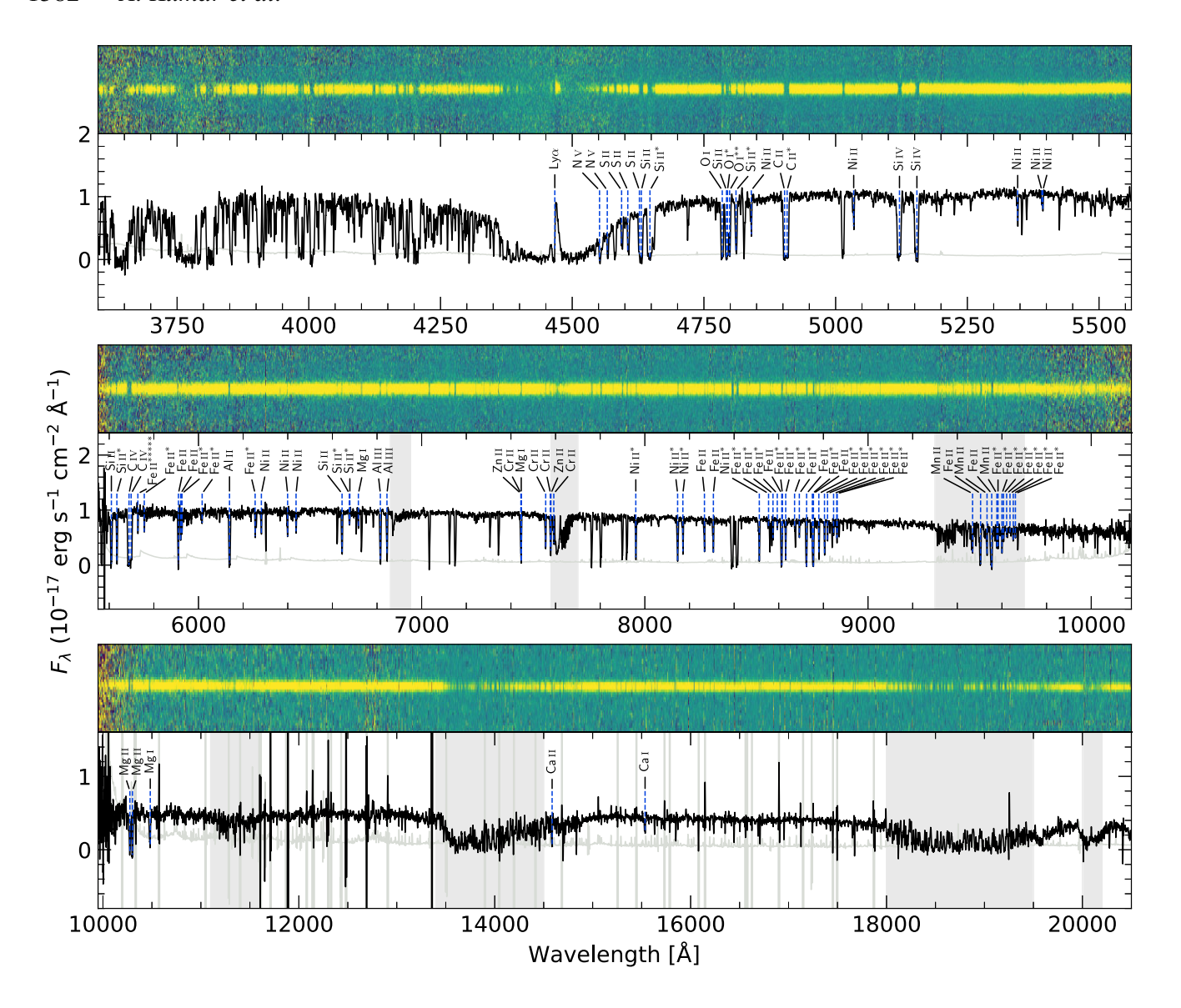


Figure A7. VLT/X-shooter spectra of GRB 241228B at $z=2.6745\pm0.0004$, obtained at 25.975 h post-trigger. Absorption lines identified at the redshift of the GRB are marked in blue and labelled accordingly. The 1D spectra have been smoothed with a Savitzky-Golay filter to enhance the visibility of spectral features.

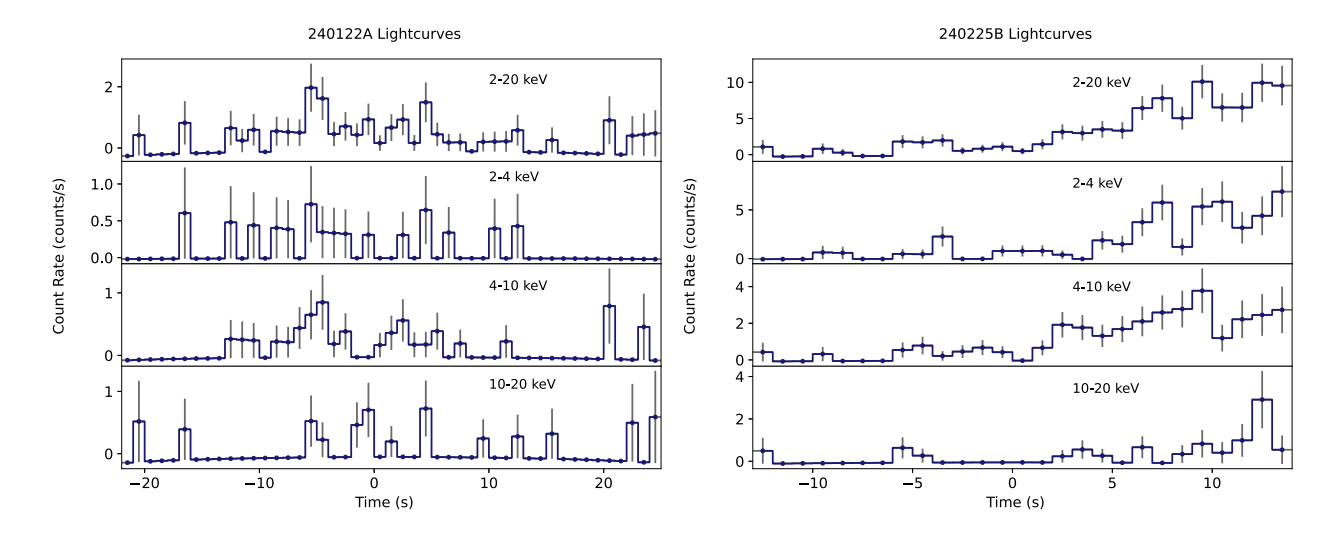


Figure A8. MAXI/GSC light curves for GRBs in our sample (240122A, 240225B) are shown. Data are binned to 1-s resolution.

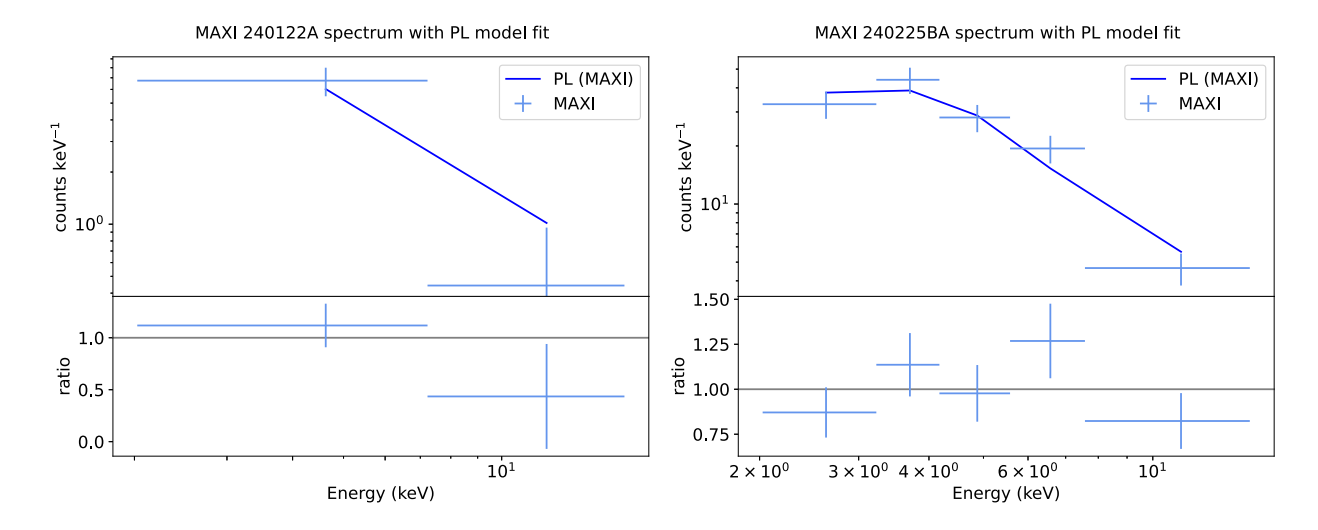


Figure A9. MAXI fitted spectra for GRBs 240122A and 240225B are shown. Models shown are the best-fitting models as described in Table 4.

¹Department of Physics, Royal Holloway – University of London, Egham TW20 0EX, UK

²Department of Physics, University of Warwick, Gibbet Hill Road, Coventry CV4 7AL, UK

³School of Physics and Astronomy, University of Birmingham, Edgbaston, Birmingham B15 2TT, UK

⁴Institute for Gravitational Wave Astronomy, University of Birmingham, Birmingham B15 2TT, UK

⁵Aix Marseille Univ., CNRS, CNES, LAM, Marseille, F-13388, France

⁶School of Physics and Astronomy, Monash University, Clayton, VIC 3800, Australia

⁷ Université Paris-Saclay, Université Paris Cité, CEA, CNRS, AIM, F-91191 Gif-sur-Yvette, France

⁸School of Physics and Astronomy, University of Leicester, University Road, Leicester LE1 7RH, UK

⁹Sydney Institute for Astronomy, School of Physics, The University of Sydney, NSW 2006, Australia

¹⁰Centre of Excellence for Gravitational Wave Discovery (OzGrav), Hawthorn, VIC 3122, Australia

¹¹ CSIRO Space and Astronomy, PO Box 76, Epping, NSW 1710, Australia

¹²The Cosmic Dawn Centre (DAWN), Rådmandsgade 64, DK-2200 København N., Denmark

¹³Niels Bohr Institute, University of Copenhagen, Jagtvej 155, DK-2200 Copenhagen N, Denmark

¹⁴Department of Astrophysics/IMAPP, Radboud University, NL-6525 AJ Nijmegen, the Netherlands

¹⁵Astrophysics Research Cluster, School of Mathematical and Physical Sciences, University of Sheffield, Sheffield S3 7RH, UK

¹⁶ Research Software Engineering, University of Sheffield, Sheffield S1 4DP,

¹⁷INAF Osservatorio Astronomico di Brera, Via E. Bianchi 46, I-23807 Merate, Italy

¹⁸ Department of Physical Science, Aoyama Gakuin University, 5-10-1 Fuchi-

nobe, Chuo-ku, Sagamihara, Kanagawa 252-5258, Japan

19 South-Western Institute for Astronomy Research (SWIFAR), Yunnan Uni-

versity, Kunming, Yunnan 650500, P. R. China
²⁰ Yunnan Key Laboratory of Survey Science, Yunnan University, Kunming

²⁰Yunnan Key Laboratory of Survey Science, Yunnan University, Kunming, Yunnan 650500, P. R. China

 $^{^{21}} National \ Astronomical \ Observatories, \ Chinese \ Academy \ of \ Sciences, \ Beijing \ 100101, \ China$

²²Guangxi Key Laboratory for Relativistic Astrophysics, School of Physical Science and Technology, Guangxi University, Nanning 530004, China

²³Armagh Observatory and Planetarium, College Hill, Armagh BT61 9DG, Northern Ireland, UK

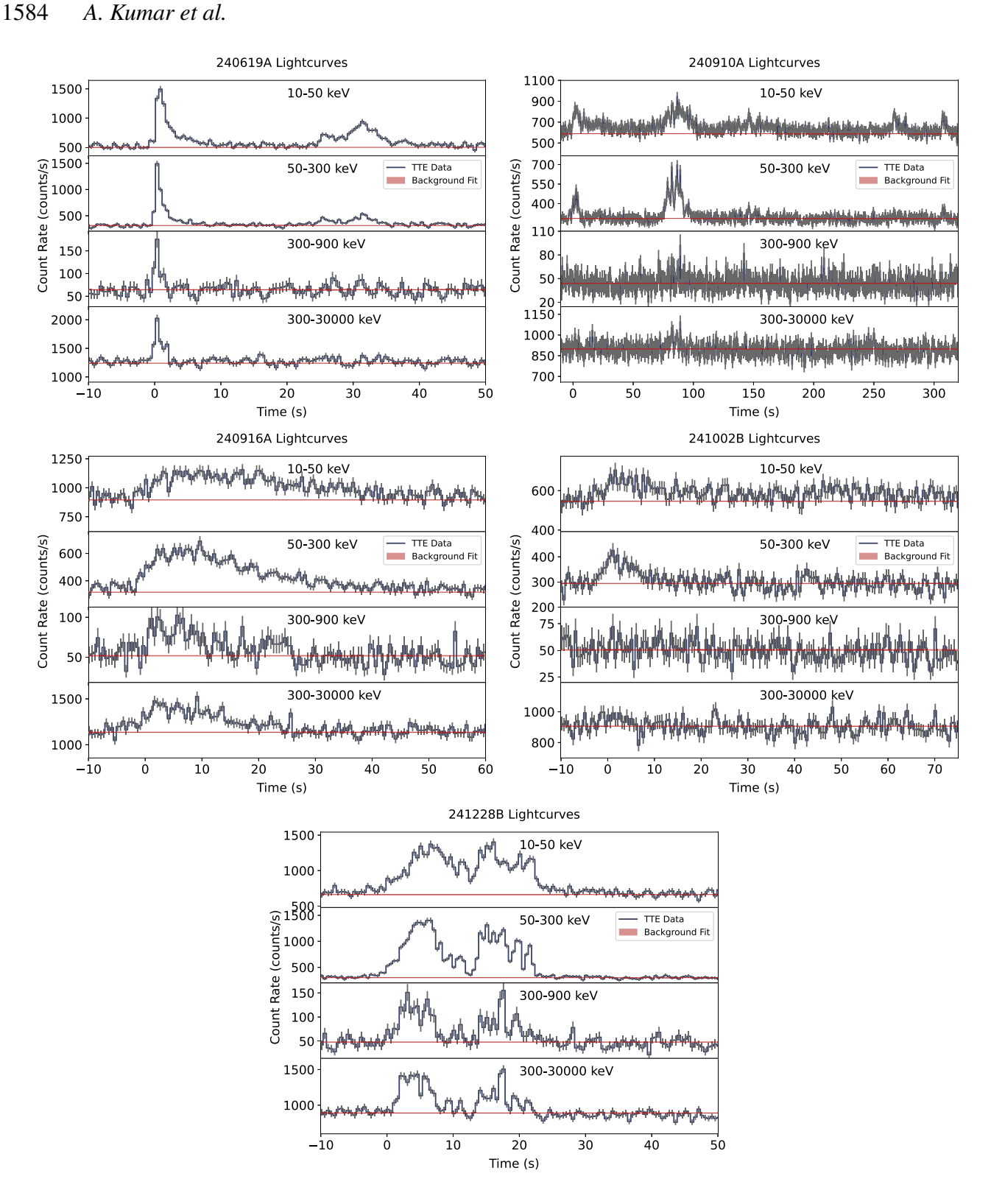


Figure A10. Fermi/GBM light curves for Fermi GRBs in our sample are shown. TTE data are binned to 0.5 s resolution.

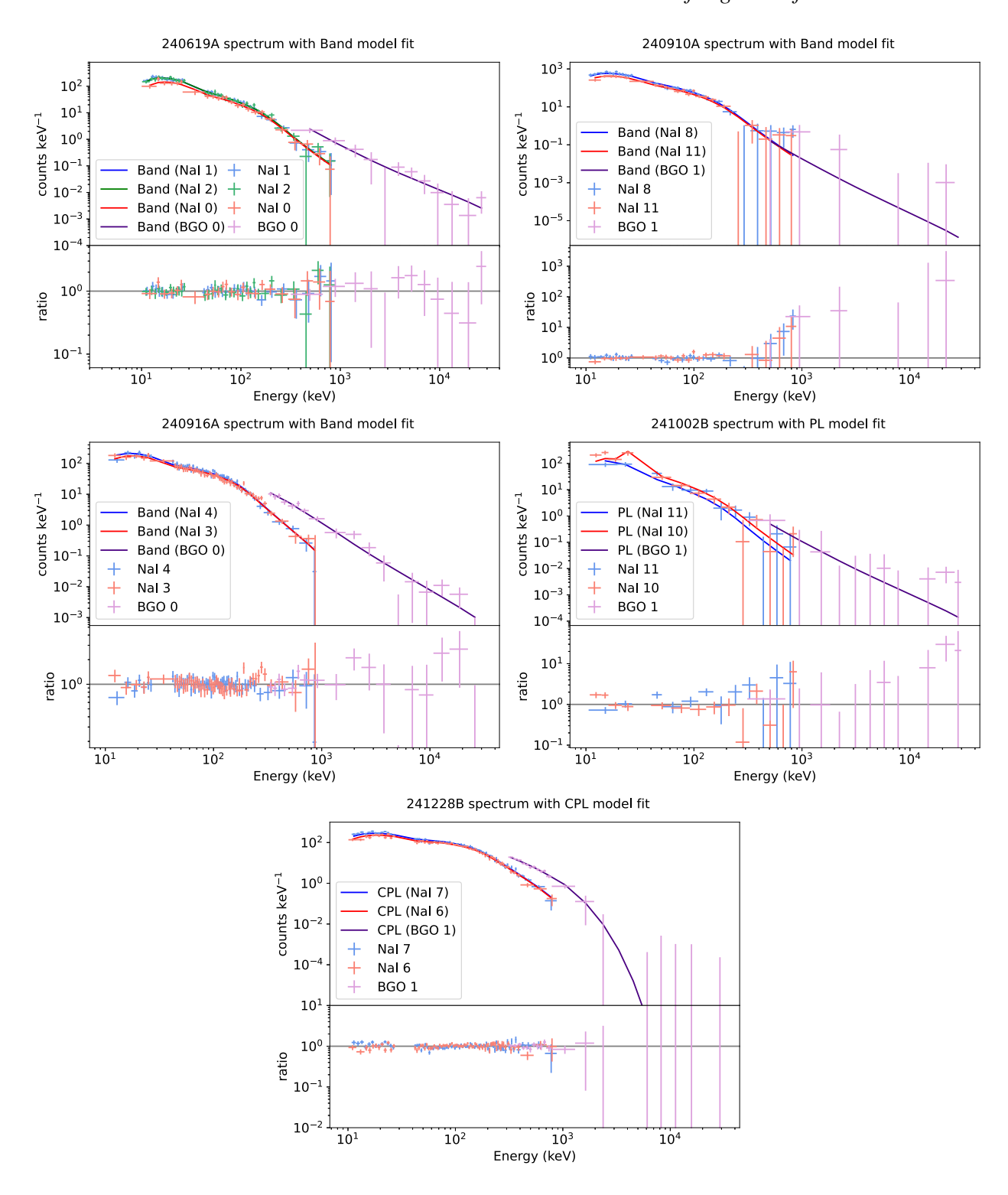


Figure A11. Fermi/GBM fitted spectra for Fermi GRBs in our sample are shown. Models shown are the best-fitting models as described in Table 4. GRB 241228B is poorly constrained in high energies, so the spectrum shown is zoomed in to show the behaviour at lower energies.

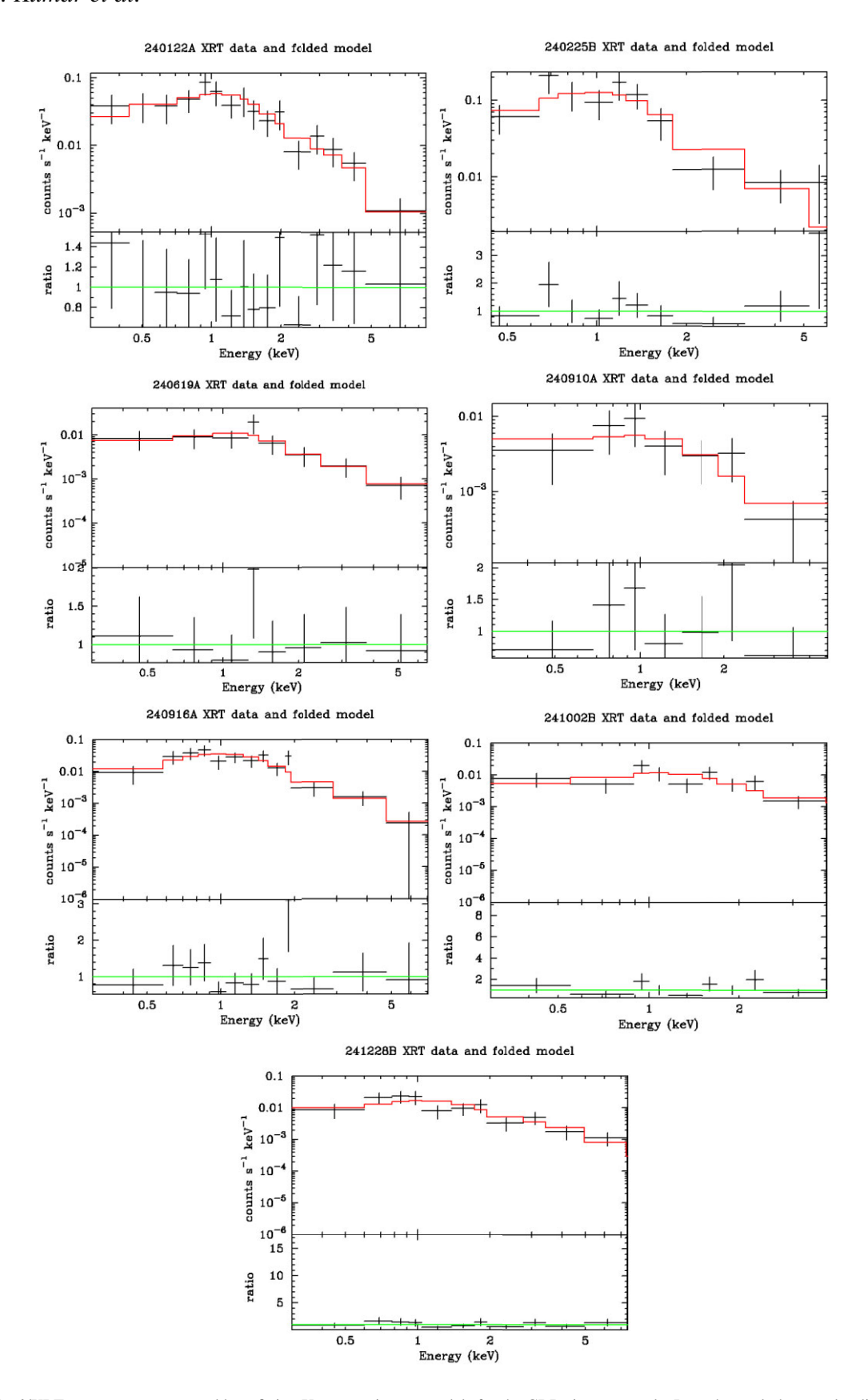


Figure A12. Swift/XRT count-rate spectra and best-fitting X-ray continuum models for the GRBs in our sample. In each panel, the top plot displays observed spectral data with errors (black points) in the 0.3–10 keV range fitted with an absorbed power-law model (red line), using Cash statistics. The bottom plot shows the ratio of observed data to folded model predictions, used to assess the goodness of fit. These spectra were used to derive photon indices and absorption column densities ($N_{\rm H}$), contributing to the multiwavelength characterization of the afterglows.

- ²⁴Institute for Globally Distributed Open Research and Education (IGDORE)
- ²⁵Instituto de Astrofísica de Canarias, E-38205 La Laguna, Tenerife, Spain
- ²⁶National Astronomical Research Institute of Thailand, 260 Moo 4, T. Donkaew, A. Maerim, Chiangmai 50180, Thailand
- ²⁷Department of Physics & Astronomy, University of Turku, Vesilinnantie 5, Turku, FI-20014, Finland
- ²⁸ Jodrell Bank Centre for Astrophysics, Department of Physics and Astronomy, The University of Manchester, Manchester M13 9PL, UK
- ²⁹Institute of Cosmology and Gravitation, University of Portsmouth, Portsmouth PO1 3FX, UK
- ³⁰Departamento de Astrofísica, Universidad de La Laguna, E-38206 La Laguna, Tenerife, Spain
- ³¹School of Physics, University College Cork, Cork, T12 K8AF, Ireland
- ³²Centre for Astrophysics Research, University of Hertfordshire, College Lane, Hatfield AL10 9AB, UK
- ³³School of Physics and Centre for Space Research, University College Dublin, Belfield, Dublin 4, Ireland
- ³⁴National Research University 'Higher School of Economics', Faculty of Physics, Myasnitskaya ul. 20, Moscow 101000, Russia
- 35 Space Research Institute of the Russian Academy of Sciences, Profsoyuznaya ul. 84/32, Moscow 117997, Russia
- ³⁶Centro Astronómico Hispano en Andalucía, Observatorio de Calar Alto, Sierra de los Filabres, Gérgal, E-04550 Almería, Spain
- ³⁷Departament d'Astronomía i Astrofísica, Universitat de València, E-46100 Burjassot, Spain
- ³⁸ Observatori Astronòmic, Universitat de València, E-46980 Paterna, Spain ³⁹ International Centre for Radio Astronomy Research, Curtin University, GPO Box U1987, Perth, WA 6845, Australia
- ⁴⁰Astrophysics Research Institute, Liverpool John Moores University, 146 Brownlow Hill, Liverpool L3 5RF, UK
- ⁴¹ Instituto de Astrofísica de Andalucía (IAA-CSIC), Glorieta de la Astronomía s/n, E-18008 Granada, Spain
- ⁴²Ingeniería de Sistemas y Automática, Universidad de Málaga, Unidad Asociada al CSIC por el IAA, Escuela de Ingenierías Industriales, Arquitecto Francisco Peñalosa, 6, Campanillas, E-29071 Málaga, Spain

- ⁴³Millennium Institute of Astrophysics (MAS), Nuncio Monsenor Sòtero Sanz 100, Providencia, Santiago RM, 8320000, Chile
- ⁴⁴MIFT Department, University of Messina, Via F.S. D'Alcontres 31, I-98166 Messina, Italy
- ⁴⁵Space Science Data Center (SSDC) Agenzia Spaziale Italiana (ASI), Via del Politecnico snc, I-00133 Roma, Italy
- ⁴⁶Department of Astronomy, School of Physics, Huazhong University of Science and Technology, Wuhan 430074, China
- ⁴⁷Clemson University, Department of Physics and Astronomy, Clemson, SC 29634-0978, USA
- ⁴⁸Osservatorio Astronomico di Capodimonte, INAF, Salita Moiariello 16, I-80131 Napoli, Italy
- ⁴⁹Institute of Solar-Terrestrial Physics, Russian Academy of Sciences, Siberian Branch, Irkutsk 664033, Russia
- 50 GRANTECAN S.A., Cuesta de San José s/n, E-38712 Breña Baja, La Palma, Spain
- ⁵¹INAF Osservatorio di Astrofisica e Scienza dello Spazio, via Piero Gobetti 93/3, I-40129 Bologna, Italy
- ⁵²GEPI, Observatoire de Paris, Université PSL, CNRS, 5 Place Jules Janssen, F-92190 Meudon, France
- ⁵³ Institute of Physics and Technology, Institutskiy Pereulok, 9, Dolgoprudny 141701, Russia
- ⁵⁴Astronomical Institute Anton Pannekoek, University of Amsterdam, PO Box 94249, NL-1090 GE Amsterdam, the Netherlands
- ⁵⁵Materials Science and Applied Mathematics, Malmö University, SE-205 06 Malmö, Sweden
- ⁵⁶Nordic Optical Telescope, Rambla José Ana Fernández Pérez 7, E-38711 Breña Baja, Spain
- ⁵⁷E. Kharadze Georgian National Astrophysical Observatory, Mt. Kanobili, Abastumani 0301, Adigeni, Georgia
- ⁵⁸Department of Physics, George Washington University, 725 21st St NW, Washington, DC 20052, USA
- ⁵⁹LUX, Observatoire de Paris, Université PSL, CNRS, Sorbonne Université, F-92190 Meudon, France

This paper has been typeset from a $T_EX/I \Delta T_EX$ file prepared by the author.